Summer 2018

Generation of Large-Volume Diffuse Plasma by an External Ionization Wave From a Single-Electrode Plasma Jet

Seyed Hamid Razavi Barzoki
Old Dominion University

GENERATION OF LARGE-VOLUME DIFFUSE PLASMA BY AN EXTERNAL IONIZATION WAVE FROM A SINGLE-ELECTRODE PLASMA JET

by

Seyed Hamid Razavi Barzoki
B.S. July 2007, University of Kashan, Iran
M.S. September 2011, Shahid Beheshti University, Iran

A Dissertation Submitted to the Faculty of Old Dominion University
In Partial Fulfillment of the Requirements for the Degree of

DOCTOR OF PHILOSOPHY

ELECTRICAL AND COMPUTER ENGINEERING

OLD DOMINION UNIVERSITY
August 2018

Approved by:

Mounir Laroussi (Director)

Sylvain Marsillac (Member)

Rick McKenzie (Member)

Jiang Li (Member)

ABSTRACT

GENERATION OF LARGE-VOLUME DIFFUSE PLASMA BY AN EXTERNAL IONIZATION WAVE FROM A SINGLE-ELECTRODE PLASMA JET

Seyed Hamid Razavi Barzoki
Old Dominion University, 2018
Director: Dr. Mounir Laroussi

A non-thermal transient diffuse plasma can be generated remotely in a nonconductive reduced-pressure chamber by an external guided fast ionization wave (FIW). We found that an atmospheric-pressure low-temperature plasma jet (APPJ) can be a source of FIW which transfers an enhanced electric field at the wave front across a reduced-pressure Pyrex glass chamber with no electrical connection to the chamber. Here, we studied the formation and propagation of the APPJ plasma, the interaction of atmospheric-pressure guided FIW with a dielectric surface which forms the wall of the reduced-pressure system, and the formation and propagation of the reduce-pressure FIW inside a chamber. In this study, key characteristics of the transient diffuse plasma are discussed.

The reduced pressure plasma parameters were measured by Langmuir probe and APPJ electrical measurements were carried out to elucidate the operational mechanisms of the guided FIW as an igniter of the reduced-pressure transient diffuse plasma. It was shown that the transient discharge in the reduced-pressure chamber was generated by an enhanced electric field (18.5 kV/cm when

the APPJ applied voltage was 8.5 kV) inside the chamber that generated a bulk plasma with negative potential due to the nonconductive boundary.

We used fast imaging of both APPJ plasma plume and the transient reduced-pressure FIW inside the Pyrex chamber. Fast images were taken by an intensified CCD to study the launching and propagation phases of both APPJ plasma and the transient reduced-pressure diffuse plasma as well as the incidence of the guided FIW on a dielectric surface. The APPJ plasma plume images revealed that the plasma plume created by guided FIW was in fact made of two discrete volumetric discharges (known as plasma bullet) per applied high-voltage pulse traveling at supersonic velocities up to 170 km/s. Since such a volumetric discharge was initiated by a surface discharge inside the APPJ hollow tube, it had a donut-shape structure.

We also used Optical emission spectroscopy (OES) to determine the physical and chemical characteristics of the APPJ plasma and the transient diffuse plasma. It was shown that the diffuse plasma was capable of producing first and second ionized nitrogen (N^+ and N^{++}), atomic oxygen (O), ionized nitrogen molecule (N_2^+), and $OH^\bullet$ radicals in helium diffuse plasma (with air impurities) and in air diffuse plasma.

The present research shows that this type of electrodeless non-thermal, large-volume diffuse plasma resembles a fast-growing transient glow discharge that lasts for several hundreds of nanoseconds. The electron density in such a plasma with the admixture of helium and air can reach up to 10^{12} cm^{-3} at pressure around 1 Torr. A promising application of the large-volume diffuse plasma is in surface processing such as plasma-aided coating and etching processes with minimal contamination due to the clean environment inside the reduced-pressure system.

TABLE OF CONTENTS

List of Figures

List of Tables

CHAPTER I
INTRODUCTION

In the middle of the 19th century, Jan Evangelista Purkinje, a Czech physiologist, introduced the Greek word “Plasma” for the first time to indicate the clear remaining fluid after removal of all corpuscular [1]. During the 1920s an American scientist, Irving Langmuir, used the same term to describe ionized gases. Generally, plasma is an ionized gas (and sometimes liquid), which is produced by an electric discharge, under certain conditions, that consists of electrons, positively charged ionic species, neutral atoms and molecules, radicals, excited states, and negative ions [2]. Debye screening governed by Maxwell’s equations and the relatively fast electron oscillations are two examples of collective behavior of plasma known as self-consistent electromagnetic forces, which make it different from other forms of gases. Besides the plasma device configuration, each gas composition has a characteristic breakdown voltage, V_B, which determines the minimum rate of the ionization. The ionization degree, η_i -the proportion of total ion number density to neutral gas number density- can vary from a very low value which is known as weakly ionized plasma or non-thermal equilibrium plasma (e.g. 10^{-6}) up to 100% (fully ionized plasma) that is called equilibrium plasma [3]. The wide temperature ranges in plasma technologies as well as electron/ion number density and power density allow plasma devices to be employed in many different applications. Examples are nanofabrication, surface deposition, surface modification, decomposition of solid wastes, purification of wastewater, air purification, biological and biomedical applications such as surface decontamination, food preservation,

wound healing, and cancer treatment [4-8]. Some of the plasma devices that generate such plasmas are categorized in terms of their thermal condition in Table 1.

Table 1. Classification of plasma

High-temperature plasma (equilibrium plasma)	$T_e \approx T_i \approx T_{neutral} \geq 10^5$K $n_e \geq 10^{20}$ m^{-3}	Laser fusion plasma
Thermal plasma Local thermodynamic equilibrium (LTE) (quasi-equilibrium plasma)	$T_e \approx T_i \approx T_{neutral} \leq 2\times 10^4$K $n_e \geq 10^{14}$ cm^{-3}	Arc plasma, Plasma torches, RF inductively coupled discharge
Non-thermal plasma Low-temperature plasma Non-LTE (non-equilibrium plasma)	$T_e \gg T_i \approx T_{neutral}$ $10^{10} \leq n_e \leq 0^{13}$ cm^{-3}	Glow discharge, Corona, APPJ, DBD, MHCD, Plasma needle, Plasma pencil, etc.

I.1 PLASMA SOURCES AND APPLICATIONS

Plasma sources are responsible for providing a condition under which gas breakdown occurs. Depending on the electron energy, electron number density, and current density, different types of plasma regimes are generated under specific conditions. Based on operating parameters such as pressure, the waveform and the amplitude of the applied electric field, the gas mixture, and the neutral gas temperature, different regimes can be generated as they are figuratively illustrated in Figure 1.

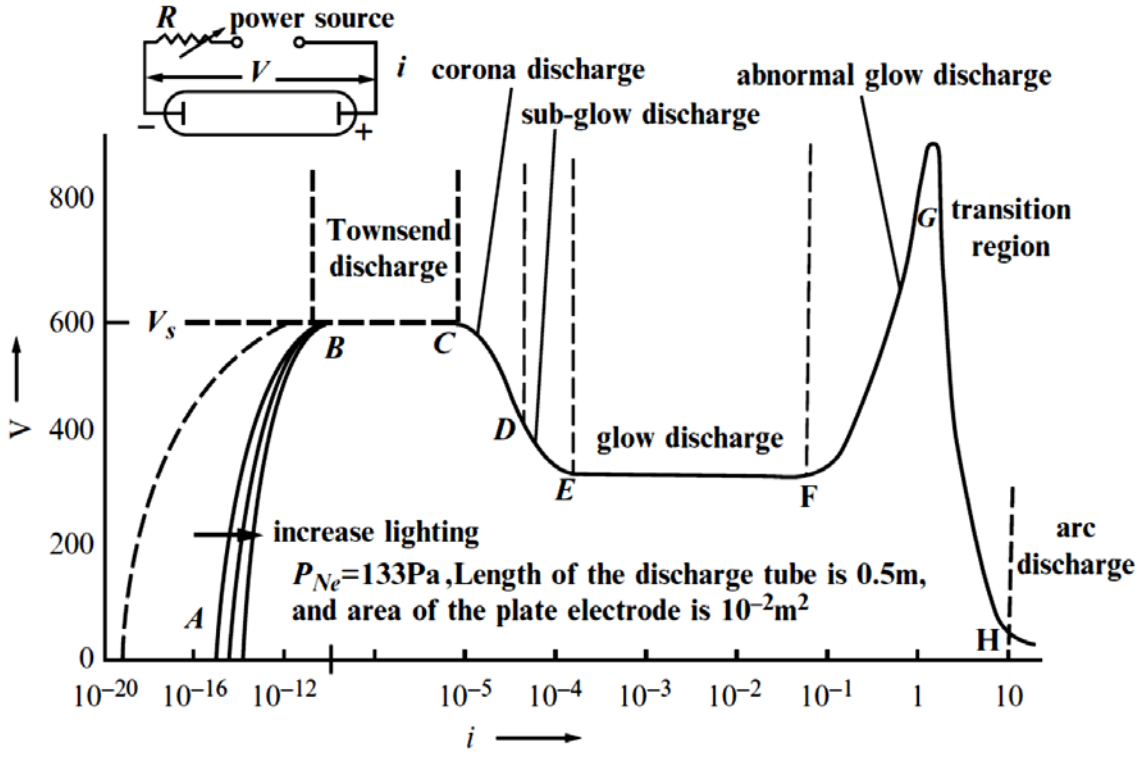

Figure 1. Voltage vs. current relationship for a low-pressure gas discharge. [9]

The current-voltage relationship of gas discharge shows the macroscopic electrical characteristics of plasma behavior inside a regular gas discharge tube with possible discharge regimes ranging from Townsend regime to arc discharge. In a gas tube as voltage increases, different physical phenomena are created depending on the charged species profiles, gas number density, and the type of interactions among electrons, neutrals, and ions in general. Some examples of plasma tubes and their discharge regimes are categorized in Table 2, from Townsend discharge to arc discharge.

Table 2. Examples of plasma-generating tubes working in different operating regions.

Townsend discharge	Ion gauges, Gas filled photocells, Geiger-Müller tubes
Glow discharge	Radar switches (TR duplex switches), Voltage regulators, Flicker glow lamps
Abnormal glow discharge	Glow lamps, Glow switches, Nixie tubes (cold cathode display)
Arc-like transition region	Sign tubes, Fluorescent tubes
Arc discharge	Flash tubes, Quench tubes, Spark gaps, High-intensity discharge lamps (HID lamps), Strobotron lamps

I.1.1 Low-pressure (Low-Density) plasma sources

A plasma generated under the condition of low gas number density, $N<10^{14}$ cm^{-3}, is called low-pressure plasma. The advent of low-pressure systems can be recognized as the origin of non-thermal plasma technologies that have industrially been used. In order to start a Townsend discharge, the plasma with the minimum current density as illustrated in Figure 1, in a low-pressure gas, a minimum breakdown voltage, V_B, is required depending on the gas type, the distance between the electrodes, and the pressure. Below V_B, the only current would be due to the background ionization by external sources of ionizing radiation such as cosmic rays. For a specific gas type, V_B is a function of the product of pressure and the gap distance, *pd*, known as Paschen's law.

$$V_B = \frac{Bpd}{\ln(Apd) - \ln\left[\ln\left(1 + \frac{1}{\gamma_{se}}\right)\right]} \quad (1)$$

Where A and B are two constants for a specific gas and γ_{se} is the secondary electron emission coefficient. There is an optimum value for V_B under a certain pd at which the lowest possible voltage could generate a discharge in the gas.

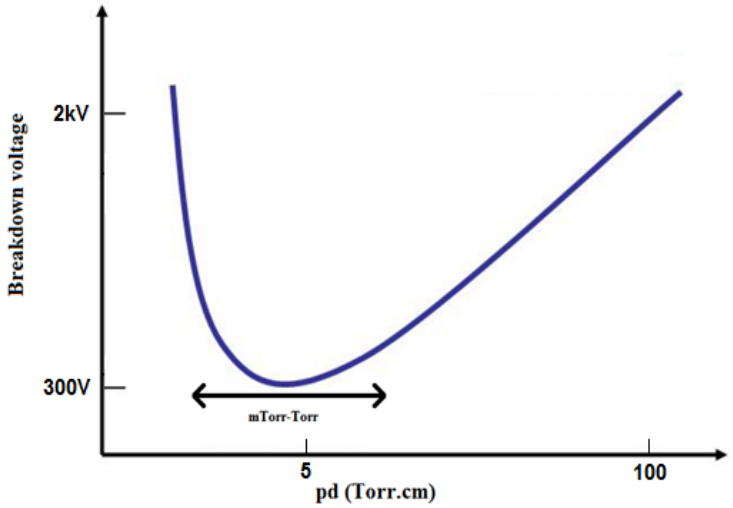

Figure 2. A generic relation between pressure, electrode gap distance, and breakdown voltage according to Paschen's law for helium.

In low-pressure plasmas, the collision rate between particles is negligible. At a sufficiently reduced pressure, the gas temperature cannot reach the electron temperature as Figure 3 shows electron and gas (ion or neutral) temperature as a function of the pressure in a mercury discharge. In fact, inelastic collisions between electrons and gas particles, which result in excitation and ionization processes, are dominant in a glow discharge regime.

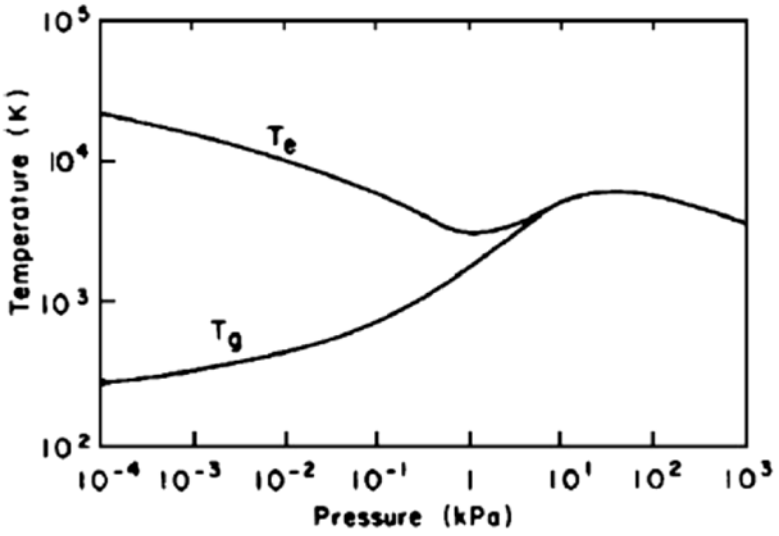

Figure 3. The influence of the pressure on a glow discharge to arc transition and the evolution of electron and gas temperature with the pressure in a mercury plasma [10].

In most operating low-pressure plasma sources, as listed in Table 3, electron number density varies between $n_e \approx 10^{10} - 10^{13} cm^{-3}$ and electron temperature is in the range of $T_e \approx 0.1 - 10\ eV$. It is worth mentioning that there had been many limitations in the possible applications of DC glow discharge because of problems such as arcing on the surface of the workbench or the workpiece, increasing temperature of the system, uncontrollable processes, non-uniformity of the temperature distribution, and overheating the surface of the workpiece. Pulsed-DC glow discharge was developed to overcome the conventional DC-driven plasma problems. [11, 12].

The inductively coupled RF plasmas (ICP) and microwave plasmas have been used for a long while. One of the benefits of these plasmas is the separation of the electrodes from the plasma. The plasma frequency is higher than 1MHz and can be up to 3GHz. The deposited power is transferred to the plasma by displacement current, not conduction current. Advantages are: Less electrode heating, less electron and ion bombardment of the electrodes, lower losses and wall recombination. Because of lower electrode losses, RF and MW plasmas are more electrically

efficient than DC and AC plasma sources. They also have higher electron kinetic energy than DC and AC plasma sources and it is beneficial in industrial applications where higher concentrations of free radicals are required. Besides the benefits and the advantages, there are operational and reliability problems and the expenses of the additional components for their operation. [12-14]

Table 3. Plasma sources and their parameters [15].

Physics	Pressure (mbar)	n_e (cm^{-3})	T_e (eV)	Bias	Application
Dc glow	10^{-3}–100				
cathode region			100	Yes	Sputtering, deposition, surface elementary
negative glow		10^{12}	0.1	No	Chemistry, radiation
positive column		10^{11}	1–10	No	Radiation
hollow cathode	10^{-2}–800	10^{12}	0.1	No	Radiation, chemistry
magnetron	10^{-3}			Yes	Sputtering
Arc, hot cathode					
external heating low voltage	1	10^{11}	0.1	No	Radiation
internal heating	1000	10^{13}	0.1	No	Radiation welding
Focus	10		keV		Radiation
Rf capacitive					
low pressure	10^{-3}–10^{-1}	10^{11}	1–10	Yes	Processing, sputtering
moderate pressure	10^{-1}–10	10^{11}	1–10	No	Processing, deposition
hollow cathode	1	10^{12}	0.1	No	Processing, radiation
magnetron	10^{-3}			Yes	Sputtering
Rf inductive	10^{-3}–10	10^{12}	1	No	Processing, etching
helicon	10^{-4}–10^{-2}	10^{13}	1	No	Processing
MW					
closed structure	1000	10^{12}	3	No	Chemistry
SLAN	1000	10^{11}	5	No	Processing
open structure					
surfatron	1000	10^{12}	5	No	Processing
planar	100	10^{11}	2	No	Processing
ECR	10^{-3}	10^{12}	5	No	Processing
Electron beam					
BPD	10^{-2}–1	10^{12}	1	No	Processing
Dielectric barrier discharge	1000	10^{14}	5	No	Ozone, processing chemisry

I.1.2 Atmospheric-pressure plasma sources

In 1857, Siemens used the first industrial type of cold atmospheric plasma to produce ozone [10]. Atmospheric pressure plasma sources, depending on their characteristics (LTE or non-LTE),

have been extensively used in waste treatment, surface processing, material machining, and biomedical applications [13]. Generating plasma at atmospheric pressure may result in a dramatic increase in discharge current which is known as arc discharge. There are three common methods to avoid arc discharge occurrence at high pressures [10, 13, 16, 17]:

1. To put a limit on the input power of the power supply to suppress the high discharge current.

2. To use an alternating power supply. This method requires an addition of one or more dielectric substances between two electrodes (known as dielectric Barrier Discharge, DBD). Another method is to use high resistivity layer instead of a dielectric. This is known as the Resistive Barrier Discharge, which can operate with AC or DC.

3. To use a pulsed power supply with short pulse duration to prevent the establishment of a thermal equilibrium state.

Applying these methods result in a variety of atmospheric-pressure plasma sources with different characteristics. A list of DC-driven and AC-driven atmospheric-pressure plasma sources and their electron and ion temperature is shown in Table 4 and more detailed characteristics and applications can be found in [13, 18-20]. In the following chapter, atmospheric-pressure low-temperature plasma jets (AP-LTPJs) will be discussed in detail as a distinct promising tool to transport an intense electric field through the high-pressure gas into a low-pressure gas via a solid dielectric barrier. [21]

Table 4. An overview of non-thermal atmospheric-pressure plasmas characteristic [7].

Input Power	Source	Properties	Operating Conditions
DC 10 kHz	Arc discharge	T_g: 3500 K N_e : 10^{13} ~ 10^{14} cm^{-3} T_{rot}: 700 ~ 2500 K	Gas: air
50 Hz alternating current (AC)	Pin plane corona		First power 35 kV, 50 Hz Second power 4.5kV, 50 ~ 10^{50} Hz Gas: He, N_2, Ar, air
50 Hz ~ 10 kHz AC	Dielectric barrier discharge (DBD)	E_e: 1 ~ 10 eV N_e: 10^{14} ~ 10^{15} cm^{-3}	Vpp: 3 ~ 20 kV Gap distance: 0.2 ~ 5 mm Gas: air, He, N_2 Gas flow: 100 sccm
100 ~ 160 kHz AC	DBD jet	P: 500 W	Gas: air, N_2 Gas flow: 40 ~ 100 slm
20 kHz AC	Flexible tube		Gas: Ar Gas flow: 3 lpm Vrms: 8.5 kV Irms: 0.098 A
25 kHz pulse	DBD jet	T_e: 1 eV N_e: 4.3 × 10^{22} m^{-3}	Gas: Ar Vrms: 15 kV
20 kHz AC	Jet	T_g: 300 K T_e: 1.56 eV N_e: 1.8 × 10^{12}/cm^3	Hole diameter: 500 um Gas: air, N_2, He Gas flow: 5 lpm
50 Hz DC	Microplasma	T_{rot}: 700 ~ 1550 K T_{vib}: 4500 ~ 5000 K	Gas: air
DC	Micro DBD	N_e: 10^{14} ~ 10^{15} cm^{-3} E_e: 1 ~ 10 eV	Gas: He, N_2, Ar, Ne Ipp: 0.1 A

I.2 PREVIOUS RESEARCH IN APPLIED PLASMA TECHNOLOGY LABORATORY (APTL)

In APTL laboratory, one of the research foci is the development of low-temperature plasma sources. Laroussi's group developed a high-frequency pulsed plasma jet, plasma pencil, driven by rectangular unipolar pulses with repetition rates in the range of 1-10 kHz. The device consists of a high-voltage electrode and a ground electrode at the vicinity of an exit nozzle in order to avoid the device from shorting through the target surface. Helium flows through orifices in disk electrodes with flow rates in the range of 1-10 L/min. Plasma pencil operates at atmospheric pressure and at ambient temperature as it mixes with air at the exit. The low temperature plasma plume emitted by the plasma pencil is made of plasma bullets which produce short living and long living reactive chemicals. These species, which include O, O_2^*, $OH^\bullet$, NO, NO^2, O_3, play important roles in biomedical applications [22-24]. It has been shown that the plasma bullets also carry a very high electric field at their tip reported to reach up to 95 $kVcm^{-1}$ locally [25-27].

Laroussi and Akman developed a type of non-thermal low-pressure diffuse plasma jet by introducing a non-thermal plasma-jet into a moderate-pressure large chamber in a way that the plasma-jet tube was directly connected to the chamber's inner space. They generated a plasma-jet with a length of 28 cm and with the maximum velocity of 140 km/s at 75Torr. The chamber was filled with helium. They also reported a transition from the jet mode to a diffuse mode below 25 Torr. The diffuse mode showed an expansion of plasma around the plasma-jet tube indicating that the plasma expands radially rather than axially. The chamber with a volume of 11.1 liters was filled entirely with the diffuse plasma when the pressure reached 3 Torr. This plasma can be

classified in the pulsed-DC glow discharge due to its transient ignition by every plasma packets generated by the connected plasma-jet [28].

I.3 ATMOSPHERIC-PRESSURE FAST IONIZATION WAVE AS A SOURCE OF ENERGY

Among the atmospheric plasma sources, atmospheric-pressure low-temperature plasma jets (AP-LTPJs) have been attracting great interest due to their remarkable impact on the biological and medical applications and also due to the supersonic plasma bullet formation. Lu, Naidis, Laroussi, and Ostrikov in [29] explained that the mechanism of the high-speed propagation of the plasma bullets is similar to that of plasma streamers based on the propagation mechanism of atmospheric fast ionization waves.

Fast ionization waves have theoretically and experimentally been studied since the last three decades. Such waves consist of electrically-charged species that travel through space spontaneously. Photoionization process and electron acceleration at the wave front play major roles in ionization and moving the wave front forward while leaving a conductive channel behind. The speed of such waves is up to several hundreds of km/s [27, 30]. There have been several attempts to generate such a wave in a low-pressure environment by applying repetitive high-voltage pulses. For this purpose, one or two electrodes are placed inside a chamber to generate electrons with sufficient energy to ionize the neutral gas. [31]

Recently, it has been shown that low-temperature plasma jets are able to generate fast ionization waves that can considerably be transmitted along with a gas flow at speeds as high as a few hundreds of km/s [24, 29]. In fact, the propagation of ionization wave through a tubular helium flow is due to the streamer discharge phenomenon that will be discussed in detail in the following chapter. The ionization wave, in turn, can play the role of an enhanced electric field and as a remote source of continuing ionization process. The mechanism of a fast positive streamer is figuratively sketched in Figure 4.

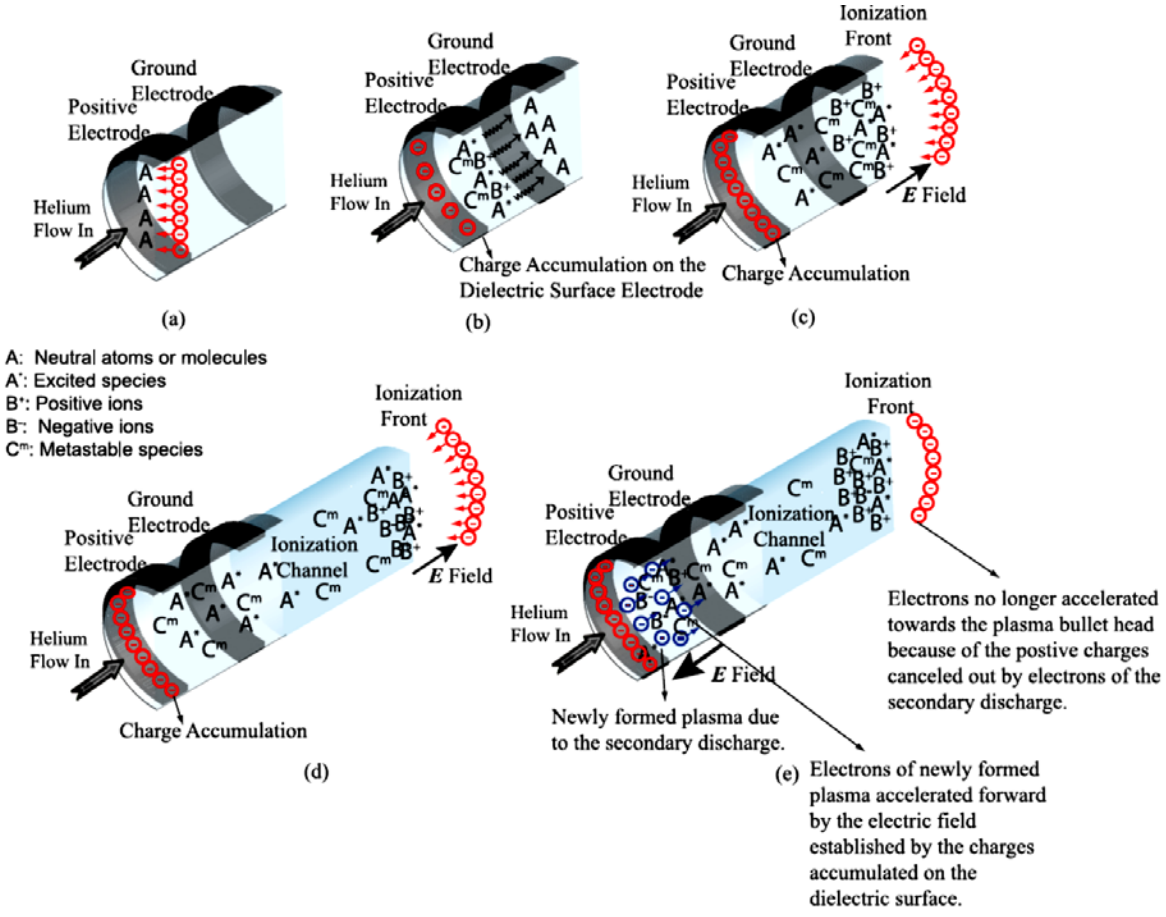

Figure 4. A plasma bullet formation process in a non-thermal plasma jet with a positive and aground electrode [18].

The initiation of a positive streamer begins with electron acceleration and ionization avalanche towards the positive electrode. At the head of a streamer, photons emitted by recombination of positively charged ions leads to photoionization. At this point, a bullet-shaped plasma is formed and photoelectrons are attracted back to the positively-charged species at the head of the plasma bullet. The repetition of this process causes the propagation of the plasma bullet and leaving behind an ionization channel consisting of metastable and excited states, positive ions, negative ions as well as radicals and long-lived chemicals. While the voltage on the electrode decreases, the accumulated electrons on the surface of the dielectric get accelerated towards the ionization channel. Basically, the repulsive Coulomb force of the space charge around the dielectric surface repels the electrons and results in a secondary discharge [18, 32].

Plasma bullet can be used as an innovative source of generating a large diffuse plasma in a low-pressure medium. Here, the enhanced electric field of the plasma bullet plays a role in initiating a gas discharge. Figure 5 shows the electric field at the head of the ionization wave at different distances in a non-thermal plasma jet. As it shows, the average electric field with the maximum of 24 $kVcm^{-1}$, was reported by Laroussi's group [25]. They also reported a maximum local field of 95 $kVcm^{-1}$ at 1.3 cm of the jet axis.

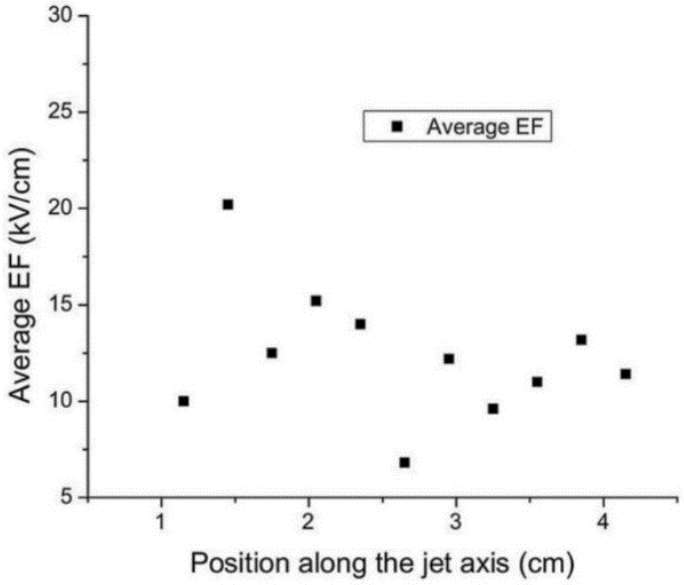

Figure 5. The electric field at the head of the ionization wave. [25]

I.4 THESIS CONTRIBUTIONS TO THE FIELD

The remote generation of a non-thermal diffuse plasma in a nonconductive low-pressure chamber by an externally generated guided fast ionization wave by means of an atmospheric-pressure LTP micro-jet and the study of its physical and chemical characteristics will be the main contribution of the present dissertation. In order to explore the characteristics of the remotely generated diffuse plasma, the external plasma source of energy (LTP plasma micro-jet) will also be investigated. This will include the propagation mechanism of a supersonic-velocity plasma bullet from a single-electrode plasma micro-jet and its interaction with a dielectric surface which forms the wall of the low-pressure system. Time-resolved and space-resolved measurements of the ignition and the propagation phases of the fast ionization waves in the diffuse plasma will be elucidated.

I.5 OUTLINE OF THE THESIS

In chapter II, ionization waves, guided ionization waves, typical examples, and devices are introduced. In addition, the mechanism of formation and the propagation phases of a plasma bullet is discussed in detail. Chapter II gives a scientific idea that implies the capability of atmospheric-pressure guided fast ionization waves as a suitable type of carrying packets of localized energy that is able to be aimed at a specific target remotely and to be transferred through a solid barrier. This considerable idea is the basis of the present research on the generation of a transient-DC diffuse plasma indirectly without introducing any electrodes into a low-pressure system

In Chapter III, experimental setups and methods, different experimental setups including a single-electrode non-thermal plasma jet, a low-pressure system with a nonconductive Pyrex chamber, and instrumentation such as high-voltage pulse generating pulse system, high-voltage and current probes, optical emission spectrometer, and ICCD camera for fast imaging are illustrated and explained.

In chapter IV, titled electrical & electronic characteristics, all electrical and electronic methods that were applied to characterize the AP-LTPJ and the transient diffuse plasma such as I-V measurements, surface charge measurements, total charge measurement in the plasma jet gas channel, and Langmuir probing will be discussed. In the remaining of the chapter, the results of the applied methods will be discussed. This section will focus on the results that are acquired by means of diagnostic instruments such as Langmuir probe, current probe, voltage probe, etc. The results will also give us a broad view about the electrical properties of the ionization wave as a

plasma-generating source, the initial condition of diffuse plasma generation as well as the plasma properties in the low-pressure medium in which the secondary plasma is generated and propagated.

Chapter V covers spectroscopic investigations. The results are obtained by applying fast imaging techniques and spectroscopic methods in order to either evaluate the electronic measurements or measure several complementary information about the characteristics of the single-electrode plasma jet and the secondary diffuse plasma.

Finally, in chapter VI, conclusions, a brief summary of the key features, main findings of the present research, possible future applications, and some recommendations for future research will be presented.

CHAPTER II

FAST IONIZATION WAVES AND GUIDED FAST IONIZATION WAVES

II.1 FAST IONIZATION WAVES (FIW)

In 1835, Wheatstone observed a luminosity travelling very fast along a 6 feet long discharge tube. He could not measure the exact velocity of the propagating luminosity at that time. However, he reported that the velocity could not have been less than $8 \times 10^7 \mathrm{cm/sec}$. In 1893, J.J. Thomson was the first scientist who observed that the luminosity is not a simultaneous start throughout the tube and it travels from anode to cathode at a finite and measurable velocity. He also experimentally concluded that the velocity of the luminosity is independent of the size, shape, and material of the electrodes. Later on, in 1965, Leonard B. Loeb termed that fast travelling luminosity "ionization waves" [33, 34].

The process of the breakdown formation is a function of the relative applied voltage, known as overvoltage, to the breakdown voltage, $\frac{V_{applied}-V_{breakdown}}{V_{breakdown}}$, the gap between the electrodes, h, and the pressure of the system, P, to a considerable extent. For low values of KPh, Townsend mechanism is usually observed. In the case of high values of KPh, the breakdown development exhibits a high-speed space charge propagation in the form of a longitudinal wave. Other important parameters that affect the specific features of the breakdown wave are the gas type, the amplitude and the waveform of the applied voltage, and the geometry of the discharge cell [35].

The ionization rate and the velocity of ionization waves depend on many experimental conditions. The propagation velocity of ionization waves can range from 10^5 to $10^{10} cm.s^{-1}$.

Relatively low propagation velocities of $10^5 - 10^7 cm.s^{-1}$ known as slow ionization waves (SIWs), appear in a homogeneous electric field and while the velocity of the ionization wave is controlled by the electron drift. Subluminal ionization waves with the velocities of $10^7 - 10^{10} cm.s^{-1}$ known as fast ionization waves (FIWs) appear in the final stage of the breakdown when the plasma cloud already exists in the discharge gap. An example of such waves is the return stroke wave of the lightning [30].

Under certain conditions, FIWs can be generated even during the initial stage of the breakdown and without the need of an already existing space charge along the discharge gap. The most important factors are a very short rise time (or a steep slope of the leading edge) of the applied high-voltage pulse to the discharge gap and the presence of pre-ionization in the gap. Generally, the faster the rise time of the high-voltage pulse and the stronger the pre-ionization, the higher the velocity of the FIW.

The breakdown processes that are developed by pulsed discharges at high overvoltages may be streamer or a spatially uniform FIW. Streamer discharge happens usually at relatively low overvoltages and it could be even lower by introducing sufficient free electrons in the discharge space in order to create stronger pre-ionization. FIWs are developed at relatively high overvoltages across the electrodes. The breakdown mechanisms of either discharges are very similar and will be discussed in the next section of this chapter [36].

The effect of gas number density (which is proportional to the pressure) on the velocity, the current, and the attenuation coefficient of the ionization wave is shown in Figure 6 while the other parameters are kept fixed. The curves indicate that the velocity of the FIW is directly proportional to the current and inversely proportional to the attenuation coefficient. This can be explained by the stillness of the ions (relatively stationary) and the high mobility of the runaway electrons in FIWs across the electrodes. It is worth mentioning that this study showed that if the FIW front cannot reach the other electrode, the current of the source electrode may not flow at all through to the grounded electrode, at the other end [30].

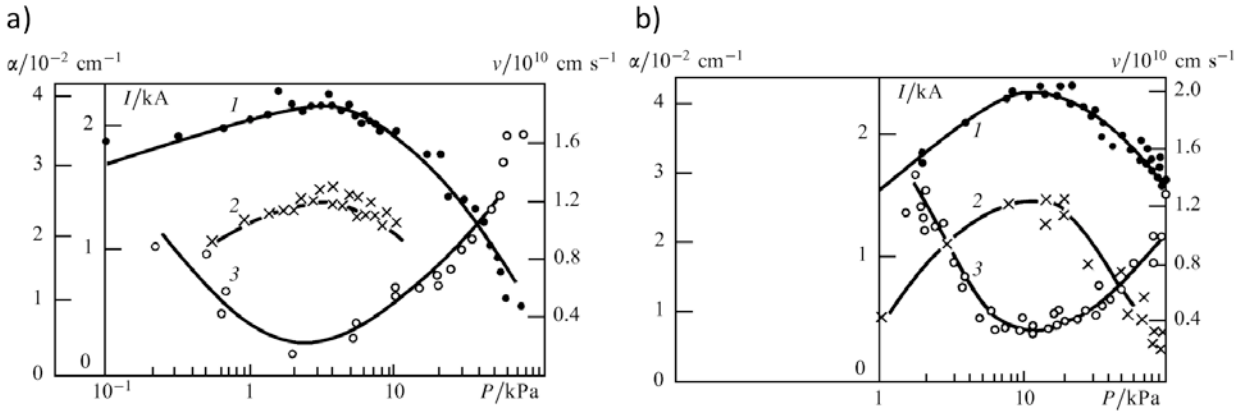

Figure 6. FIW velocity (1), current (2), and attenuation coefficient (3) versus gas pressure in a)air and b) helium with 250kV applied voltage, 47 cm long tube and 0.4 cm in diameter [30].

The promising applications of FIWs are due to their unique features such as supersonic rate of filling the discharge space with highly ionized plasma without heating the gas, strong electric field at the FIW head, and high-energy electrons. One promising application of FIWs may be in the fabrication of physical electronic devices such as fast switches, sharpers, and pulse peaking devices. They also can be used in laser pumping [37] specifically with self-terminating

transitions in excimer mixtures, fast physiochemical combustion waves, and diagnostics of fast flowing gases [30].

II.2 STREAMER MECHANISMS

Understanding the streamers mechanisms is of essential importance for the later discussions in the present research. Streamers as electric breakdown waves are transient non-thermal filamentary plasmas developing and propagating in an insulating media often generated over a nanosecond timescale. Streamers can be found in many types of discharges such as Dielectric Barrier Discharges, DBDs, lightning discharges, and the transient luminous waves in the upper atmosphere. The streamer theory was originally developed by Raether [38] and Loeb and Meek [39] due to some difficulties with explaining the discharge by the classical theories at higher pressures such as the propagation speed. The high reproducibility and greater homogeneity of FIWs differ from the characteristics of streamers. Other than these two differences, streamers and FIWs are very similar in their elementary processes that control the discharge propagation.

There are positive and negative streamers depending on the net positive or negative charge at the streamer's head respectively. In positive streamers (cathode-directed streamers), the breakdown starts from anode and propagates towards cathode and against the direction of the electrons drift while negative streamers (anode-directed streamers) propagate inversely. Thus, in negative streamers, the electrons get accelerated from the discharge channel to the streamer's head region while in positive streamers, the free electrons come from a place in front of the streamer's head

into the discharge channel. Those electrons are believed to be generated by photoionization process.

The behavior of either FIWs or streamers is governed by a classical fluid model including transport equations

$$\frac{\partial n_j}{\partial t} + \nabla.\left(n_j \boldsymbol{V_j}\right) = F_j + S_j \tag{2}$$

$$\boldsymbol{V_j} = \mu_j \boldsymbol{E} + D_j \nabla \ln\left(n_j\right) \tag{3}$$

and the Poisson equation for either positive or negative streamers.

$$\boldsymbol{E} = -\nabla \Phi \tag{4}$$

$$-\nabla(\varepsilon \nabla \Phi) = \sum q_j n_j \tag{5}$$

Where in Eq.(2), continuity equations, and Eq.(3), momentum equations, n_j is the number density of the j-th specie, $\boldsymbol{V_j}$ is fluid velocities of the plasma species, $\boldsymbol{E}$ is the electric field, and $\mu_j$and D_j are the mobility and diffusion coefficients of the j-th specie. In Eq.(4) and Eq.(5), Φ is the electric potential, q_j is the elementary charge for each specie, ε is the permittivity of the studied space, F_j is the production rate of the j-th specie, and S_j is the production rate of electrons-ion pairs due to the photoionization. The continuity equations can be extended by the absorption and emission functions of the existing species which contribute in producing photoelectrons. The fluid model, Eq.(2)-(5), provides the space and time variations of the electron density, ion density, and electric field or electric potential [29].

Applied electric field has been believed to be solely responsible for the streamer dynamics since 1970 [40]. Consider a number of free electrons in a gas (or liquid dielectric) immersed in an external electric field. Those electrons gain energy and collide with neutrals and lose a fraction of their kinetic energy and again this process repeats until they propagate with an average velocity known as the electron drift velocity. If the external field is strong enough so that electrons can gain enough energy between collisions to be capable of ionizing the neutral molecules and create secondary electrons, they will drift together and make an exponential increment of secondary electrons while moving forward known as electron avalanche phenomenon. The avalanche to streamer transition occurs when the local electric field produced by the electrons is comparable to the external electric field. In fact, streamers are driven by the highly nonlinear space charge waves. The streamers dynamics is significantly controlled by the highly-enhanced field at the head of the discharge filament unlike the electron avalanche that is mainly controlled by electron drift and it has negligible effect on the space charge.

The space charge at the head region plays the main role in the FIW propagation since it strongly enhances the electric field up to several times larger than the conventional breakdown field while shielding the external field inside the streamer channel. This high field raises the electron number density and leads to the advancement of the channel into the neutral gas farther ahead. Unlike anode-directed streamers which propagate in the direction of electron drift velocity, cathode-directed streamers propagate against the direction of the electron drift velocity and seed electrons must present in front of the positive streamer head for the spatial advancement. Photoionization, detachment from negative ions, and seed electrons left from previous discharges in case of repetitive discharges are responsible for such a process.

Several models have been developed with and without photoionization taken into account in order to understand its impact on the propagation of the positive streamer. The main correlated factor in the simulations is the initial seed electron density, n_0. In simulation of streamers in nitrogen-oxygen mixtures with very low electron number density, the propagation speed without photoionization taken into account is much lower than the experimental results. However, taking photoionization process into account increases the electron number density around the ionization processes by creating a weakly ionized plasma cloud surrounding the streamer head. This cloud increases the electron density up to $10^8 cm^{-3}$ which significantly increases the speed of the streamer propagation speed [41]. In this study, the oxygen molecules absorption of emitted photons by excited nitrogen molecules is responsible for producing photoelectrons. In another simulation of helium with admixture of 1% air, ionizing radiation of excited excimer molecules He_2^* absorbed by air molecules produce photoelectrons [42].

The main photoemissions of streamers in He/air mixture come from the de-excitation of excimer molecules, He_2^*, the first positive [$1PN_2, N_2\left(B^3\Pi_g\right) \rightarrow N_2(A^3\Sigma_u^+)$], the second positive band systems of N_2 [$2PN_2, N_2(C^3\Pi_u) \rightarrow N_2\left(B^3\Pi_g\right)$], the first negative band system of N_2^+ [$1NN_2^+, N_2^+(B^2\Sigma_u^+) \rightarrow N_2^+\left(X^2\Sigma_g^+\right)$], and Lyman-Birge-Hopfield (LBH) band system of N_2 (LBH N_2,). [$N_2\left(a^1\Pi_g\right) \rightarrow N_2\left(X^1\Sigma_g^+\right)$] [43]. These processes including the possible kinetic mechanisms of guided FIW will be discussed in detail in chapter 5.

II.3 GUIDED FAST IONIZATION WAVES

As mentioned earlier, ionization wave freely propagates in space governed by the continuity and Poisson's equations. Therefore, its path depends on the surrounding conditions. Supplying specific conditions can make a FIW directional and in a predetermined path. An example of guided FIW at low−pressure is restricting its propagation inside a dielectric tube. [33]. In 1970, J.R. Vail et al reported that a laser trail with the ionization left in its path can induce a guided streamer plasma channel as well. They showed that the physical basis of the phenomena is the trail of electrons and ions left by the optical breakdown of the gas through the path of the high-power laser. This can be done either at low-pressure or at atmospheric pressure [30, 44].

Recently, another type of guided FIW has been discovered in APPJs generated in the form of dielectric barrier discharge with a flow of a noble gas such as helium or argon through a dielectric tube that immersed into ambient air. This discovery was independently reported around the same time in two different APPJs, one was RF driven jet and the second was a pulsed DC driven jet (plasma pencil) [24, 45]. In this case, the noble gas channel predetermines the path of the propagation process, as illustrated in Figure 7. As previously mentioned in the section of streamers mechanisms, the excimer molecules emission absorbed by air molecules diffusing into the helium flow channel is responsible for making the channel a preferred path for the propagation of the FIW.

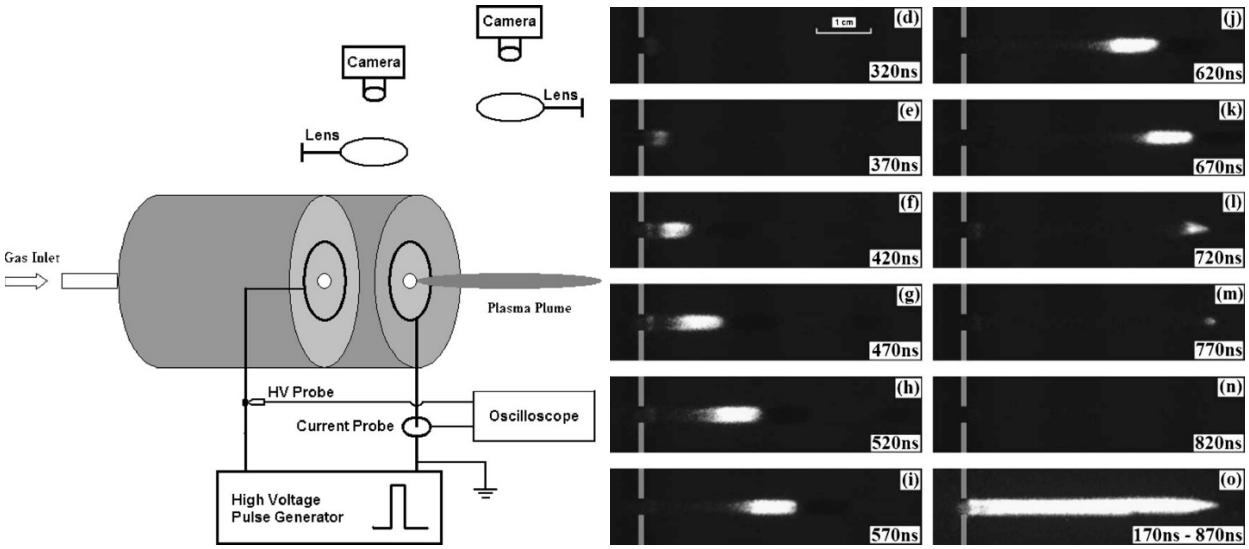

Figure 7. A schematics of an APPJ (plasma pencil) and the high-speed photographs of generated guided FIW through helium flow immersing into air [24].

As mentioned before, positive overvoltage pulses generate plasma bullets (i.e, FIW) while negative overvoltage pulses generate a solid discharge channel along the gas flow. Likewise, as it is clear in Figure 8, the propagation speed of a negative streamer is much slower than positive streamers in guided FIWs.

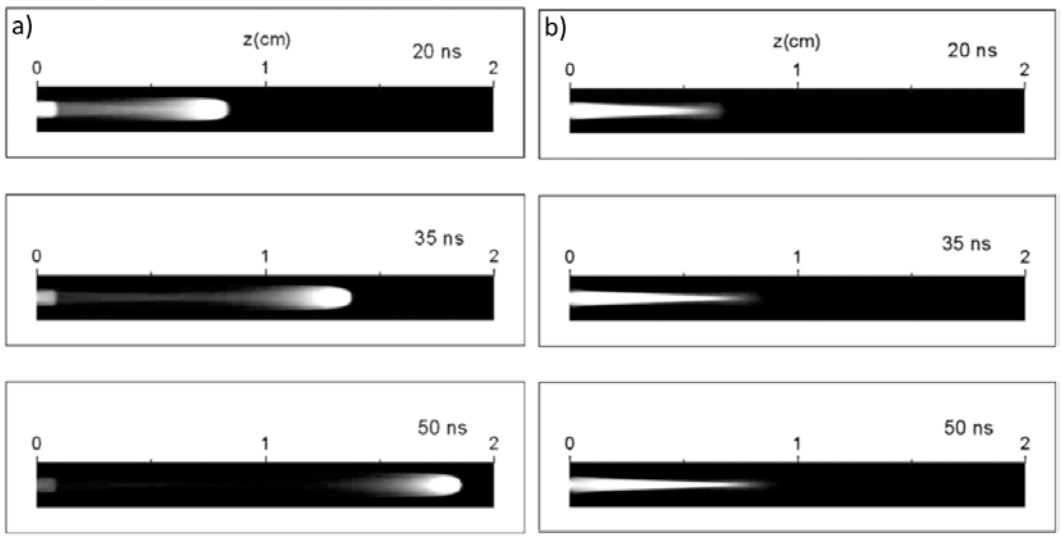

Figure 8. a) A normalized emission intensity of N_2(C-B) for a positive streamer. b) same for negative streamer [29].

Three different sources of large-volume guided FIWs has been chronologically illustrated in Figure 9. In every configuration, there are electrodes in contact with the discharge chamber whether directly placed into the space or not (covered by an insulating material e.g. glass) [28, 31, 33].

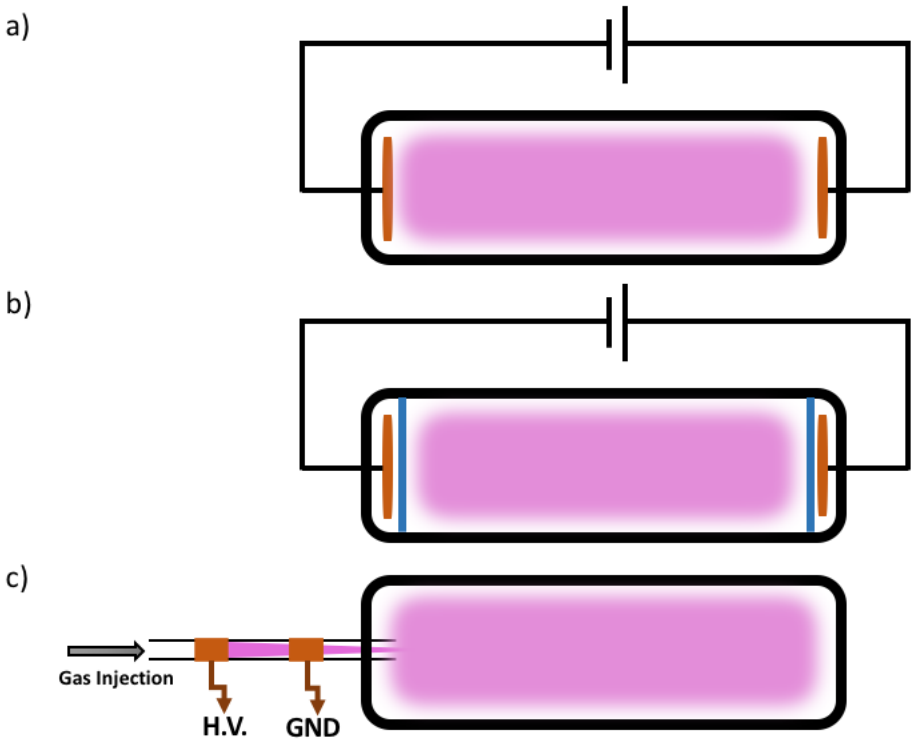

Figure 9. Three different methods of generating FIW at low-pressure system by applying a high overvoltage pulses with a) two electrodes, b) two covered electrodes with thin glass plate, and c) the generation of FIW by means of a plasma jet and introducing the waves into a large-volume chamber [28, 31, 33]. The method shown in c) was developed at ODU's Applied Plasma Technology Laboratory.

The high-speed photographs of guided FIW corresponding to the method in Figure 9c at different pressures is shown in Figure 10 while the container was filled by helium. The breakdown wave at higher pressure, 75 Torr, (Figure 10.a) resembles a plasma bullet generated by the same APPJ source traversing into ambient air. Lowering the pressure causes a transition from plasma bullet to a diffuse transient plasma that propagates in all directions. It was reported that at pressures

below 5 Torr, the diffuse plasma filled the entire space similar to a pulsed-DC glow discharge in an insulating chamber.

Figure 10. High-speed photographs of an FIW generated by introducing a discharge into a large-volume chamber at pressures a) 75 Torr and b) 25 Torr. The chamber is filled with helium. The applied voltage pulse was 7 kV, frequency: 5 kHz, and pulse width: 2 μs [46].

Besides the benefits of the recent method of generating a guided FIW developed by Laroussi's group (Figure 9.c), the limitation of generating such breakdown waves in different gas mixtures such as pure air, Oxygen, and highly quenching gasses was due to the high dependence of the plasma jet on the working gas type. Another limitation of such a configuration is the effect of the pressure on the operation of the plasma jet. Therefore, a novel configuration was proposed (Figure 11) to generate a large-volume diffuse plasma by means of a single-electrode APPJ that is not connected to the chamber and its working gas is independent of the pressure and the gas type inside the low-pressure discharge chamber [21]. In this case, the plasma jet operation can be fully optimized without making any limitations on the discharge chamber configuration.

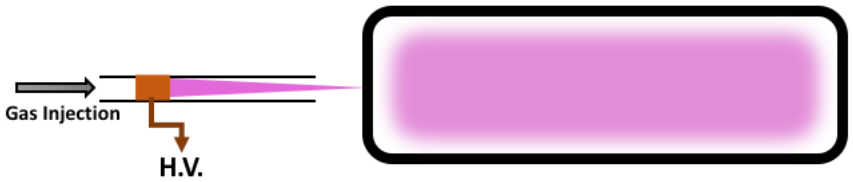

Figure 11. The proposed idea of remote generation of a low-pressure FIW in a large-volume glass chamber by impinging a plasma bullet generated by an APPJ on it [21].

II.4 SUMMARY

In this chapter, a brief history of different types of ionization waves was presented. FIWs and guided FIWs were introduced and their formation and propagation mechanisms (as streamers) was discussed in detail. At the end, the capability of atmospheric-pressure guided FIWs generated by an APPJ as a suitable type of carrying packets of localized energy that is able to be aimed at a specific target remotely and to be transferred through a solid barrier was adopted for the present research work. This considerable idea is the basis of the present study on the generation of a pulsed-DC diffuse plasma indirectly, without introducing any electrodes into a low-pressure system, as a source of a propagating highly-enhanced electric field.

CHAPTER III

EXPERIMENTAL SETUP AND DEVICES

In this chapter, two main sections of the experimental setup will be introduced. This includes an APPJ as the power source driving the generation of a large-volume diffuse plasma inside a dielectric low-pressure chamber system where a transient diffuse plasma is generated. In the following, the plasma experimental setup and diagnostics instrumentation will be introduced. Elements of the experimental setup such as vacuum system, high-voltage power supply, voltage and current probes, optical emission spectrometer (OES), and high-speed camera for fast imaging are explained.

III.1 EXPERIMENTAL SETUP

III.1.1 Single-Electrode Plasma jet

In the present research, two similar configurations of single-electrode plasma jets with different electrode lengths had been used depending on the focus of the research. The picture of a typical atmospheric-pressure plasma plume of a single electrode plasma jet is shown in Figure 12. To generate the plasma plume, a helium flow rate between 1.5 standard L/min (SLM) to 7 SLM was introduced to the plasma jet. The electrode was connected to a high-voltage unipolar square pulse varying from 4 kV to 10 kV, pulse width between 250 ns to 10 µs, and a repetition rate up to 10 kHz. In this configuration, the thickness of the plasma plume was dominated by the tube diameter and the length of the plasma plume could reach up to 70 mm.

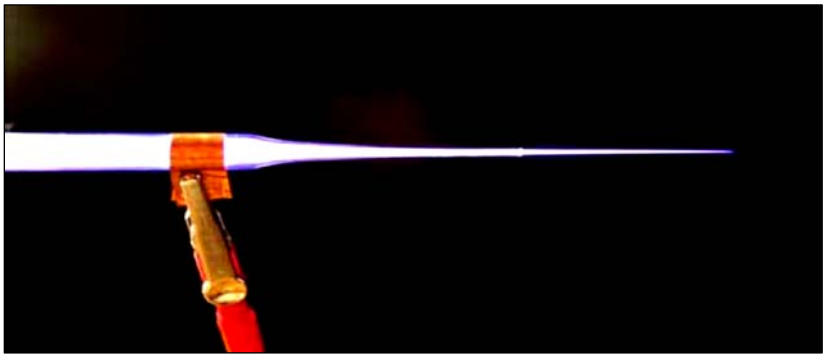

Figure 12. A single-electrode APPJ operating at 7 kV, 7 kHz, 1 µs pulse width, and with 7 SLM helium flow rate.

The plasma jet was made of a copper foil with a thickness of 0.1 mm wrapped around an open end glass tube with a thickness of 1 mm and an inner diameter of 3 mm. The copper foil was connected to the high-voltage power supply. Two different lengths of 10 mm and 10 cm copper foils had been used that will be further mentioned in the experiments presented in the following chapters. No substantial differences in the generation of the plasma plume by varying the length of the copper foil was observed.

As it is shown in Figure 13, the entire experimental setup for the APPJ consists of the plasma jet itself, gas flow meter, high-voltage pulse generating system, digital phosphor oscilloscope, high-voltage probe, current probe, ICCD with focusing lenses, and spectrometer with photomultiplier tube (PMT). The pulse generating system includes a high-voltage DC power supply, a digital waveform generator, and a high-voltage pulse generator.

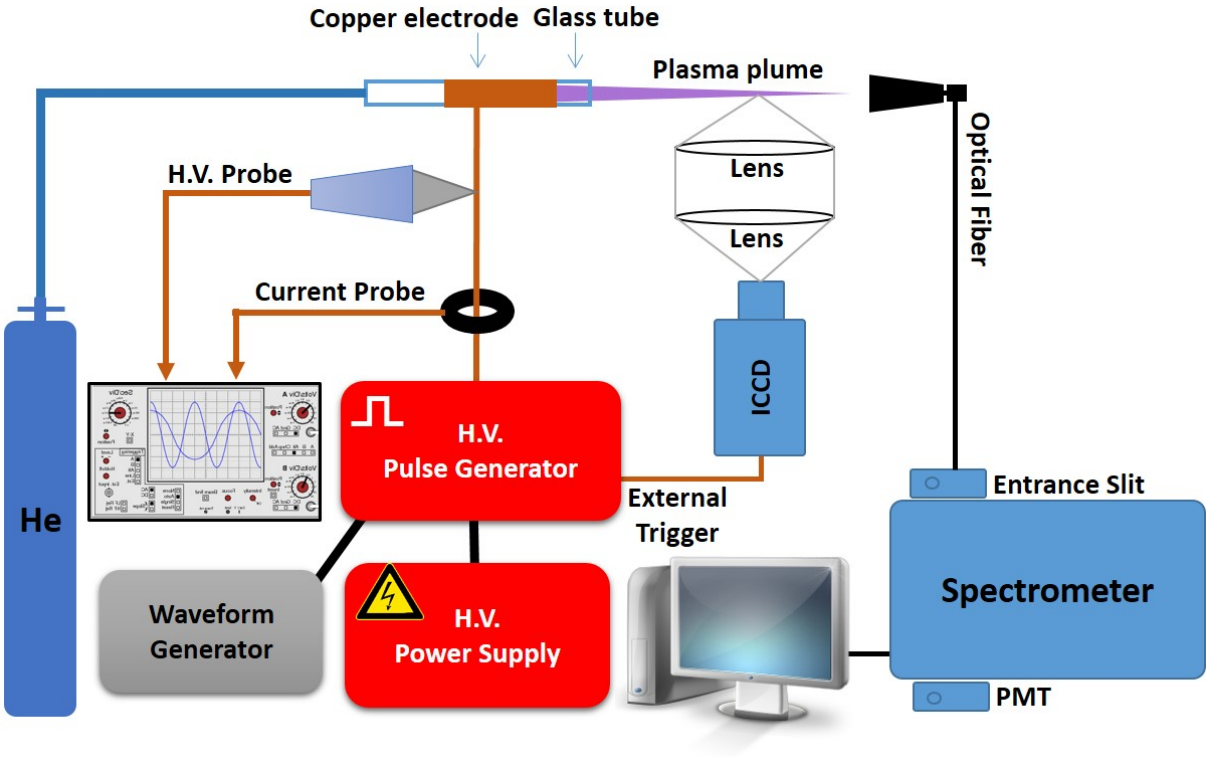

Figure 13. Schematics of a general experimental setup for the APPJ.

III.1.2 Indirect Transient Diffuse Plasma

Generating low-temperature diffuse plasma requires low-pressure conditions in order to increase the mean free path (MFP) of electrons so that they initially gain enough kinetic energy to collide with neutral species and excite or ionize them and eventually have enough time to reach an extended space with less collision. This allows plasma to expand easily in a large volume (depending on the gas type and the gas number density) as well. The more effective ionizing and exciting collisions in a chamber, the larger volume and more efficient plasma will be produced.

The mean free path of an electron depends inversely on the gas pressure and squared distance between the electron and neutral molecule trajectory line. Assuming that two free electrons

collision is unlikely, then the target gas density will mostly affect the electron mean free path as in the streamer mechanism [47].

Figure 14 shows a turbo pump (Adixen ACP15) that was used to evacuate the chamber. Adixen ACP series pumps are optimized for operating without lubricants inside the pumping module. To control the pump operating pressure, Alcatel Adixen ACT200T was connected to the pump. There are also two manual valves to adjust the pressure inside the chamber.

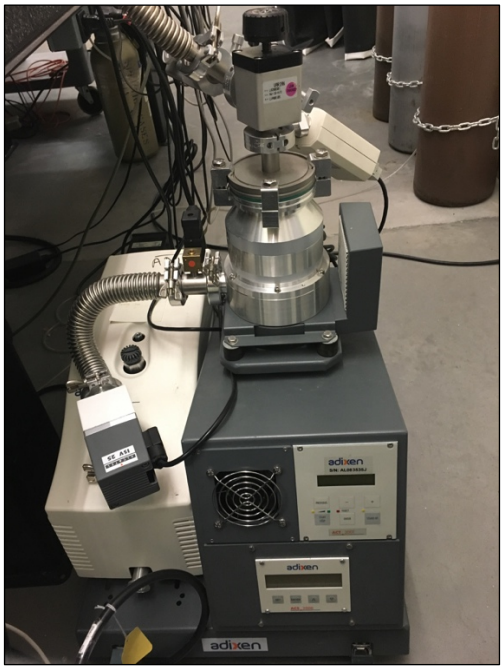

Figure 14. The photograph of the vacuum system Adixen ACP15 with Alcatel Adixen ACT200T control panel.

The schematics of the diffuse plasma setup with different possible orientations of APPJ is shown in Figure 15. A dielectric cross-shaped Pyrex tubing chamber was employed to study the characteristics of the propagating diffuse plasma under reduced-pressure environment.

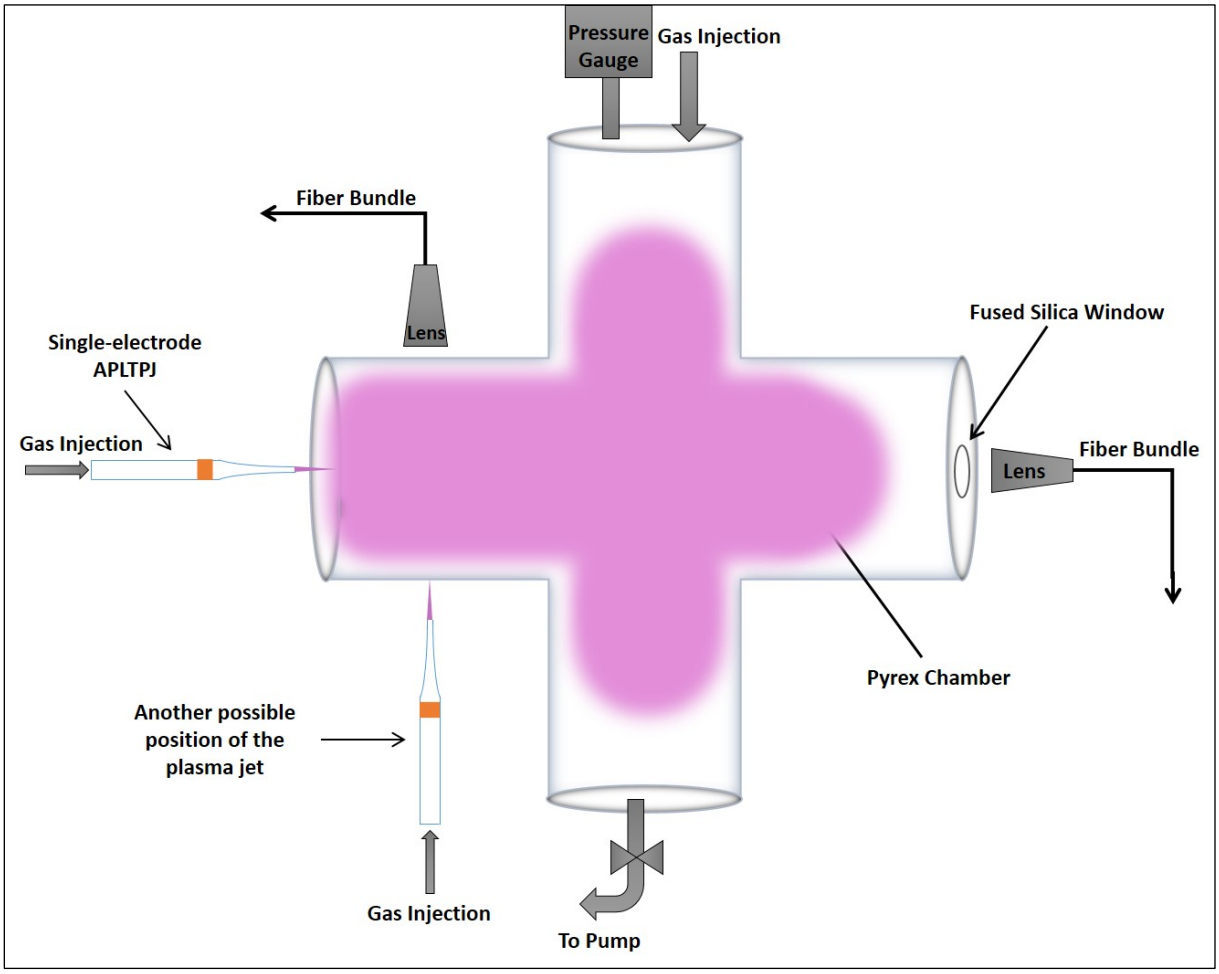

Figure 15. The schematic of the setup with different possible positions of the plasma jet as the source of diffuse plasma.

Two different types of gas injection ports are mounted on the chamber. One is through a standard vacuum clamp/port and the other one is a thin glass tube connected directly to the chamber. Two quartz windows are also mounted on the chamber to measure the emission spectra of the plasma inside the chamber. These windows let photons with a wide range of wavelengths from IR to UV travel through with little attenuation.

To measure the pressure inside the chamber an electrical transducer module (Kurt J. Lesker 902056) through a vacuum gauge was connected to one of the ports.

An optional grounding copper foil with a width of 2 cm was mounted around the chamber to maintain a zero electric potential reference on the glass cylinder when required. In order to make the diffuse plasma spread homogeneously throughout the glass tube, such a grounded ring is necessary.

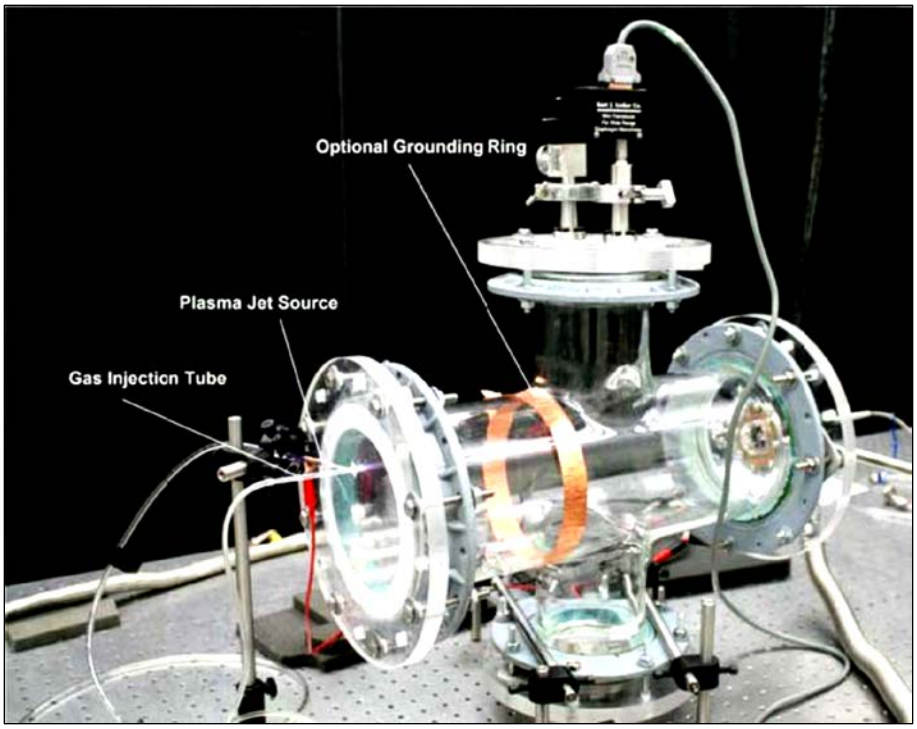

Figure 16. Photograph of the setup with the first possible position of the plasma jet *[21]*.

In order to ignite a diffuse plasma inside the chamber, the plasma jet is brought close enough to the Plexiglass wall of the chamber, so that a bright pink and light purple plasma is generated, as Figure 17 illustrates. The brightness of the diffused plasma depends on the intensity of the ionization wave approaching the outer surface of the chamber wall.

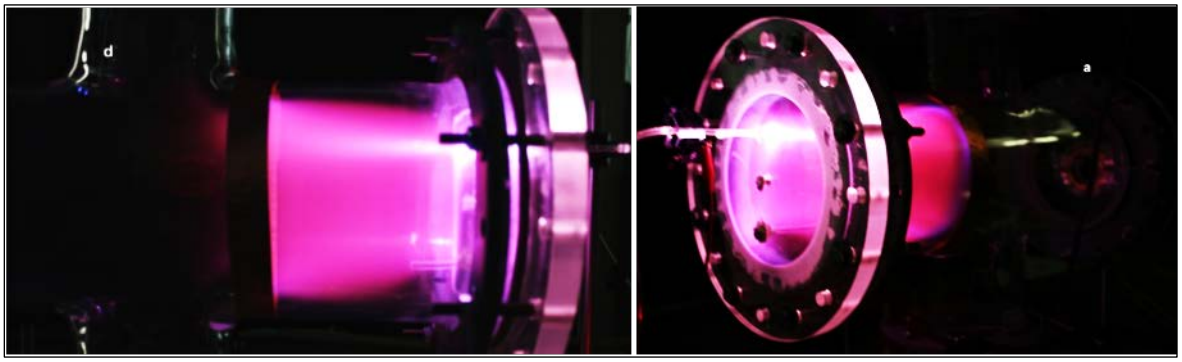

Figure 17. Photograph of the diffuse plasma generated inside the Pyrex chamber *[21]*.

III.2 EXPERIMENTAL INSTRUMENTS AND DEVICES

III.2.1 High Voltage Pulse Generating System

The high-voltage pulse generating system that runs the APPJ consists of a high voltage DC power supply ranging from 0-20 kV (Glassman high voltage, INC, LT series), a high-voltage pulse generator (Directed Energy, Inc. PVX-4110 high voltage ±10kV), and a digital function waveform generator (Agilent 33220A) to provide high-voltage unipolar pulses (Figure 18). As was shown in Figure 13, the high-voltage DC power supply and the waveform generator are connected to the high-voltage pulse generator. The high-voltage pulse generator chops the input high-voltage DC in the shape of the input square signal from the waveform generator. Therefore, the width and the repetition rate of the output pulse is controlled by the shape of the input waveform and the magnitude of the pulse is controlled by the high-voltage DC power supply.

Figure 18. The photograph of the pulsed power supply consists of a high-voltage DC supply (bottom), high-voltage pulse generator (middle), and a 20MHz function/arbitrary waveform generator, Agilent 33220A (top).

Since the input waveform acts as a trigger for the pulse generator, in order to have a clean-shaped (no ringing) output pulse, the rise and fall time of the input waveform should be set as steep as possible.

III.2.2 High Voltage and Current Probes

Measurement of the magnitude of the high-voltage pulses were carried out using a heavy-duty Tektronix P6015A probe. It is a 1000X, 3.0 pF, 100 MΩ voltage probe that measures up to 20 kV

DC and up to 40 kV peak pulse with a duration of up to 100 ms (Figure 19a). Its 75 MHz bandwidth makes it capable of measuring fast signals down to 14 ns pulses.

A Tektronix P6139A probe was also employed in order to measure the net current of the APPJ and the Langmuir probe (Figure 19b). It is a 10X, passive probe, 500 MHz, 8.0 pF, and capable of measuring very fast signals down to 2 ns. This is a suitable probe for the time-resolved measurement of the FIW that will be discussed in the next chapter.

A Pearson current monitor model 4100 was used to measure the current through the high-voltage electrode. Its sensitivity is approximately 1 Volt/Ampere +1/-0% and between 140 Hz and 130 MHz (Figure 19c). This probe is a passive probe that is connected to the oscilloscope with an input resistance of 50 Ω.

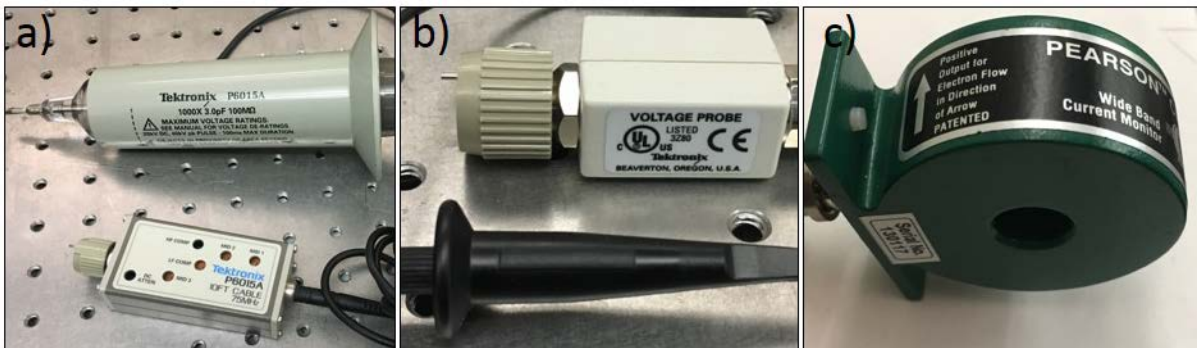

Figure 19. a) High-voltage probe, Tektronix P6015A, b) voltage probe, Tektronix P6139A, and c) Pearson current monitor 4100.

A 500 MHz bandwidth digital phosphor oscilloscope, Tektronix TDS-3054B, was used to read the probe outputs (Figure 20). The oscilloscope was connected to a computer via a local area network (LAN) cable for saving and analyzing the measured waveforms.

Figure 20. Digital phosphor oscilloscope, Tektronix TDS-3054B.

III.2.3 Optical Emission Spectrometer (OES)

An Acton Research SpectraPro 500i imaging spectrometer equipped with an optical fiber bundle that collects the light from a designated point or area by means of a set of transmissive optical devices (UV/visible filters, convex/concave lenses, quartz/glass windows) was used to study the emission spectra of the APPJ and the diffuse plasma inside the low-pressure chamber (Figure 21). The spectrometer aims the light by a mirror to a grating that disperses the spectral light components at varying angles. The dispersed light spectra are then sent to a photomultiplier tube (PMT) to amplify and digitize the spectra. Other than a PMT tube, another way is to use an intensified CCD camera to digitize and visualize the spectrometer output data. With ICCD camera, it is possible to make a time-resolved spectral acquisition with the spectrometer. The same setup is also used to study the time-resolved emission spectra of the diffuse plasma inside the chamber.

Figure 21. Spectrometer SpectraPro-500i with a PMT mounted on it with the capability of mounting ICCD as a complimentary photo-sensing device.

III.2.4 Intensified Charge-Coupled Device (ICCD) Camera

An ICCD camera, Dicam Pro, and a pair of focus lenses (Nikkor 35 mm f/2.8, Nikkor 50 mm f/1.8) was used for high-speed imaging. Its ultra-fast shutter speed allows us to capture images in a few nanoseconds. The sensor inside the camera is a photocathode which is capable of transducing a wide range of wavelengths to photoelectrons as a resultant current with a roughly constant quantum efficiency from 200 nm to 900 nm [48].

The ICCD was used in the imaging of FIWs in both APPJ and the diffuse plasma. It was also used as an alternate sensor for the spectrometer. The advantage of the ICCD over the PMT in spectroscopy is its capability of temporal sensing. It can be used for time-resolved spectroscopy of a very narrow bandwidth of the total spectra while the PMT integrates the measured photocurrents over time. In order to measure a time-varying spectrum, the spectrometer should be set on a specific wavelength so that the ICCD detects the screened spectra coming out of the spectrometer onto its photocathode. In chapter V, the detailed method will be discussed.

Figure 22. Photograph of high-speed ICCD camera, DiCam Pro.

III.3 SUMMARY

In this chapter, experimental setups for the single-electrode non-thermal plasma jet and the low-pressure diffuse plasma system inside a nonconductive Pyrex chamber was introduced and the instrumentation such as high-voltage pulse generating pulse system, high-voltage and current probes, optical emission spectrometer, and ICCD camera for fast imaging were illustrated and explained. Other measurement devices and their configurations, such as Langmuir probe and capacitive probes that were used in the present research will be introduced and explained in detail in the next chapter.

CHAPTER IV

ELECTRICAL & ELECTRONIC CHARACTERISTICS

Characterizing the APPJ as an important part of driving the low-pressure diffuse plasma system is helpful to obtain a complete picture of plasma generation in the low-pressure chamber by transferring ionization-wave packets, which are carried by plasma bullets. This chapter focuses on the electrical and electronic methods that were applied to characterize the APPJ and the transient diffuse plasma. These include I-V measurements, surface charge measurements, total charge measurement in the plasma jet, and Langmuir probing inside the chamber. In the following, the results of the applied methods will be discussed in detail. The results will give us a broad view about the electrical properties of the atmospheric-pressure ionization wave as a plasma-generating source, the initial condition of diffuse plasma generation as well as the plasma properties in the low-pressure medium.

IV.1 METHODS

IV.1.1 I-V measurements

Schematics of the electrical measurement for current-voltage characterization is shown in Figure 23. The voltage of the jet electrode was measured by a high voltage probe (Tektronix P6015A) and the current of the jet was measured using a Pearson current probe that was already explained in chapter 3. Probes were connected to an oscilloscope (Tektronix TDS3054B, 500 MHz bandwidth, 5 GS/s sampling rate).

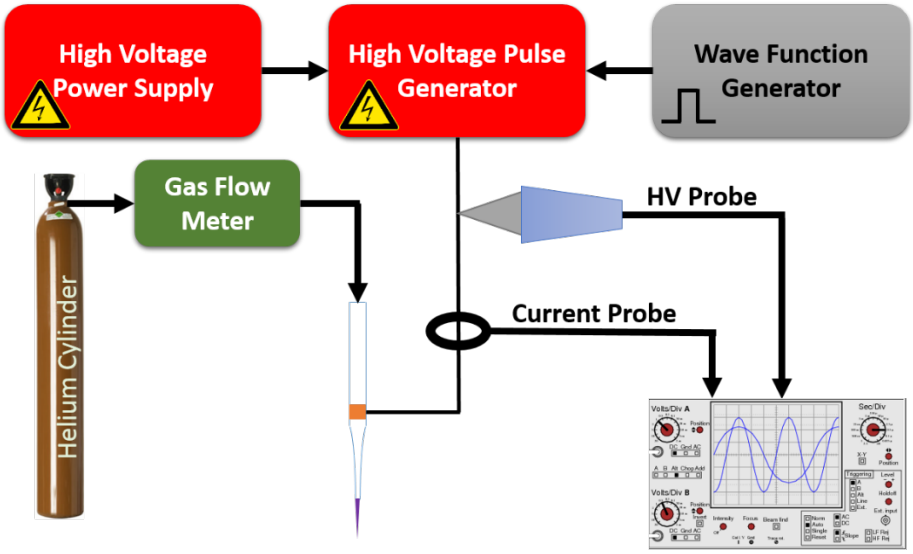

Figure 23. Schematics of the APPJ and the I-V characterization setup.

Measuring the current and the voltage of the APPJ will provide us the consumed power per cycle by integration of the I-V curve. Moreover, we can also calculate the total charge transfer between the plasma device and the power supply by integrating the measured I(t) curve that will be shown and discussed in the results section.

IV.1.2 Spatiotemporal-Resolved Total Charge Measurement Technique (Annular D-dot Probe)

Measurement of the spatial variations of the total charge density in an APPJ plasma plume in addition to the other reported measurements, such as electron density and the density of the ionic (atomic and molecular) species, provides a clearer picture of the mechanisms of the ionization wave propagation. A differential passive sensor can provide a solution to this problem by monitoring the temporal and spatial evolution of the electric field around a propagating plasma plume without perturbing it.

Differential D-Dot sensor is a type of highly-sensitive passive sensor with an output voltage signal proportional to the time derivative of the normal component of the electric displacement vector ($\frac{dD}{dt}$ or $\frac{\varepsilon dE_{\perp}}{dt}$) on the surface of the probe. This type of sensor is usually used for the transient voltage level sensor in transformers and as the electric field sensor based on the electric field coupling principle.

A simple structure of a traditional D-Dot is shown in Figure 24 with a frequency response of equal to a first-order RC circuit [49].

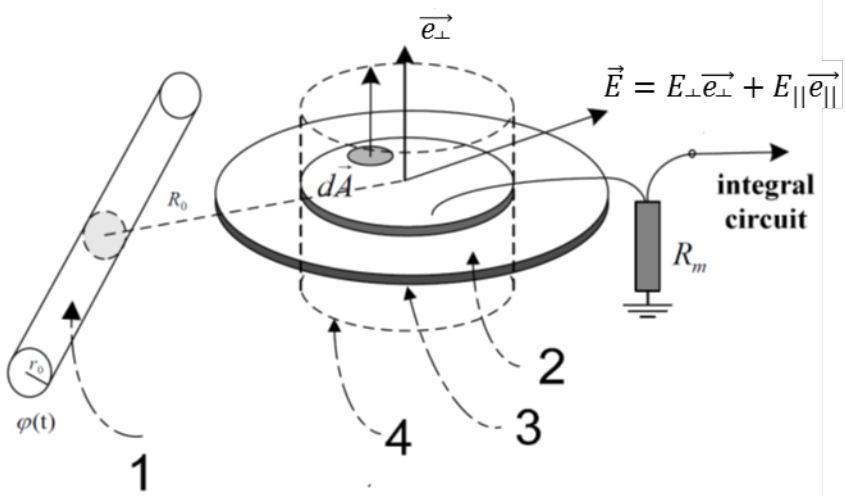

Figure 24. Schematics of the theory of a traditional D-Dot sensor. Part 1 of the figure shows the measured electric potential on a wire with a distance of R_0 from the sensor. Part 2 and 3 show a metal disk with high electrical conductivity and the grounding insulation, respectively. Part 4 shows the closed Gaussian surface covering part 2 of the sensor. The induced charge on the sensor is proportional on the perpendicular component of the electric field to the surface of the sensor, $E_{\perp} = \vec{E}.\overrightarrow{e_{\perp}}$ [49].

Spatiotemporal-resolved measurement of the residual charge in an APPJ channel has been a big challenge due to the failure of the spectroscopic methods to measure the space-charge density. Since plasma bullet characteristics strongly depend on their surrounding configurations, using closely, an active probe to the plasma bullet is very disruptive and makes the measurements

inaccurate. Recently, several attempts have been done by applying integrated electro-optic sensors for electric field measurements. For these measurements, crystals are used and are mainly potassium dihydrogen phosphate (KDP), bismuth germanium oxide (BGO), bismuth silicon oxide (BSO), and lithium niobate ($LiNbO_3$) [50, 51]. The most challenging issue is that the sensor must be as compact as possible in order to have an accurate measurement due to the large electric field gradient. In order to overcome such a problem, we developed an ultrafast passive probe which is a new version of a differential D-Dot sensor that is capable of measuring the transient total charge variation of the plasma bullets that are generated by an APPJ. The output voltage signal is based on the induced displacement current on the probe by the space charge variation over time. Since the plasma bullet travels in a straight line up to a few centimeters, the shape of the sensor was chosen to be a thin ring placed coaxially with the plasma bullet channel as shown in Figure 25. This structure was chosen to maximize the probe surface to amplify the output voltage signal and to minimize the measurement error due to the high sensitivity of the displacement current in an intense electric field gradient at the nearby space.

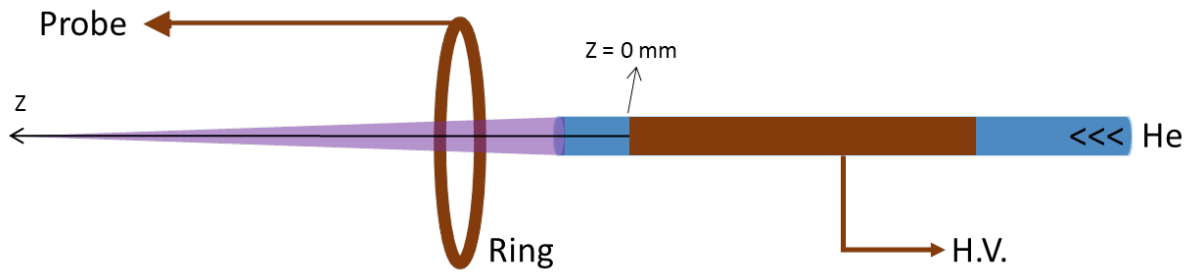

Figure 25. Schematics of the annular D-dot sensor and its relative location to the APPJ plasma plume.

The response time of the probe and that of the oscilloscope are responsible for the lagging, broadening, and attenuating the measured waveforms. These perturbing functions can be

evaluated and removed by means of either rectifiers or computer-based signal processing. Figure 26 shows the experimental setup including an APPJ, a Pearson current probe connected to the electrode, and an annular D-dot sensor at z=0 mm (z = 0 mm correspond to the edge of the copper electrode). The ring is designed to be removable in order to measure and deduce the effect of the displacement current on the entire circuit except the annular D-dot. The length of the electrode is 10 cm. Since we want to study the total charge of one plasma bullet and there are two plasma bullets generated at the same time from two ends of the electrode, the electrode is considered sufficiently long to minimize the impact of the plasma bullet from the other end of the electrode in this case.

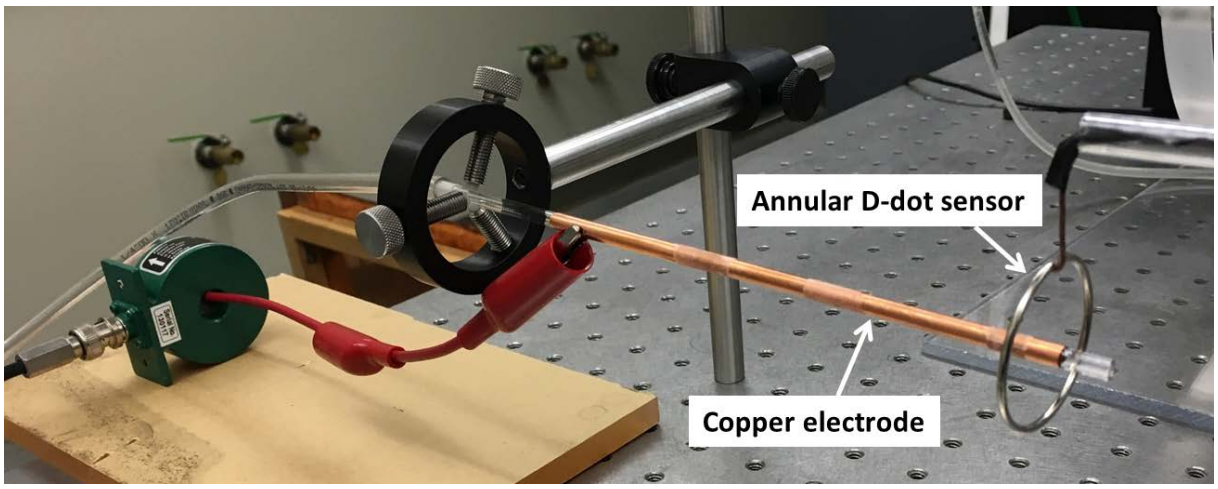

Figure 26. Photograph of the annular D-dot sensor located at the tip of the APPJ electrode (z=0 mm).

Electric field measurement:

The equivalent circuit for the annular D-dot sensor is shown in Figure 27. In this model, the real electric potential on the sensor is a function of the electrical properties of the probe circuit and

the oscilloscope. The voltage drop across the measuring resistor, R_m, is proportional to the electric field variations over time at the measuring point on the sensor. In Figure 27, V(r;t) is the actual voltage on the sensor, $V(r;t)_{probe}$ is the apparent voltage on the oscilloscope, C_{Mutual} is the mutual capacitance between the charge and the sensor, C_{Stray} is the capacitance between the sensor and the ground that is mainly from the wiring, C_{probe} is the probe capacitance, and the measuring resistance, R_m, are considered in the model.

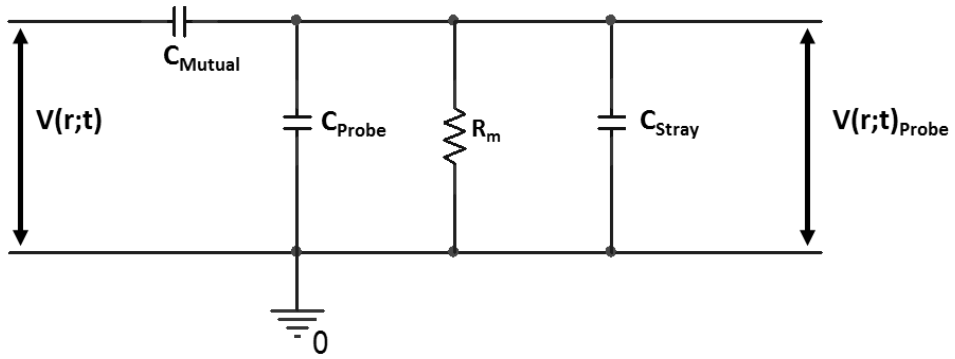

Figure 27. The equivalent circuit model for the annular D-dot probe measurement.

The displacement current is related to the rate of change of the electric field. In the presence of a dielectric, in addition to the free charges, a major contribution comes from charges due to the polarization of the dielectric material. However, since our sensor is a conductor only, free electric charges enter into play. The variation of the induced charge on the surface is proportional to the normal component of the electric displacement field on the sensor.

$$I_D = \iint \boldsymbol{J_D}.d\boldsymbol{S} = \iint \frac{\partial \boldsymbol{D}}{\partial t}.d\boldsymbol{S} = \iint \varepsilon_0 \frac{\partial \boldsymbol{E}}{\partial t}.d\boldsymbol{S} \quad (6)$$

$$I_D = \frac{V_{probe}}{R_m} \approx \varepsilon_0 A_{eff} \frac{\partial E}{\partial t} \quad (7)$$

$$E = \frac{\varepsilon_0 A_{eff}}{R_m} \int V_{probe} dt \quad (8)$$

Where I_D is the displacement current as a result of the charge density variation, $\boldsymbol{J_D}$ is the displacement current density, $\boldsymbol{S}$ is the surface vector of the sensor, and the effective area, A_{eff}, is equivalent to total surface area of the sensor multiply by the perpendicular fraction of the electric field on the surface of the sensor. The annular D-dot radius is 17 mm, the ring thickness is 1.75 mm, the effective area of the ring, $A_{eff} = 3 \times 10^{-4}\, m^2$, and the measuring resistance, $R_m = 50\Omega$. The reason of choosing a ring shape (symmetrical shape) and a large radius was to prevent perturbation of the plasma bullet.

Total electric charge calculation:

When the plasma is said to be off, it is assumed to be connected to a high-voltage source, but an insufficient amount of N_e exists around the plasma jet, so that the plasma device is not capable of forming plasma bullets. At this time, the annular D-dot sensor only picks up and measures the electric field from the electrode, $E_{electrode}$.

Knowing the electric field at the location of the probe, we can model the plasma plume with a set of volumetric arrays of space charge varying with time. Figure 28 illustrates the model including the resultant electric field on the probe.

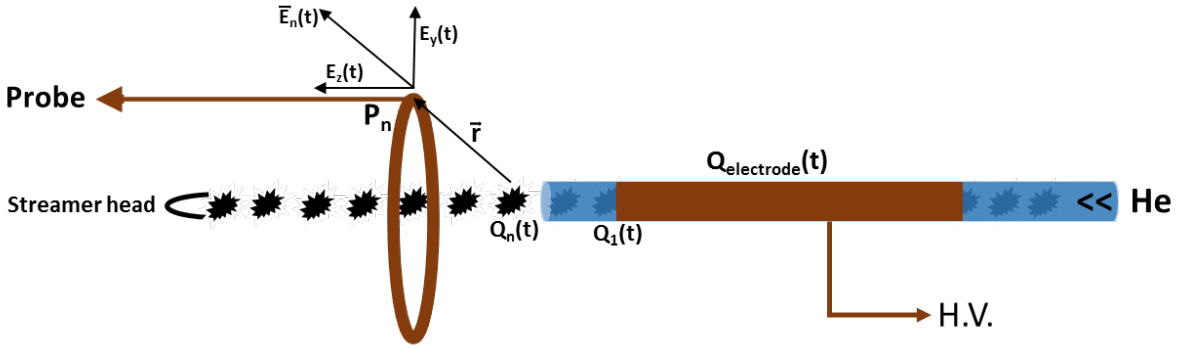

Figure 28. Illustrative model of the net-charge measurement by an annular D-dot sensor. P_n represents the nth location of the probe and Q_n represents the net-charge of the nth volumetric array along the gas channel.

Therefore, the electric field in the vicinity of the probe is

$$\vec{\boldsymbol{r}} = z\vec{\mathbf{k}} + y\vec{\boldsymbol{j}} \tag{9}$$

$$\overrightarrow{\boldsymbol{E}(\boldsymbol{r};t)} = E_z(t)\vec{\mathbf{k}} + E_y(t)\vec{\boldsymbol{j}} \tag{10}$$

Where $\vec{\boldsymbol{r}}$ is the displacement vector between the charge and the probe ring, $z\vec{\mathbf{k}}$ is the axial component of $\vec{\boldsymbol{r}}$, and $y\vec{\boldsymbol{j}}$ is the radial component of the vector $\vec{\boldsymbol{r}}$. The annular D-dot probe measures the magnitude of the electric field at the point where the ring is located. The electric field can be expanded as Eq.(11).

$$\boldsymbol{E}(\boldsymbol{r};t) = \boldsymbol{E}_{\boldsymbol{electrode}}(\boldsymbol{r};t) + \boldsymbol{E}_{\boldsymbol{plasma}}(\boldsymbol{r};t) \tag{11}$$

$$q_{net}(n;t) = q_{negative}(n;t) + q_{positive}(n;t) \tag{12}$$

Where n is the nth array of the plasma plume.

$$E_z(\boldsymbol{r};t) = E_{z,electrode}(\boldsymbol{r};t) + \sum_{n=0}^{N} \frac{q_{net,n}(t) r_{\perp}}{4\pi\epsilon_0 r^3} \tag{13}$$

$$E_r(\boldsymbol{r};t) = E_{r,electrode}(\boldsymbol{r};t) + \sum_{n=0}^{N} \frac{q_{net,n}(t) r_{\parallel}}{4\pi\epsilon_0 r^3} \tag{14}$$

Therefore,

$$|\boldsymbol{E}(\boldsymbol{r};t)| = \sqrt{E_z^2(\boldsymbol{r};t) + E_r^2(\boldsymbol{r};t)} \tag{15}$$

The time derivative of the electric field intensity is directly proportional to the displaced current on the surface of the probe. Solving the coupled Eq.(11-15) over time and the volumetric charge locations result in the spatiotemporal profile of the charge distribution along the plasma plume. This will be discussed in detail in the results section.

IV.1.3 Dielectric Surface Charge Measurements (Capacitive Probe)

This method is applied to measure the cumulative total induced charge on the surface of a dielectric obstacle where an APPJ plasma plume impinges on the other side of it. In this method, a copper sheet is stuck on the dielectric obstacle and the induced surface charge over the sheet is equal to the total polarized charge on the surface of the obstacle due to the plasma device electric field. The schematic of the setup is shown in Figure 29.

The method of the measurement is similar to the displacement current measurement on a capacitor connected in series with a high impedance circuit. The magnitude of the deposited charge is directly proportional to the total capacitance of the circuit shown in Figure 29. The total

capacitance of the equivalent circuit consists of the capacitance of the air gap between the conductive plate and the dielectric obstacle. The thickness of the air gap, d, is in the order of micrometer. Thus, the value of C_{airgap} is a very large value with respect to C_{Wall} and it can be disregarded in the calculation of the total capacitance.

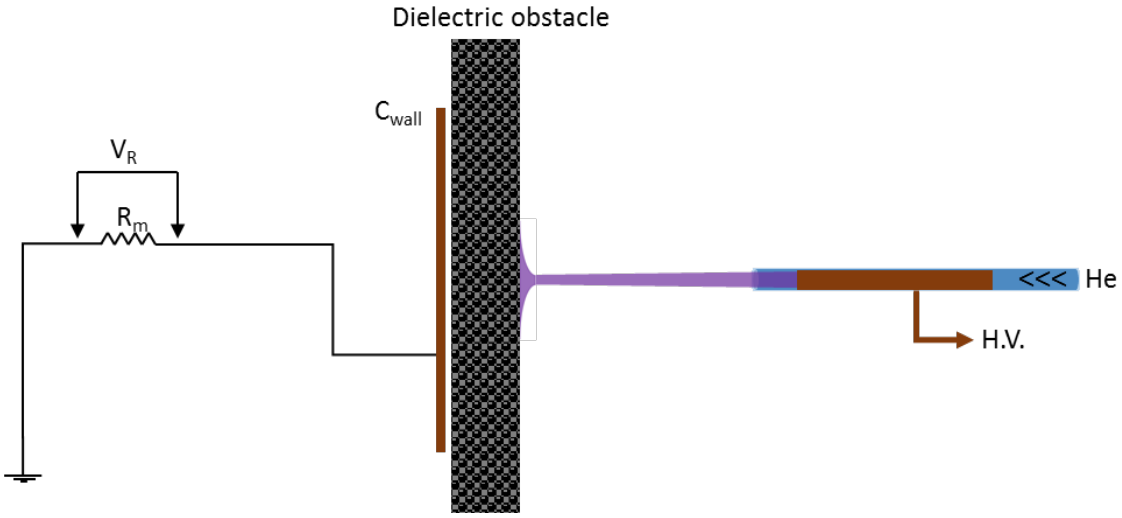

Figure 29. Schematics of the surface charge measurement experimental setup. C_{wall} is the mutual capacitance of the electrical-conductive plate, R_m is a resistor with a known value connected in series with the plate in order to measure the transient current going through the plate.

$$C_{wall} = \frac{\varepsilon_{plexiglass} A}{d} \tag{16}$$

Where C_{Wall} is the total equivalent capacitance of the circuit in series with the resistor, $\varepsilon_{plexiglass}$ is the electric permittivity of the dielectric obstacle located in front of the plasma micro jet, A is the surface area of the copper plate, and d is the thickness of the dielectric material. The electric permittivity of Plexiglass is $\varepsilon_{plexiglass} = 3.2\varepsilon_0$, the value of the resistor

was $R = 1k\Omega$, the surface area of the copper plate was $A = 20cm^2$, and the thickness of the Plexiglass was $d = 17mm$.

$$C_{wall} = \frac{\varepsilon_{plexiglass} A}{d} \tag{17}$$

$$C_{wall} = 3\ pF$$

The total capacitance at the right side of the circuit is equal to the input capacitance of the oscilloscope. Therefore, the lagging time of the measurement will not exceed τ=RC=±3ns. The induced current is

$$I(t) = \frac{dq(t)}{dt} = \frac{V_R(t)}{R} \tag{18}$$

And the total charge is equal to the integration of the current over one period of time (one cycle of applied voltage to the APPJ device)

$$Q_{total} = \int \frac{V_R(t)}{R} dt \tag{19}$$

IV.1.4 Langmuir Probe

Langmuir single probe as an intrusive probing technique is a widely used probe to determine the electron density, electron temperature, Debye length, and the electric potential of reduced

pressure plasma in a quasi-neutrality condition. The probe consists of a very thin and short well-shielded wire, a low inductance resistor, a dual polarity DC power supply, and a differential probe to measure the current (Figure 30).

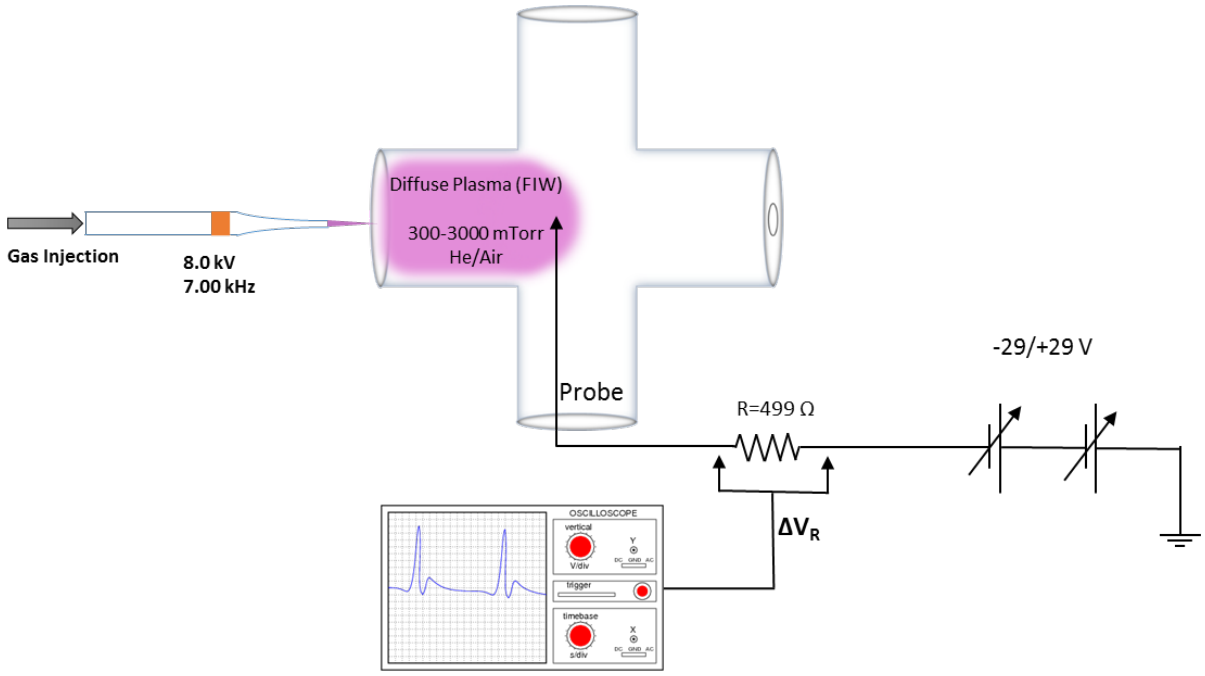

Figure 30. Schematics of current measurement through the Langmuir probe.

When an external body is inserted into a plasma, electrons will be absorbed by the surface of the body faster than ions because of their higher mobility and thermal energy, by at least to a factor of $\sqrt{m_i/m_e}$. A growing negative potential is formed on the body and gives rise to a repulsive Coulomb potential that repels the incoming electrons until the ion and electron flux is equal. Therefore, if a wire is inserted into a plasma, the electrons will leave the plasma and a negative potential that is called floating potential (V_f) will form on the wire and retard the electrons so that the ion influx and electron influx will be equal. In this condition, a net charge of zero is

achieved and charging will stop. If the wire is held at higher or lower voltage than V_f, it will collect more electrons or ions, respectively.

A cylindrical Langmuir probe shielded by a glass tube was fabricated with a copper tip of 0.15 mm thick, 5 mm long, and surface area (A_{probe}) of 2.36 mm^2. A Tektronix P6247, 1GHz differential probe with 200MHz bandwidth was connected to a 499 Ω resistor in series with a dual polarity power supply (BK Precision 1760a triple output DC) and the voltage difference across the resistor was measured by Tektronix TDS3054B oscilloscope (500 MHz bandwidth, 5 GS/s sampling rate). A Tektronix P6139A voltage probe (10×, 500 MHz, 10 MΩ, 8 pF) was also connected to the output of the power supply to monitor the biasing voltage. The voltage was swept from -29 V to +29 V.

In a Langmuir probe I-V curve, four regions can be considered. The first one is the ion saturation region which is the left tail of the curve. In this region, the probe voltage is set to a very negative value in order to repel the surrounding electrons and to collect mostly positive ions. In the second region and step by step voltage increment, the curve gets to a point at which the electrons can only reach the probe by random thermal impacts. The voltage is equal to the plasma potential, V_f, and ion current is equal to electron current and the net charge is zero through the probe. The third region is when the current grows exponentially until a bending point is achieved. At that point, the sheath disappears and the electrons do not sense any retarding potential and it shows the electron saturation current, I_{es}. Beyond this point, the extra potential will attract surrounding electrons and the current increases linearly.

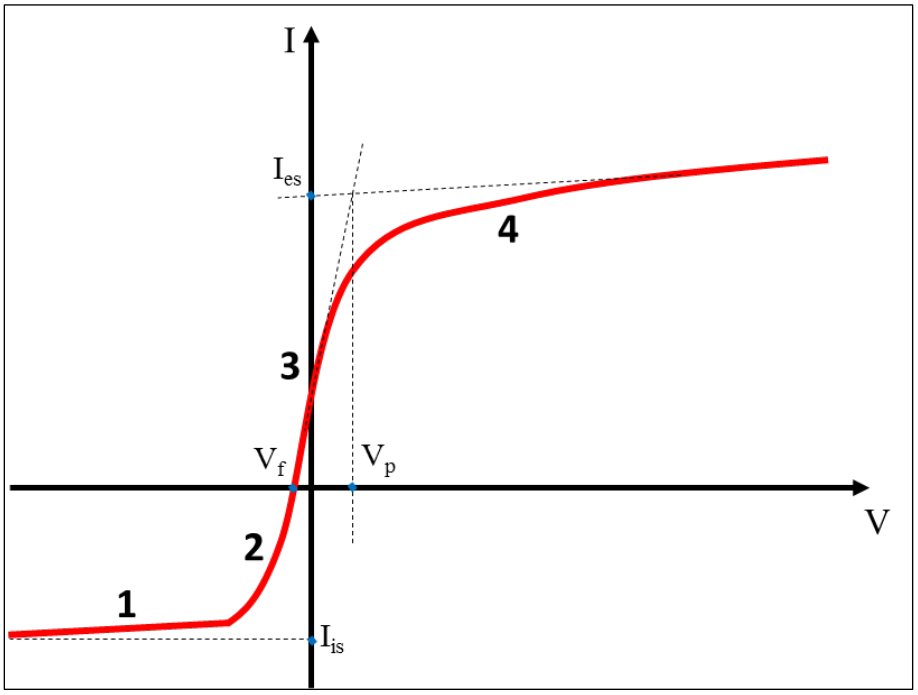

Figure 31. A typical Langmuir probe characteristic I-V curve.

From the floating potential, the electron temperature, T_e, can be calculated assuming Maxwellian distribution.

$$V_f = -\frac{k_B T_e}{2e} \ln\left(\frac{m_i}{2.3 m_e}\right) \tag{20}$$

Where k_B is Boltzmann's constant, m_i is the average ion mass, and m_e is the mass of resting electron. Electron number density can be calculated by

$$I_{es} = n_e e A \left[\frac{k_B T_e}{2\pi m_e}\right]^{\frac{1}{2}} \tag{21}$$

Where k_B is the Boltzmann's constant and I_{es} is the measured current at the plasma potential, V_p.

The plasma frequency can be calculated by:

$$\omega_p = 2\pi f_p = \sqrt{\frac{n_e e^2}{\varepsilon_0 m_e}} \tag{22}$$

Where ω_p (or f_p) is the plasma frequency. Electromagnetic waves with a frequency less than the plasma frequency are reflected by the plasma while those with a frequency higher than the plasma frequency are transmitted.

By knowing the electron temperature and electron density, Debye length, λ_D, of the plasma at the point of the Langmuir probe can be calculated.

$$\lambda_D = \sqrt{\frac{\varepsilon_0 k_B T_e}{e^2 n_e}} \tag{23}$$

IV.2 RESULTS AND DISCUSSION

Using the methods described in the previous sections, we will now focus on the results and the technical approach to address measurement problems. Because the measurements were sensitive to noise, we put the wave function generator and the high-voltage pulse generator in a well-shielded Faraday cage in order to lower the external high electromagnetic noises affecting the measurement procedures. We also put the measuring devices at a great distance from the noise making devices and used low reactance wiring.

In the following measurements, unless specified otherwise, we set the parameters at fixed values of 7 kV applied voltage, 7 L/min helium flow rate, 7 kHz applied frequency, and 1 μs applied pulse width to study the APPJ effects. In most cases, the rise time and the fall time of the applied voltage are at 100 ns and 1100 ns, respectively. All measurements were done in ambient air and ambient temperature and the electrical measurements were done by averaging 512 samples in every measurement procedure, unless it mentioned otherwise.

IV.2.1 Single-Electrode Plasma Jet

I-V measurements

The applied high-voltage waveform to the APPJ is a unipolar square nanosecond pulse as it is shown in Figure 32. The resultant current is a nanosecond transient waveform with a positive current peak at the rise time of the pulse and a negative current peak at the fall time of the pulse that indicates the capacitive behavior of the plasma device.

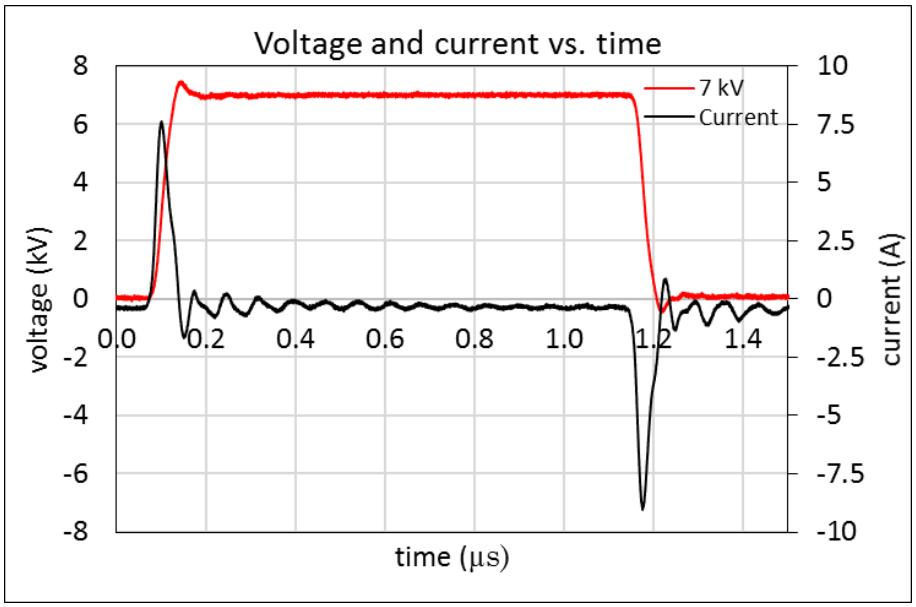

Figure 32. An example of the current and the voltage graph of a running APPJ while plasma is on at 7 kV, flow rate: He 7 slm, frequency: 7 kHz, and pulse width: 1 µs.

The influence of the applied voltage on the total current is shown in Figure 33. The current peak in an APPJ strongly depends on the capacitance of the device and the applied voltage as we have $I.\Delta t = Q = C.V$. The larger the capacitance and the applied voltage, the higher the induced charge and the current peak. The peak values increased linearly by increasing the applied voltage.

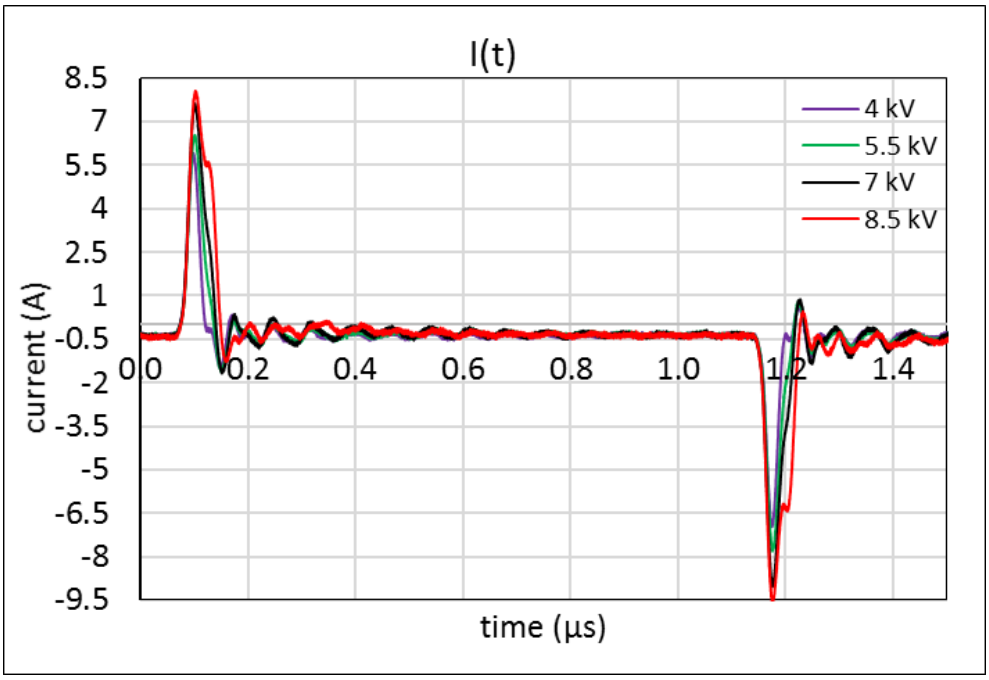

Figure 33. The influence of the applied voltage on the total current in the running APTLPJ with plasma ON at fixed flow rate: He 7 slm, frequency: 7 kHz, and pulse width: 1 µs.

It had been shown that discharge current in an APPJ has similarly a positive and negative current peak during the time of the formation and the propagation of the first and the second plasma bullet, respectively. It had also been observed that the first current peak begins after 50 ns of the voltage rise time and the second current peak happens right after the fall time of the high voltage pulse. The short delay for the first plasma bullet is due to the time of the formation of the internal electric field that makes the plasma streamer able to propagate against the electrode. The second plasma bullet does not need this time period due to already accumulated electrons and charged species in the device tube during the first discharge. In Figure 34, the effect of the applied voltage on the start point of the first and the second discharges are shown clearly [26].

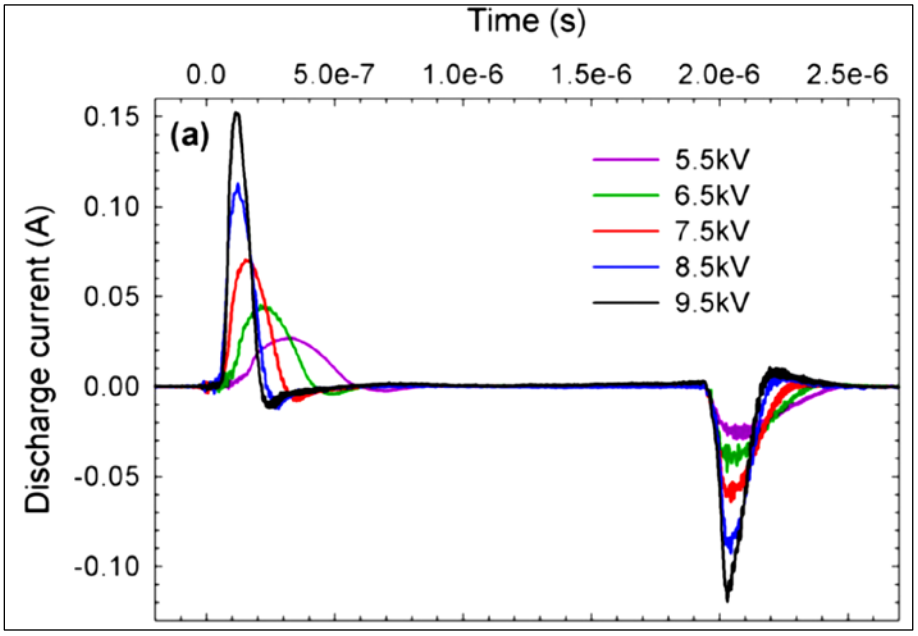

Figure 34. The effect of the applied voltage on the start time of the discharge current of an APPJ device [26].

Figure 35 shows the consumed power of both the APPJ and the plasma plume versus time. The dissipated power is in the range of kilowatts that lasts for a few nanoseconds and the total injected energy is in the range of millijoules. As it is clearly shown in Figure 35, although the current peak has a linear response to the applied voltage, as mentioned before, the power peak on the electrode increased nonlinearly by increasing the applied voltage. Therefore, the applied voltage has a strong influence on the injected energy into the plasma plume per cycle. However, that was not affected by the gas flow rate and the applied frequency with a similar pattern.

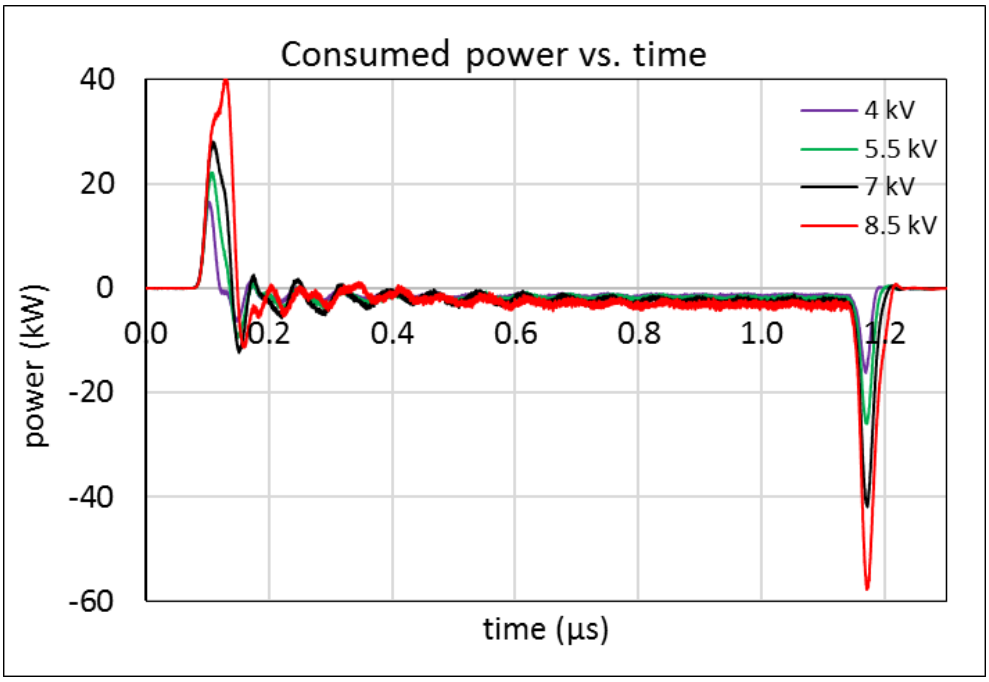

Figure 35. The influence of the applied voltage on the total power dissipation of the APPJ including the device and the plasma plume.

Figure 36 shows the Lissajous pattern of the device with different applied voltages. The area inside the pattern expresses the consumed power per cycle. The pattern shows that the current is non zero when the applied voltage rises from zero to its maximum value and when it falls from the highest value to zero. The current is zero when the applied voltage remains at its plateau value. This indicates that the majority of the power is consumed during the rising and falling of the voltage at the time of the plasma bullets generation.

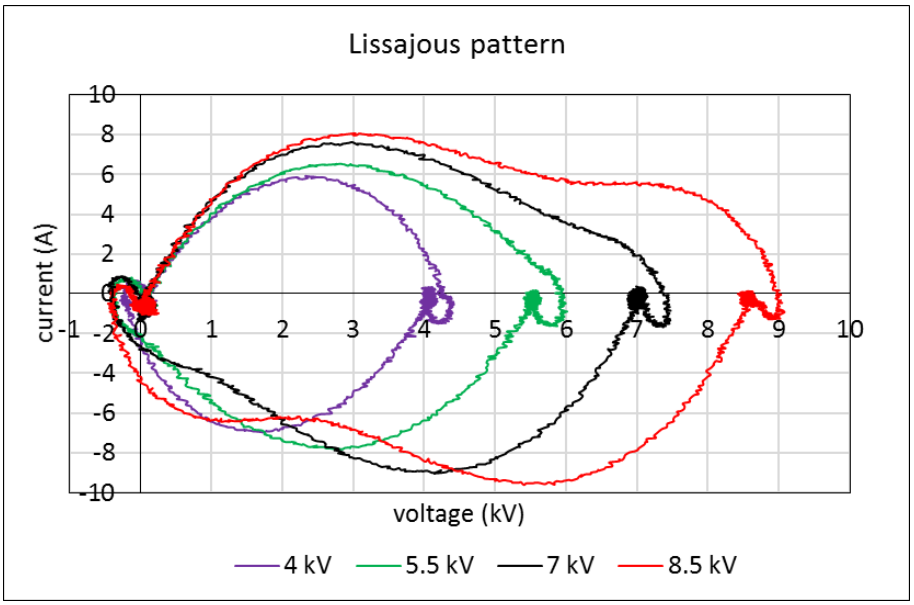

Figure 36. Lissajous pattern of the APPJ for different applied voltages. The surface area of the curves shows the total dissipated power in both the APPJ device and the plasma plume. (*f*: 7 kHz, P.W: 1µsec, flow rate: He, 7 slm)

The power includes the plasma bullet generation power and the power loss in the circuit. The energy per cycle, E_{el} and the power, P_{el} can be found by equations (24) and (25) [52].

$$E_{el} = \int V(t)I(t)dt \tag{24}$$

$$P_{el} = \frac{1}{T}E_{el} = f.E_{el}. \tag{25}$$

Where f is the frequency of the applied voltage. In Figure 37, the influence of the applied voltage on the consumed energy in the first plasma bullet, the second plasma bullet, and the total energy per cycle is shown. The figure shows that the magnitude of the total energy per cycle increases by increasing the applied voltage.

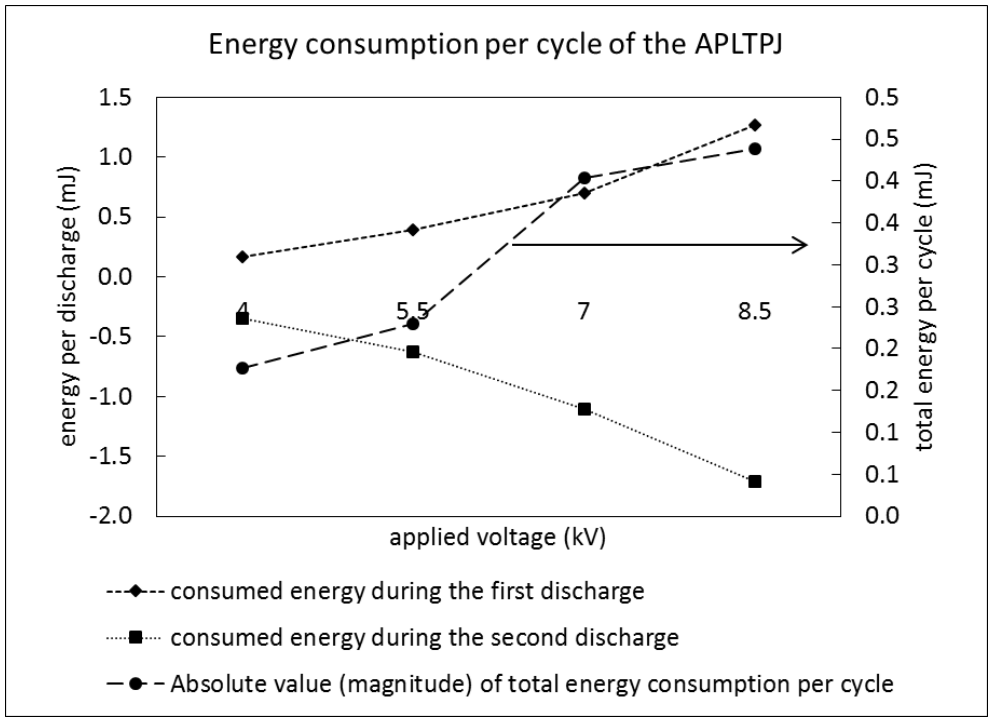

Figure 37. The effect of the applied voltage on the consumed energy of the APPJ during the development of the first plasma bullet, the second plasma bullet and the magnitude of the total energy per cycle. The negative value of the energy for the second plasma bullet is due to the inverse current of the plasma jet.

Spatiotemporal-Resolved Total Charge Measurements (Annular D-dot probe)

The variation of dE/dt in the vicinity of the probe is directly proportional to the induced current on the probe. What we measure is the current going through the resistor in series with the D-dot probe. Therefore, integrating the signal gives us the electric field intensity on the surface of the probe. Figure 38 shows an example of the measured signal and the integral of the signal that is equivalent to the electric field intensity when the probe is placed at a fixed location close to the running APPJ without discharge (the helium was cut off). The reason for the similarity of the probe current signal to the current of the APTLPJ electrode is that at a fixed location, the electric

field intensity only depends on the magnitude of the electric charge on the surface of the jet electrode that is a linear function of the applied voltage.

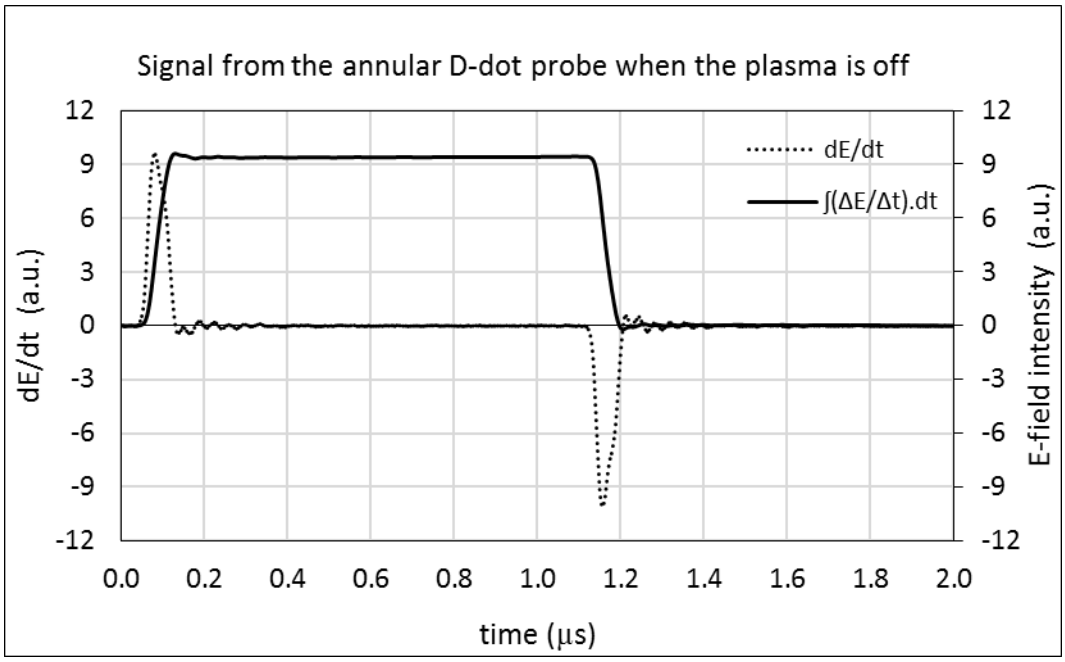

Figure 38. An example of the measured signal by an annular D-dot probe and its integral over time representing the electric field intensity variation over time when plasma is OFF. The signal is due to the applied voltage on the jet electrode (applied voltage: 7 kV, repetition rate: 7 kHz, flow rate7 slm, and pulse width: 1 μs).

We divided the plasma plume from the jet electrode (z=0 mm) up to z=42 mm into 15 points with equal distance of 3 mm from the adjacent points. To simplify the problem and to reduce the number of the equations, we assumed that farther ahead of the plasma streamer head is a neutral space. Therefore, we obtained the location of the plasma streamer head versus time by photographing the propagation of the plasma bullet with the ICCD camera. The result that is shown in Figure 39, also indicates the length of the plasma plume over time.

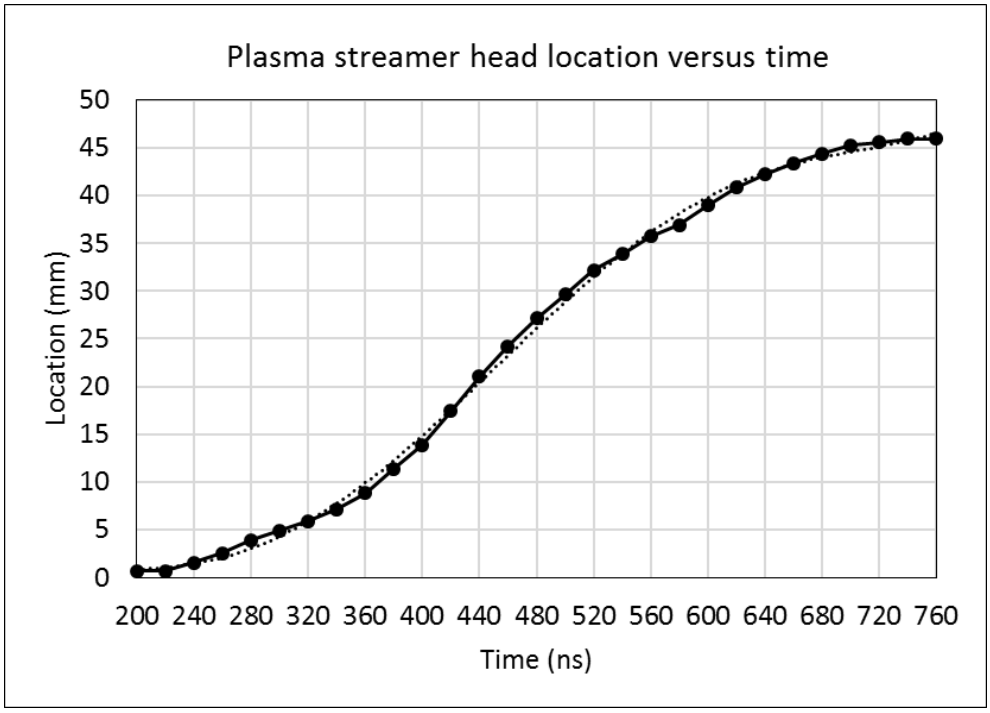

Figure 39. The location of the plasma streamer head versus time. The applied voltage starts at t=0 ns and the plasma bullet starts propagating at t=200 ns.

To investigate the effect of the net charge of the plasma plume on the probe, we subtracted the induced charge due to the electric field of the electrode from the measured total charge. Then, we assumed that the electric potential around the electrode is constant due to the equipotential condition on the jet electrode that was connected to the high-voltage power supply. The power supply is responsible to maintain the equipotential condition on the surface of the electrode. We also assumed that the electron diffusion was limited inside the volumetric arrays of the model. The first result of the measurement is shown in Figure 40 from the start time of the plasma bullet propagation at 200 ns to 360 ns. The solid line in Figure 40 indicates that at the time of the initiation of the ionization wave, the seed electrons are attracted towards the APPJ and leave charged species behind in the gas channel. The seed electrons and the charged species exist around the gas channel due to the previous discharges. At 270 ns, the discharge occurs and the

electrons are attracted to the closest point to the electrode and the equipotential condition of the electrode cancels out the net charge. Therefore, at any time, an equal amount of negative charge and positive charge is in the system. The electrons are accumulated at point z=0 mm (on the surface of the tube and close to the electrode edge) and an equal positive net charge is left in the gas channel. According to the fast images and the D-dot probe results, at 270 ns to 360 ns, the plasma bullet becomes more intense toward the tube exit and forms a faster plasma bullet outside of the tube that propagates along the gas channel. In addition to the volumetric discharge along the gas channel, we observed a long-lasting surface discharge process inside the tube. Figure 40, Figure 41, and Figure 42 show that there are two separate regions, one inside the tube and another one outside the tube related to the surface discharge and the volumetric plasma bullet, respectively.

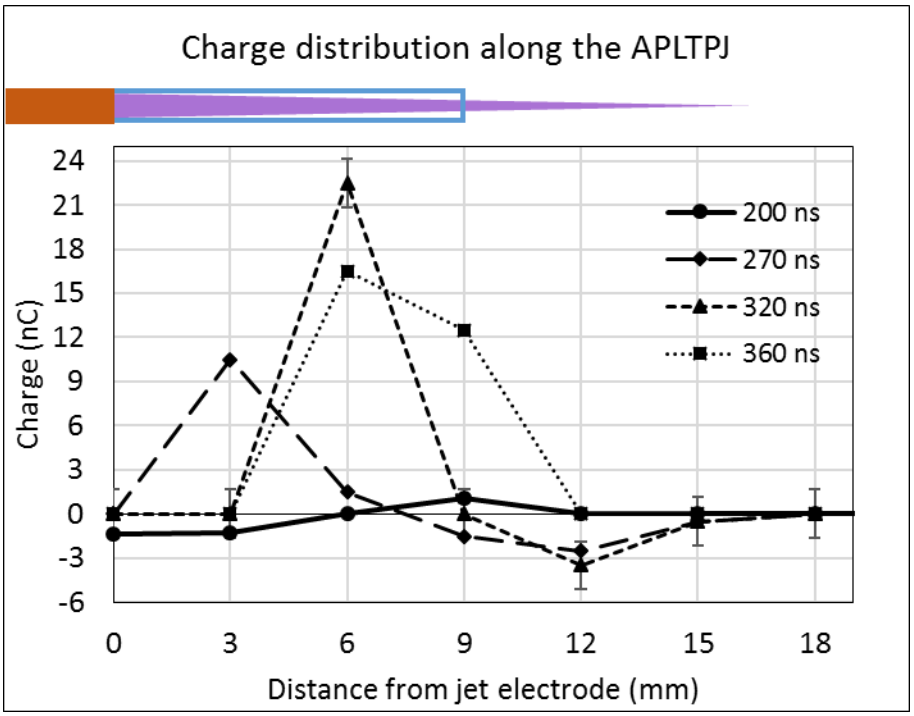

Figure 40. The net charge (Q_++Q_-) distribution along the gas channel during the first discharge from 200 ns to 360 ns (applied voltage: 7 kV, repetition rate: 7 kHz, flow rate7 slm, and pulse width: 1 µs).

Figure 41 shows the continuing process of the plasma plume propagation. The results show that a large amount of net positive charge is trapped inside the jet tube (the tube head is located at point z=9 mm). Outside of the tube, the net charge has a growing pattern behind the streamer head.

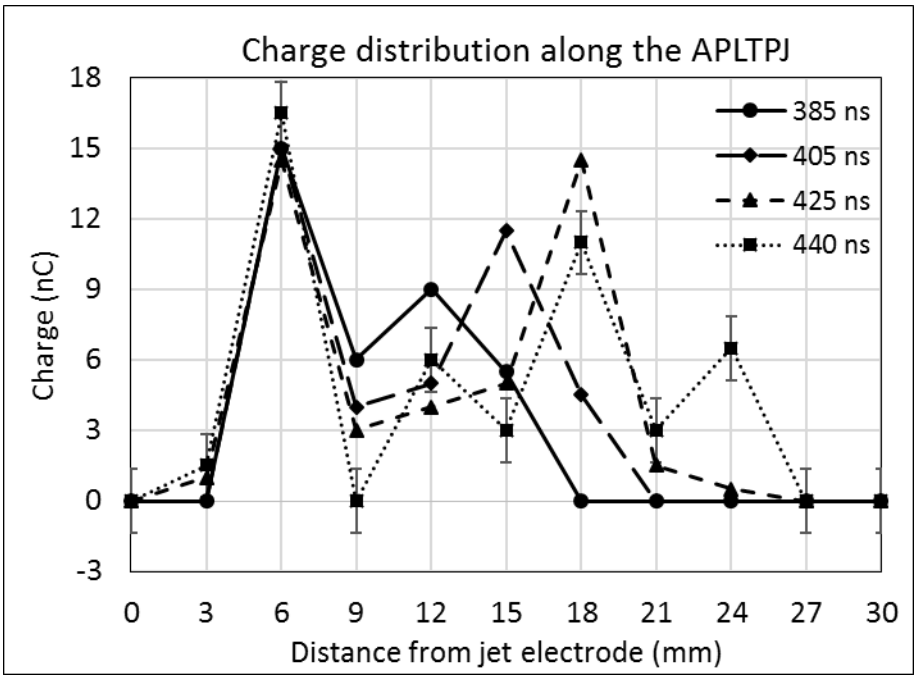

Figure 41. The net charge distribution along the plasma plume during the first discharge from 385 ns to 440 ns (applied voltage: 7 kV, repetition rate: 7 kHz, flow rate7 slm, and pulse width: 1 μs).

In Figure 42, it is clear that during the plasma plume development, the peak points spread over the gas channel. The maximum value occurs between the electrode and the tip of the jet tube. This is the point at which the concentration of the air molecules increases, and the ionization ratio is at its maximum within the gas channel. The minimum net charge happens at the exit of the nozzle. One hypothesis is about the maximum rate of the negative ions production at that location. In the next chapter we will measure the production rate of the negative ions in the plasma plume and discuss it further.

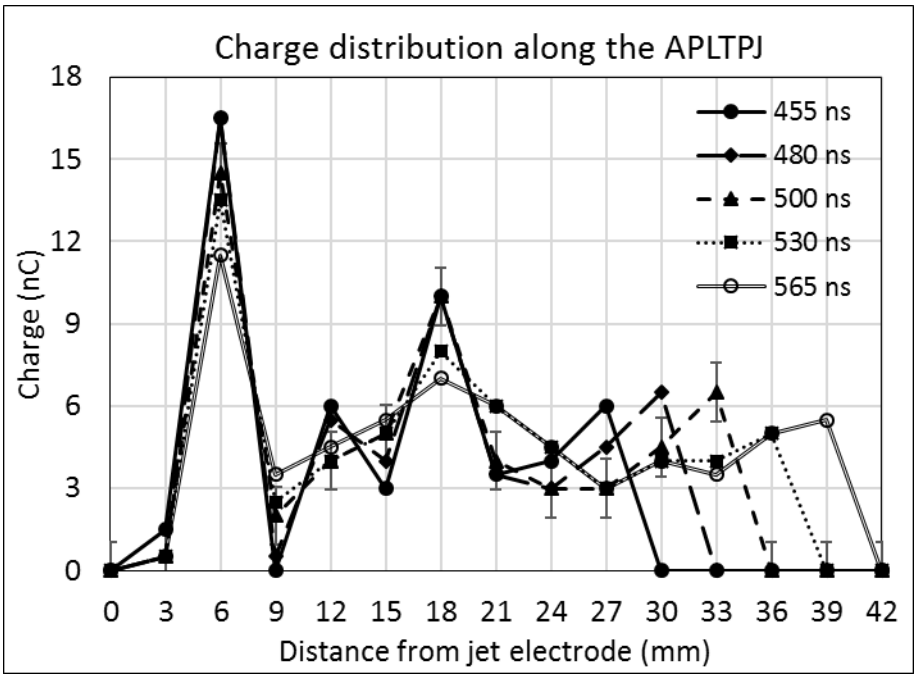

Figure 42. The net charge distribution along the plasma plume during the first discharge from 455 ns to 565 ns (applied voltage: 7 kV, repetition rate: 7 kHz, flow rate7 slm, and pulse width: 1 μs).

The net charge is the summation of the negative species and the positive species. Therefore, the ionization process does not affect the magnitude of the net charge due to the quasineutrality at the discharge point. Although the streamer head has a sizable electric field intensity, it cannot be measured by the D-dot probe because of the plasma quasi-neutrality.

Figure 43 shows the total net charge which is the summation of the net charge along the entire channel and the streamer head location versus time. As we assumed at the beginning, the probe is not able to measure the magnitude of the negative charge inside the electrode due to the equipotential shielding of the electrode. Regarding the high conductivity of the plasma plume, we can assume that an equivalent number of electrons accumulate on the dielectric surface of the jet tube. The accumulated electrons are responsible for the second discharge at the fall time of the high-voltage pulse.

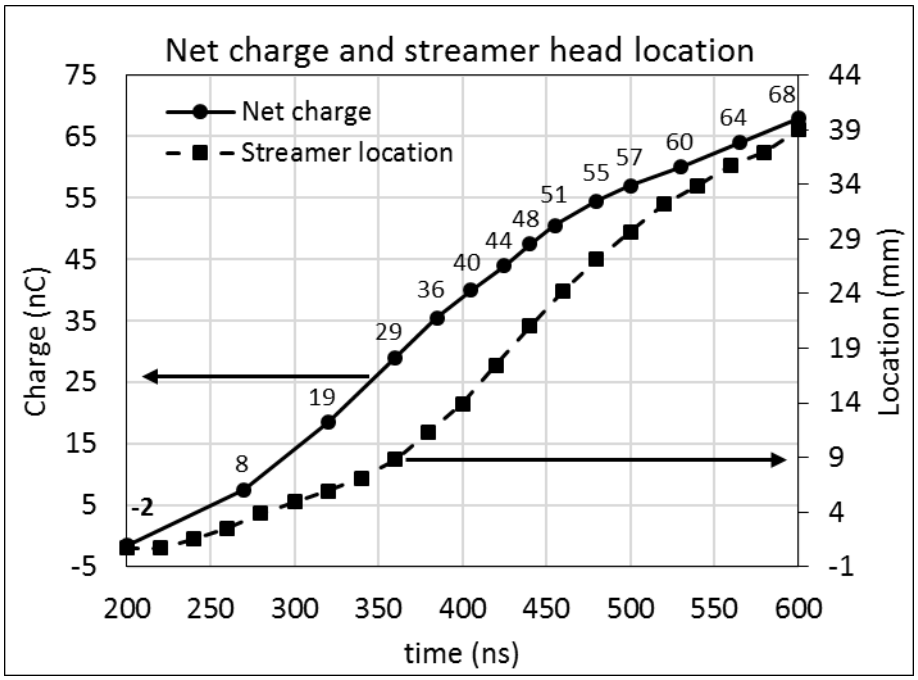

Figure 43. The summation of the net charge distribution along the plasma plume during the first discharge and the location of the streamer head versus time. (Applied voltage: 7 kV, repetition rate: 7 kHz, flow rate7 slm, and pulse width: 1 µs).

We also measured the discharge current and calculated the total charge on the electrode by means of the Rogowsky coil. The method of calculating the total charge on the electrode was similar to the method of the surface charge measurement that was mentioned in the previous section. Instead of using a resistor in series with the high-voltage electrode to measure the current, we used the Rogowsky coil with a relatively higher accuracy. The Rogowsky coil measures the current that goes through the high-voltage electrode. By integrating the electrode current over time, we can calculate the total charge on the electrode. The result in Figure 44 shows that the measurement of the net charge by the annular D-dot probe has an acceptable accuracy. In the figure, at the start time of the pulse, a net charge of 2.2 nC is brought on the electrode from the power supply which is roughly equal to the measured surface net charge next to the electrode edge inside the jet tube by the annular D-dot probe. The maximum amount of

total charge on the electrode also indicates that an equal opposite charge (the attracted electrons from the plasma plume and by the electrode E-field) accumulate inside the jet tube during the plasma plume propagation.

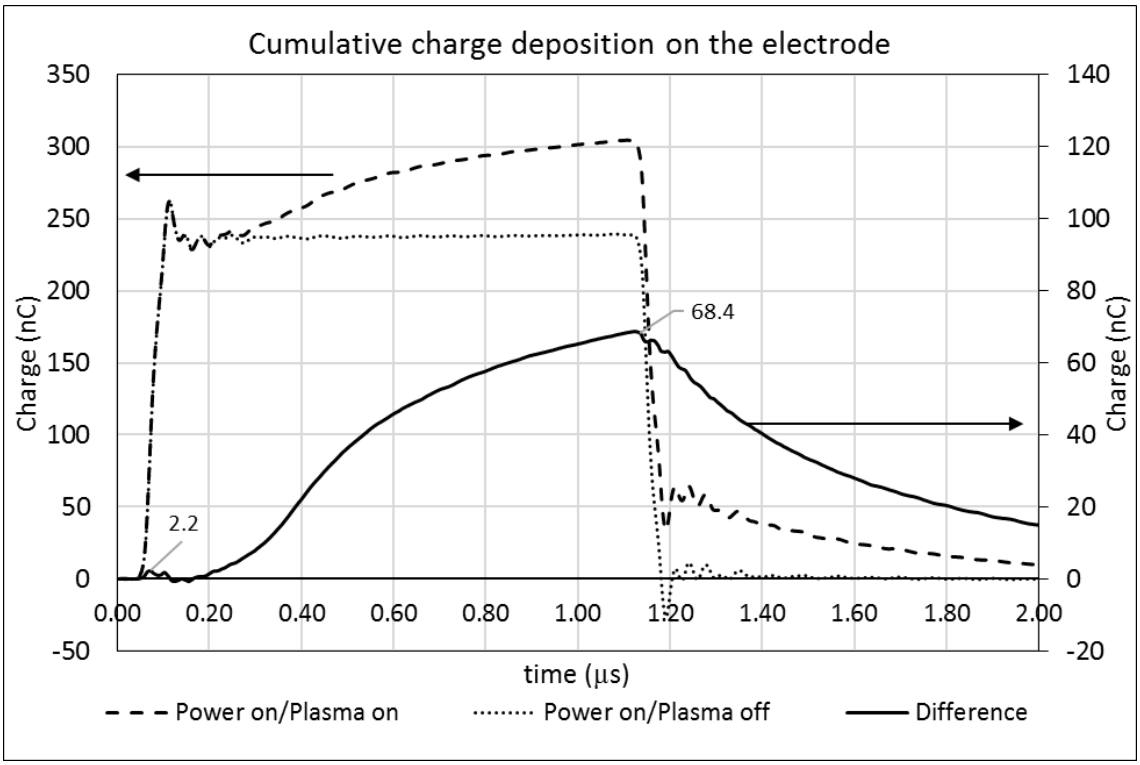

Figure 44. The waveform of the measured net electric charge on the electrode by means of the Rogowsky coil indicating the positive net charge at the very beginning to maintain the equipotential condition due to the accumulation of the seed electrons inside the jet tube and (applied voltage: 7 kV, repetition rate: 7 kHz, flow rate7 slm, and pulse width: 1 μs).

The charge accumulation trend over time in both Figure 43 and Figure 44 shows that a certain fraction of the generated electrons in the plasma plume are attracted inside the tube during the propagation process. The magnitude of the electric charge of the accumulated electrons in the tube is equal to the magnitude of the total charge on the electrode due to the capacitive structure of the APPJ. As it is shown in Figure 43, the electric charge due to the seed electrons that causes the discharge initiation is about -2.2 nC in this case.

IV.2.2 Single-Electrode Plasma Jet and Dielectric Obstacle

I-V measurements

We measured the APPJ voltage and current while a dielectric obstacle was placed in front of the plasma plume similar to the configuration mentioned in chapter 3. The waveform of the current was very similar to when there is only plasma jet propagating into air without the obstacle in front of it. The exit tube of the APPJ was placed 6 mm away from the dielectric surface and the parameters were fixed at the applied voltage of 7 kV, repetition rate of 7 kHz, pulse width of 1µs, and gas flow rate of 7 slm (Figure 45).

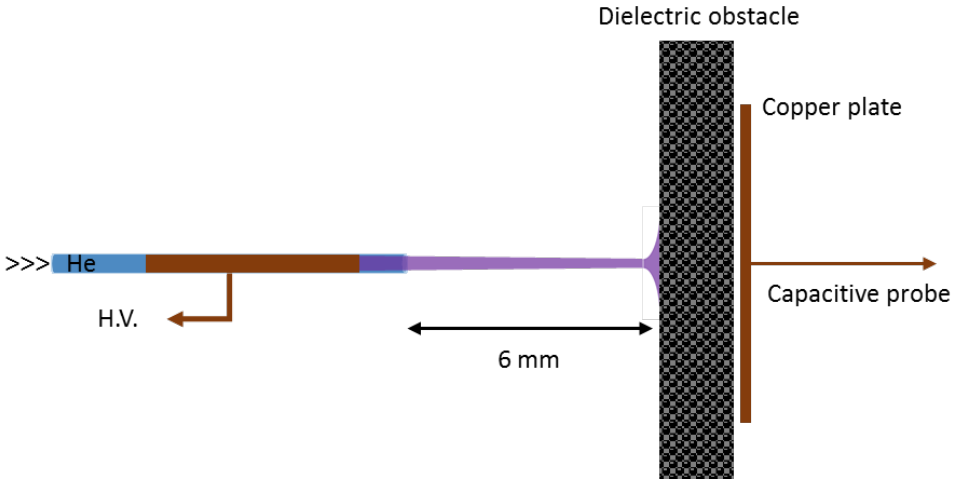

Figure 45. The schematics of the orientation of the APPJ in the vicinity of the dielectric surface. The distance between the exit tube and the surface of the dielectric was 6 mm (Applied voltage: 7 kV, repetition rate: 7 kHz, pulse width: 1 µs, and He flow rate: 7 slm).

Comparing the results of the energy consumption in this case (shown in Figure 46) with respect to the APPJ without any obstacles that was shown in the previous section indicates a different trend during the second discharge (discharge occurring during the falling edge of the applied voltage pulse). In the second discharge, the amount of the energy per cycle decreases by

increasing the applied voltage. Therefore, the total energy per cycle reduces at higher applied voltages. One hypothesis is due to spreading of the plasma plume over the dielectric surface and charge deposition over the surface. The second reason can be due to the greater ionization ratio even at lower voltages during the first discharge process in this case. This can be confirmed by the larger values of the energy dissipation at the second discharge with respect to the result in Figure 37.

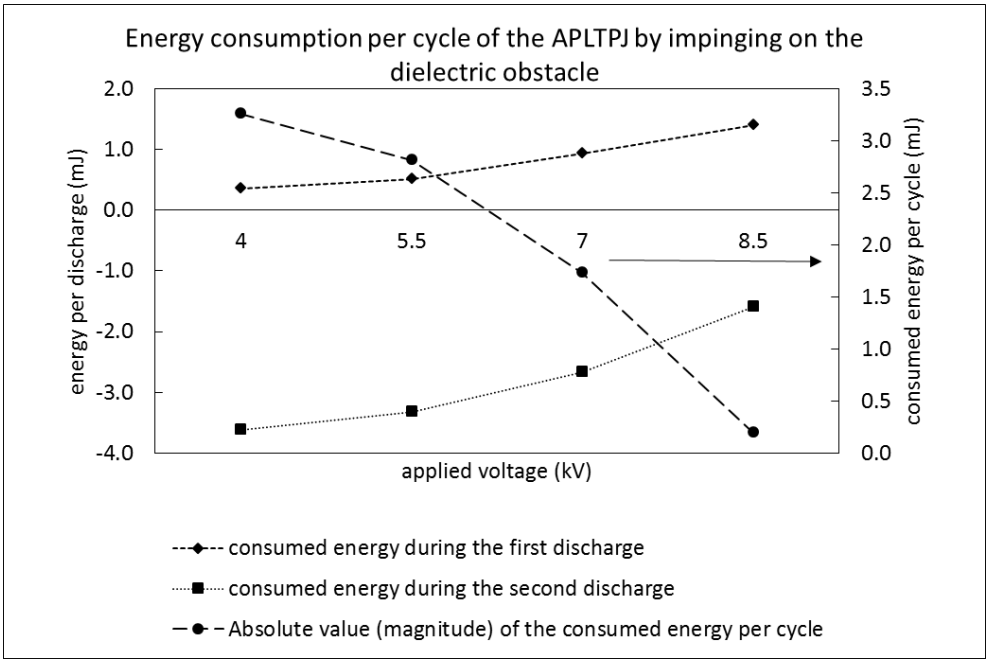

Figure 46. The effect of the applied voltage on the energy consumption of the APPJ during the development of the first plasma bullet, the second plasma bullet and the magnitude of the total energy per cycle when a dielectric obstacle is placed in front of the APPJ. The negative value of the energy for the second plasma bullet is due to the inverse current of the plasma jet.

We also investigated the current peaks in two conditions with and without dielectric obstacle. The results are shown in Figure 47. The results show that the APPJ without any blocking material in front of it has a linear response to the applied voltage. Putting a dielectric obstacle in

front of the APPJ limits the effect of the applied voltage may be due to blocking the diffusion of air into the jet tube.

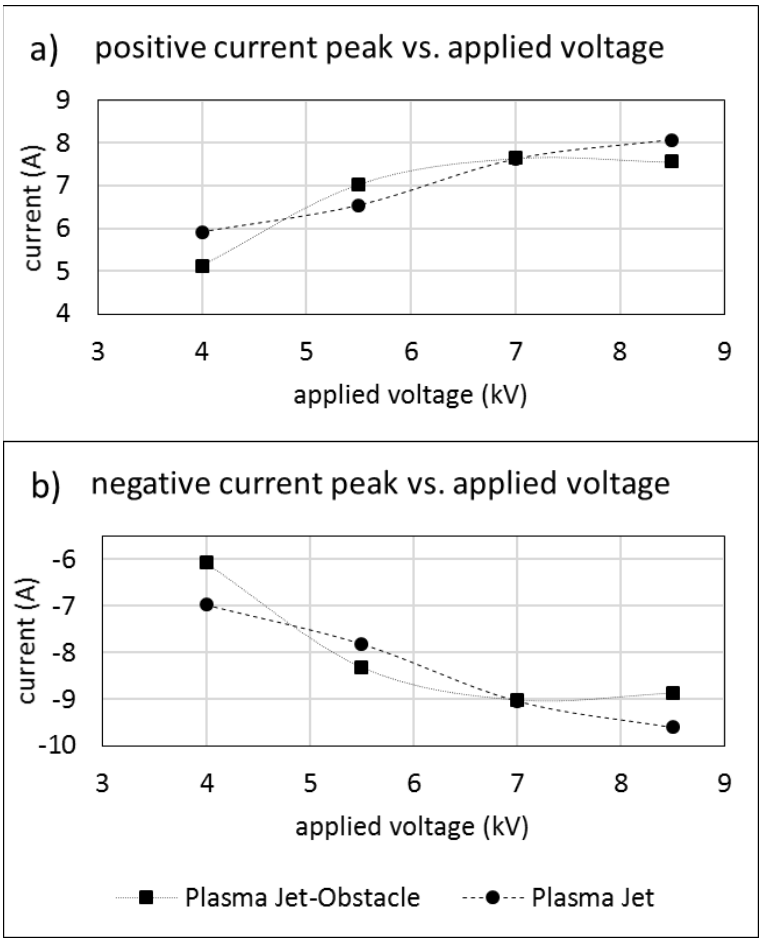

Figure 47. The effect of the dielectric obstacle presence on the APPJ current versus different applied voltages (Distance between the plasma jet and the dielectric surface: 6 mm, *f*=7 kHz, P.W.: 1 µs, Flow rate: 7 slm).

Surface Charge Measurements (Capacitive Probe)

We measured the current through a resistor that was connected in series with a copper plate attached to the surface of the dielectric obstacle as it was shown in Figure 29. The total capacitance of the circuit was about 170 pF according to the response time of the circuit. In Figure 48, the current through the attached plate to the dielectric surface is shown. The first

current peak refers to the applied voltage to the APPJ device and the second peak shows the current related to the plasma plume approaching the surface, impinging on it, and finally decaying over the surface. The applied voltage affects the length of the plasma plume and the speed of the plasma bullet. Figure 48 represents that the current peak value and the current peak time are enhanced for increasing the applied voltage. The prominence of the second peak strongly depends on the speed of the plasma bullet and its lasting time. At 4 kV, the length of the plasma plume is not enough to get to the surface of the dielectric obstacle and gas flow is responsible for the transport of the charged species while at 8.5 kV the plasma bullet itself has a considerable ionization rate in the vicinity of the dielectric surface.

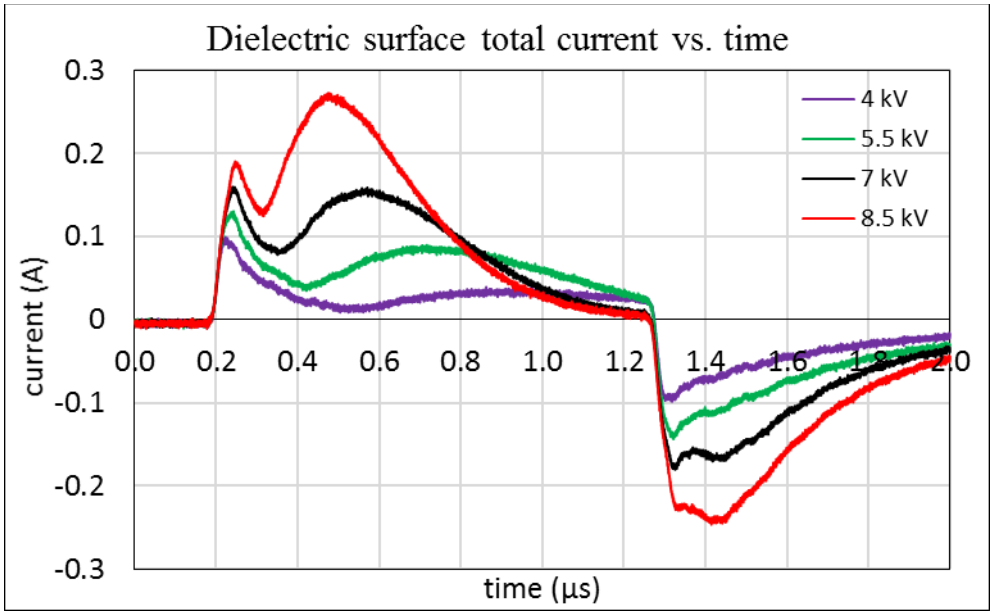

Figure 48. The effect of the applied voltage on the total induced current on the surface of the dielectric by the jet electrode and the plasma plume (*f*=7 kHz, P.W.: 1 µs, Flow rate: 7 slm).

Figure 49 shows that the induced current through the plasma plume strongly depends on the applied voltage. It also indicates the speed of approaching the plasma bullets onto the dielectric surface. Comparing the current peaks of the jet electrode and the plasma bullets in Figure 49 and

Figure 48 give us useful information about the contribution of each one on the induced charge on the dielectric surface. Increasing the applied voltage enhances the contribution of the plasma bullets in inducing electric charge on the dielectric surface. It also helps the plasma bullets reach to the surface faster by comparing the timing of the current peaks.

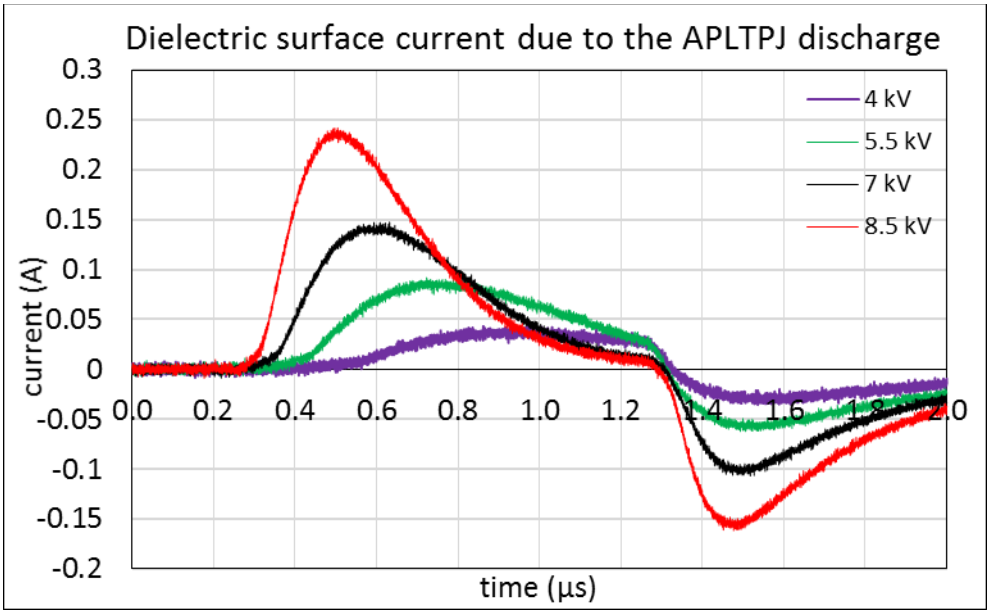

Figure 49. The induced current on the surface of the dielectric due to the plasma plume with different applied voltages (*f*=7 kHz, P.W.: 1 µs, Flow rate: 7 slm).

In Figure 50 and Figure 51, the charge accumulation on the surface of the dielectric is calculated by integrating the current profiles over time considering the configuration of the measurement circuit. The total induced charge on the surface of the dielectric due to the jet electrode increases linearly by increasing the applied voltage. The contribution of the plasma plume is more sizable than the jet electrode.

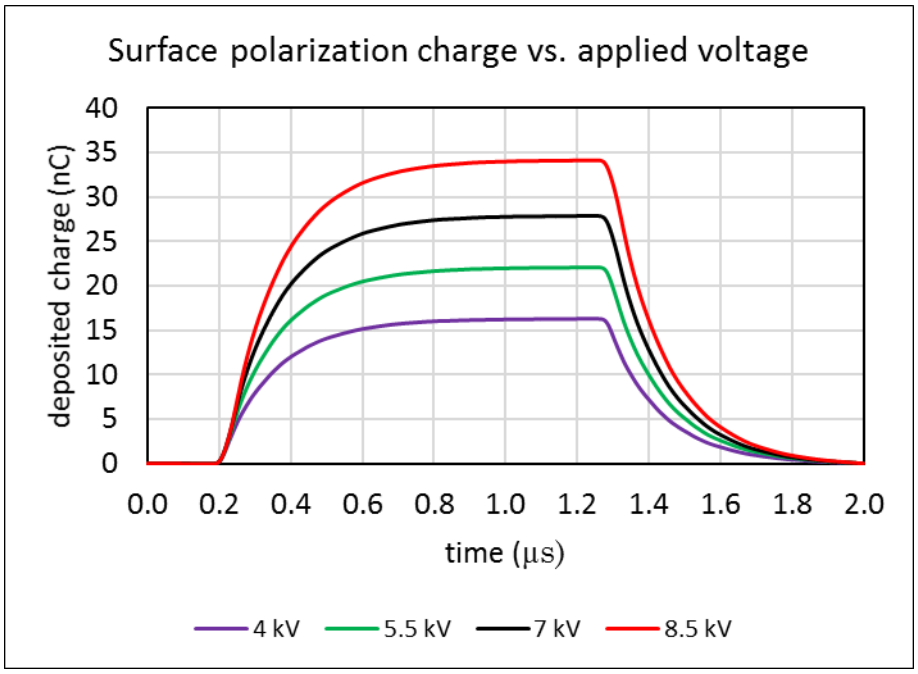

Figure 50. The measured surface polarization charge on the dielectric surface over time due to the electric field of the running APPJ with plasma OFF (*f*=7 kHz, P.W.: 1 μs, Flow rate: 7 slm).

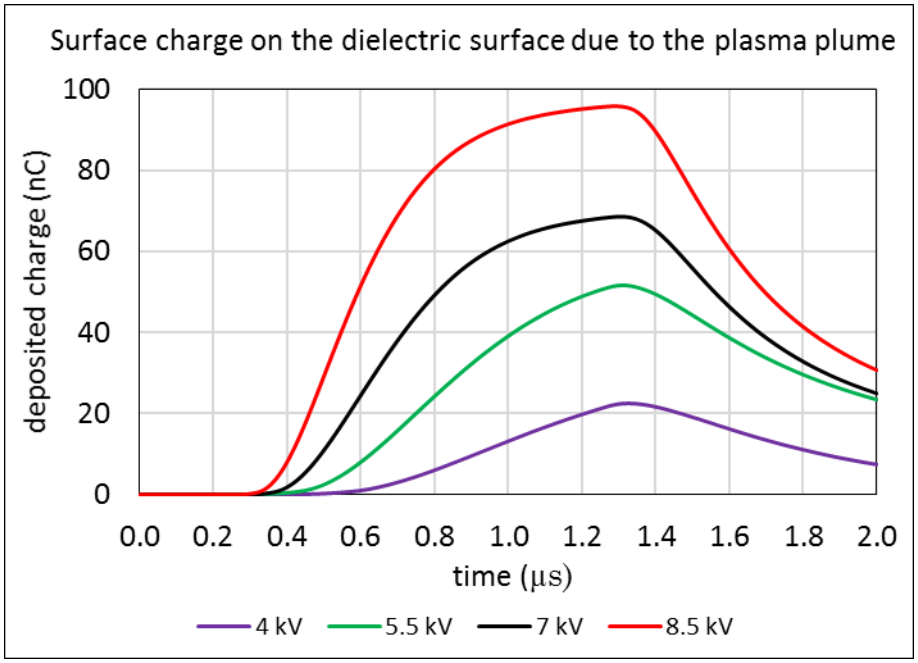

Figure 51. The measured surface charge due to the impinging plasma plume on the dielectric surface vs. time with different applied voltages (*f*=7 kHz, P.W.: 1 μs, Flow rate: 7 slm).

Two reasons are responsible for the big contribution of the plasma plume on the induced charge over the surface of the dielectric. The first reason is due to the transport of a sizable electric field intensity at the streamer head very close to the surface. The second reason is due to the spread of the plasma plume over the surface and a positive charge deposition in the vicinity of the dielectric surface

We also assessed the effect of the gas flow rate on the surface charge on the dielectric target. As it is shown in Figure 52, increasing the gas flow rate enhances the surface charge. Our hypothesis is that increasing the gas flow rate makes a larger volume with high helium content around the dielectric target that enhances the ionization rate and the length of the plasma plume that spreads over the dielectric surface.

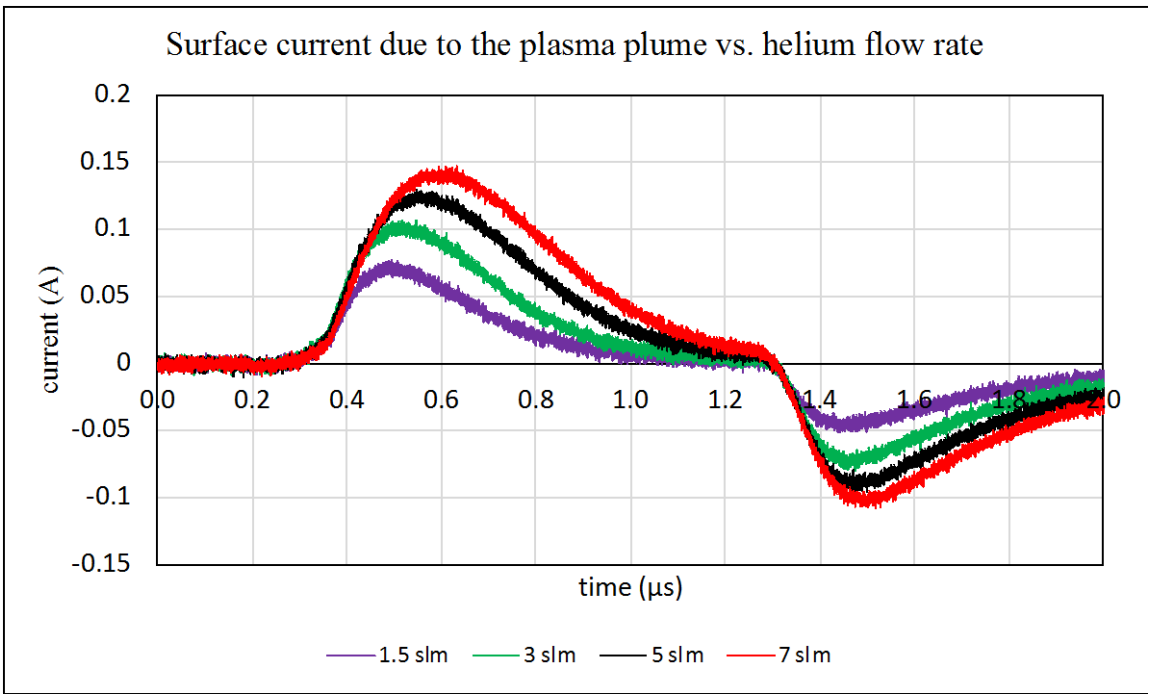

Figure 52. The induced current on the surface of the dielectric due to the plasma plume with different helium flow rates (Applied voltage: 7 kV, *f*=7 kHz, P.W.: 1 µs).

From Figure 52, we extracted the peak time of the induced current on the surface of the dielectric target versus time. The result represents a lag in the current peak time by increasing the gas flow rate. The equal rising slopes of the curves at various applied voltages show a constant rate of current increment on the dielectric surface and the only difference that was observed by the fast imaging was the radius of the surface discharge that enhances the current peak. By increasing the gas flow rate, we increase the radius of the surface discharge on the dielectric surface that intensifies the induced current. Therefore, the current peak time of the surface discharge occurs when the plasma spreads completely over the surface.

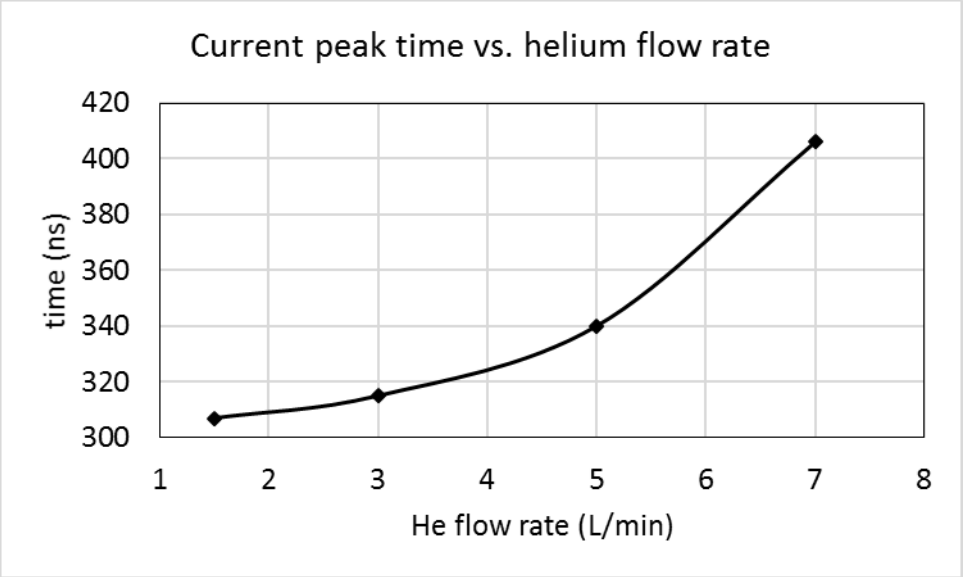

Figure 53. Induced current peak time versus helium flow rate (Applied voltage: 7 kV, *f*=7 kHz, P.W.: 1 μs).

We also studied the effect of the distance and the applied frequency. By increasing the distance of the APPJ from the surface of the dielectric surface, the induced charge decreases dramatically and also the current peak occurs with a delay because of the greater distance and the decrease of the plasma plume velocity. Increasing the applied frequency causes a faster plasma plume formation and it was observed that the measured current waveform was similar in every case.

The time of the plasma bullet formation was 60 ns faster by changing the applied frequency from 3 kHz to 9 kHz.

Finally, we chose the most suitable applied voltage of 7 kV and the distance of 6 mm in order to have the lowest effect of the jet electrode and the greatest effect of the plasma plume on the generation of the diffuse plasma at the low-pressure side of the dielectric surface. Decreasing the applied voltage weakens the plasma plume electric field intensity as well as its velocity. Increasing the applied voltage too much could ignite the ionization wave inside the low-pressure chamber, which was not desirable. Likewise, the too close and too far distances could adversely affect the contribution of the plasma plume on the generation of the ionization wave inside the low-pressure side of the chamber.

IV.2.3 Transient Diffuse Plasma

Langmuir Probe

The Langmuir probe was placed in the bulk of the reduced pressure plasma to measure the electron density and the electron temperature. An example of a Langmuir I-V curve is shown in Figure 54. Measurement without proper shielding was tried as well as with a glass tube shielding. The measurement without shielding did not give us a specific value for the saturated electron current as it can be seen in Figure 54. The glass tube shielding provided us with a more precise I_{es}, but the expected plateau at the right tale did not follow a normal pattern. A more

accurate pattern was achieved by averaging the measured signal from the unshielded probe and the shielded one.

Figure 54 shows the Langmuir curve of the bulk of air plasma at a pressure of 400 mTorr. The APPJ was placed 6 mm away from the outer wall of the chamber. In order to find the electron temperature, we used Eq.(20). To simplify the calculation of m_i, air content can be assumed as N_2. Therefore, $m_i \approx m_{N_2} = 28\ a.m.u.$. For the helium plasma, $m_i = m_{He} = 4\ a.m.u.$.

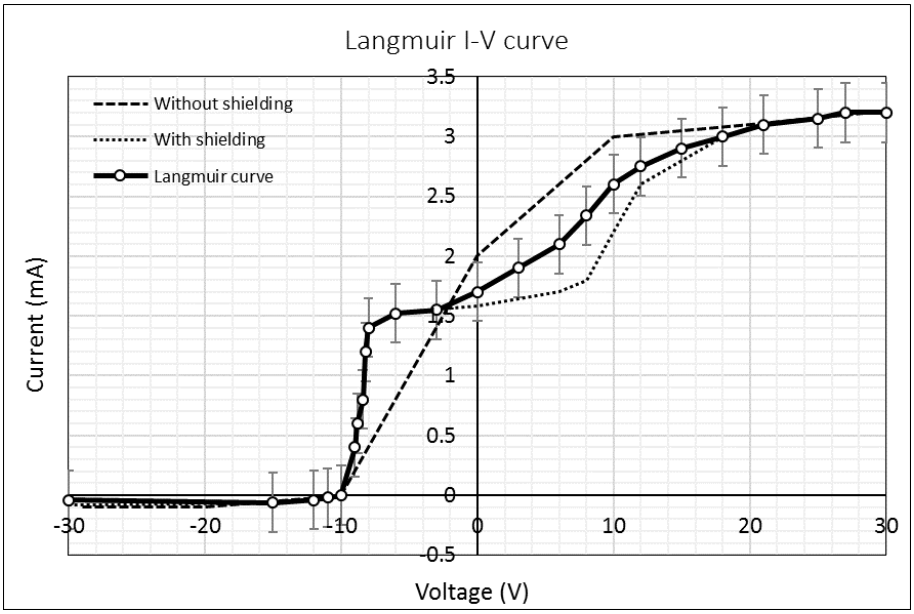

Figure 54. An example of an I-V curve of plasma positive column filled with air at a pressure of 400 mTorr.

$$T_e = 25{,}600\ \text{K} = 2.2\ \text{eV}$$

$$n_e = 1.624 \times 10^{16}\ \text{m}^{-3}$$

$$\lambda_D = \sqrt{\frac{\varepsilon_0 k_B T_e}{e^2 n_e}} = 86.7\ \mu m \tag{26}$$

The left-hand side tail of the curve in Figure 54 is about -40 μA which is a very small value with respect to the DC power supply precision and not reliable. Therefore, it is not going to be considered in future calculations. It indicates the saturated ion current and the ion number density can be extracted from it by the Bohm current equation and it is valid when $T_i \ll T_e$. Although, in the quasi-neutrality condition, the ion number density is expected to be equal to electron number density [53, 54].

Generally, negative plasma potential is an unexpected result of the I-V graph in Figure 54 while most of the quasi-neutral plasmas with a common grounded container is expected to have a positive potential in the bulk of plasma. The main reason that explains the negative plasma potential in this type of plasma is that since the chamber wall is non-conductive and there is no electrode in the container and no conductive grounded surface around the plasma expansion region, there is no dramatic electron loss from the bulk [55].

Heinisch et al. studied the phonon-mediated absorption of the electrons at SiO_2 surface as a dielectric material. They show that electrons with the mean energy more than 1 eV have a sticking coefficient at a factor of 10^{-4} at the surface temperature of 300 K [56, 57]. In another report, they show that electrons are trapped temporarily in the surface layer of dielectric due to a growing number density of electrons over time [58]. Moreover, ions are attracted to the dielectric surface and recombine with the electrons. This indicates that a dielectric container is similar to a negatively biased surface with a reduced loss of electrons from the bulk of plasma [59]. Under a negatively biased substrate and supplemental electrons emitting from the substrate, the plasma electric potential becomes negative [55, 60]. Hershkowitz reported a negative plasma potential in

a multidipole chamber with a dielectric coated plasma boundary. In this experiment, the discharge type was electropositive plasma similar to our experiment. He explained the reason of the negative potential was because of the balance between electron creation and loss and the mechanism for negative dielectric wall charging. [61]

We also observed the electron current by measuring the differential voltage across a resistor in series with unbiased Langmuir probe connected to the input channel of the oscilloscope similar to Figure 30. The peak value in the measured signal provides the electron saturation current, I_e, for the chamber filled with air at 0.3 Torr, I_e=1.7 mA and when it is filled with helium I_e=6 mA. By using equation (21) it was found that the helium to the air discharge current ratio is 3.53. Therefore, considering the electron temperature in a helium/air plasma to be $T_e = 2.73\, eV$, the electron density in the helium discharge at 0.3 Torr is

$$n_e = 6.38 \times 10^{16}\ m^{-3}$$

By knowing the electron density, from Eq.(22), the plasma frequency can be calculated.

$$\omega_p = 7.20 \times 10^{9}\ \text{Hz} = 7.20\ \text{GHz}$$

The current through the probe reaches a plateau after a few microseconds and that is the maximum current flux of the probe. Increasing the pulse width at the APPJ side will lead to decreasing the electron saturation current in the chamber over a longer period of time. A lower measured current indicates a lower plasma potential as well as a lower ionization and electron production rate in the bulk plasma. It indicates that the plasma decays after a certain period of

time and it depends strongly on the plasma bullets characteristics as a source of the diffuse plasma.

The electron temperature is directly proportional to the floating potential and the gas type as it is clear from Eq.(20). We did not observe a sensible change in the floating potential by varying the pressure. Therefore, the electron density is a linear function of the saturated electron current in this case. However, the electron density is also correlated to the electron temperature. Figure 55 shows the saturated electron current when the chamber is filled with helium and when it is filled with 70% helium and 30% air.

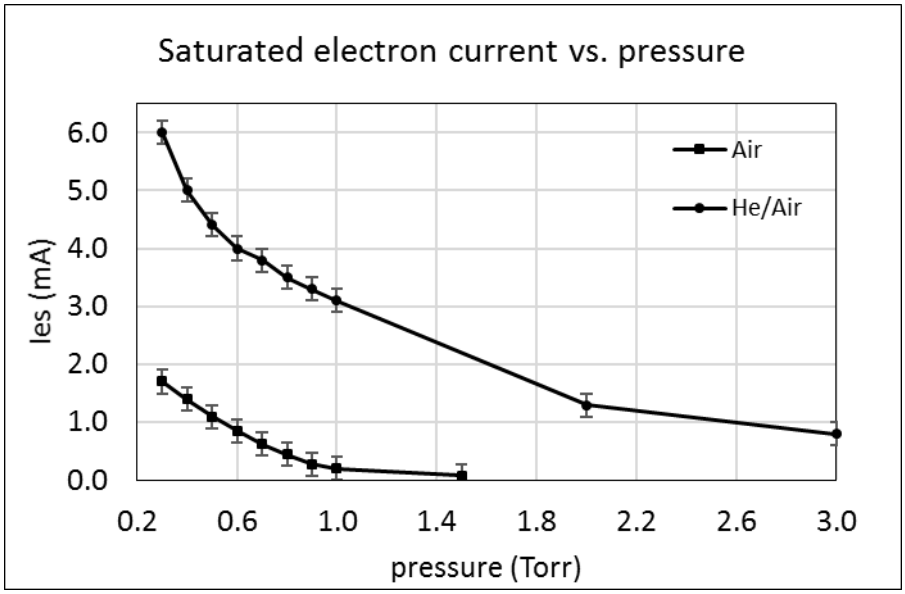

Figure 55. Saturated electron temperature versus pressure in the chamber that was filled with helium and He/Air.

The effect of gas type and pressure on the electron density is shown in Figure 56. Increasing the pressure strongly affects the electron number density as it affects the length of the ionization wave propagation that will be discussed in the next chapter. Electron number density is lower in a medium in which the air concentration is higher due to the quenching impact of oxygen and

nitrogen molecules. The diffuse plasma at higher pressures makes a transition from a diffuse plasma to a corona at which time we could not measure the plasma features. For the diffuse air plasma, the transition occurred above 2 Torr and for the helium/air it happened above 5 Torr.

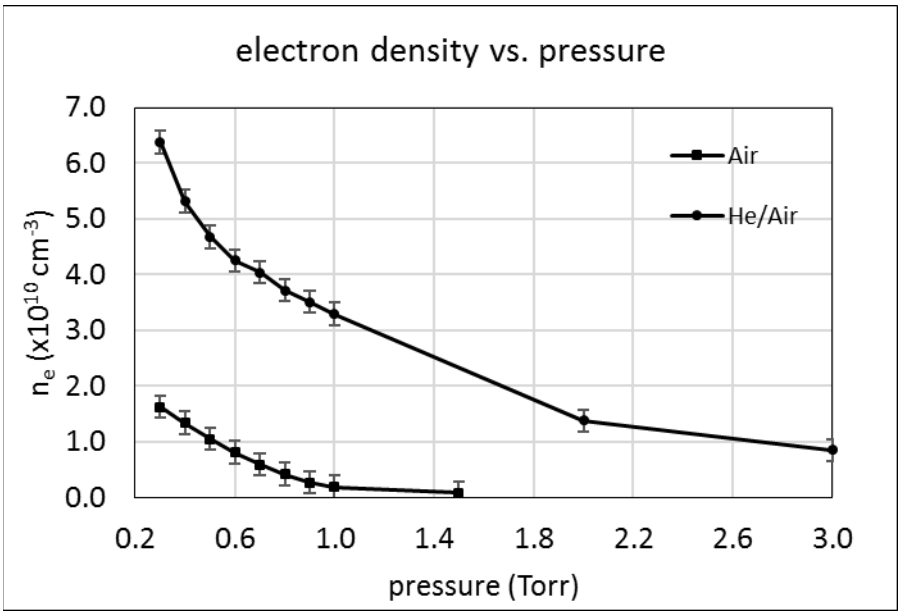

Figure 56. The effect of gas type and pressure on the electron density in the diffuse plasma.

IV.3 SUMMARY

In this chapter, we introduced several methods to study the parameters that affect the operation of the APPJ and their impact on the induced charge on a dielectric surface. This is important since the generation of the diffuse plasma behind a dielectric wall is through capacitive coupling. We developed an annular D-dot probe to study the spatiotemporal measurement of the net electric charge in the plasma plume of the APPJ. We also measured the net induced charge on the surface of a dielectric target by varying the effective operational parameters such as the

applied voltage, the distance between the APPJ and the dielectric surface, the gas flow rate, and the repetition rate. In addition, we measured important plasma features such as electron temperature and electron density inside the low-pressure chamber. The electron temperature and density were found to be higher in a diffuse helium plasma than in a diffuse air plasma.

The results of the interaction of the APPJ and a dielectric obstacle showed that the plasma plume is indeed responsible for initiating the FIW inside the chamber. There are two correlated factors on the magnitude of the induced charge on the dielectric surface. The first factor is the enhanced electric field intensity at the streamer head and the second one is the residual deposited charge on the surface of the dielectric target.

CHAPTER V

SPECTROSCOPIC INVESTIGATIONS

V.1 METHODS

The second part of the present research is about spectroscopic investigations of the APPJ and the low-temperature diffuse plasma. In this chapter, we utilized several experimental setups to investigate the plasma evolution mechanisms in both APPJ plasma and the diffuse plasma. We used spatial optical emission spectroscopy (OES), time-resolved OES spectroscopy, ultra-fast imaging of the APPJ plasma plume and the diffuse plasma, and the measurement of the electric field in the diffuse plasma by Stark splitting technique. The results of the experiments will be discussed in detail.

V.1.1 Spatial and Time Resolved Spectroscopy

Recorded emission spectral data can be used to gain some useful information about the mechanism of the evolution of plasmas. Optical emission spectroscopy (OES) is a widely-used non-intrusive analytical technique of determining the generated chemical species in low-pressure and atmospheric plasmas.

The OES system consists of an Acton research PD-471 photomultiplier tube (PMT), an Acton Research Spectra-Pro 500i monochromator, and a three-meter optical fiber. It has two grating for different ranges of wavelengths. The 3600 g/mm grating is used for UV spectra (200-466 nm) and the 1200 g/mm grating is used for visible and IR spectra (466-1400 nm). The entrance slit of the OES system has a height of 4 mm and an adjustable width of 10-3000 μm. The width of the

entrance slit was adjusted to 150 µm. The measurement resolution and the integration time was adjusted to 0.01 nm and 50 ms, respectively.

Figure 57 shows the schematics of the spatially resolved spectroscopy system and a photograph of the experimental setup. We used a double-convex UV-grade filter at the time of recording visible spectra in order to filter the intense emissions of the second positive system (SPS) of N2 and the first negative system (FNS) of N2+. These emissions cause a higher-order dispersion in the visible spectral range. The aperture radius was 3 mm and it was located between the convex lens and the plasma in order to block unwanted spectra. The distance between the aperture and the lens was 5 cm and the distance between the two lenses was 15 cm. The UV filter was located between two lenses to minimize the aberration.

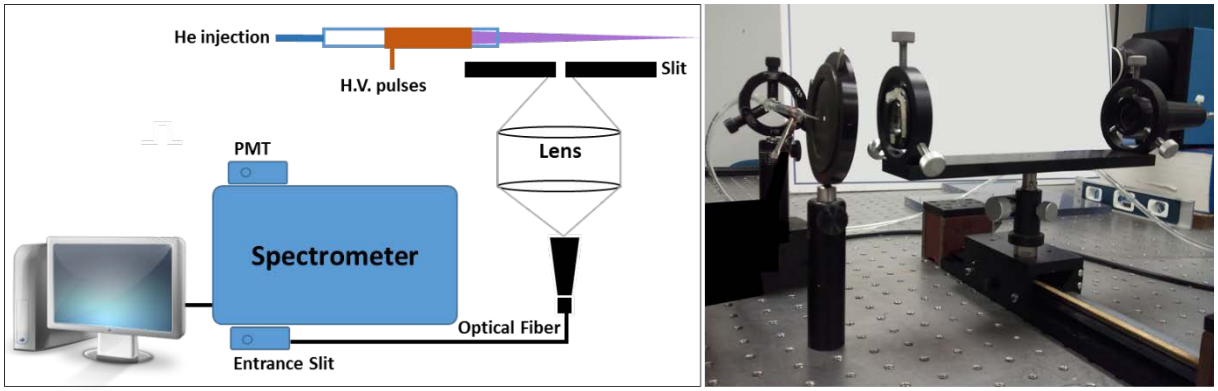

Figure 57. Schematics and experimental setup of the spatially resolved OES method. The optical bundle consists of an adjustable aperture, two convex lenses, and an optical fiber that transmits the beam into the spectrometer. A mounted PMT device was used on the spectrometer.

A complementary method was used to investigate the time-resolved evolution of chemical ingredients of the APPJ plasma. We replaced the PMT with the ICCD by mounting it on the spectrometer as it is schematically shown in Figure 58. The reason that we replaced the PMT with an ICCD is due to the higher quantum efficiency of the ICCD than that of PMT.

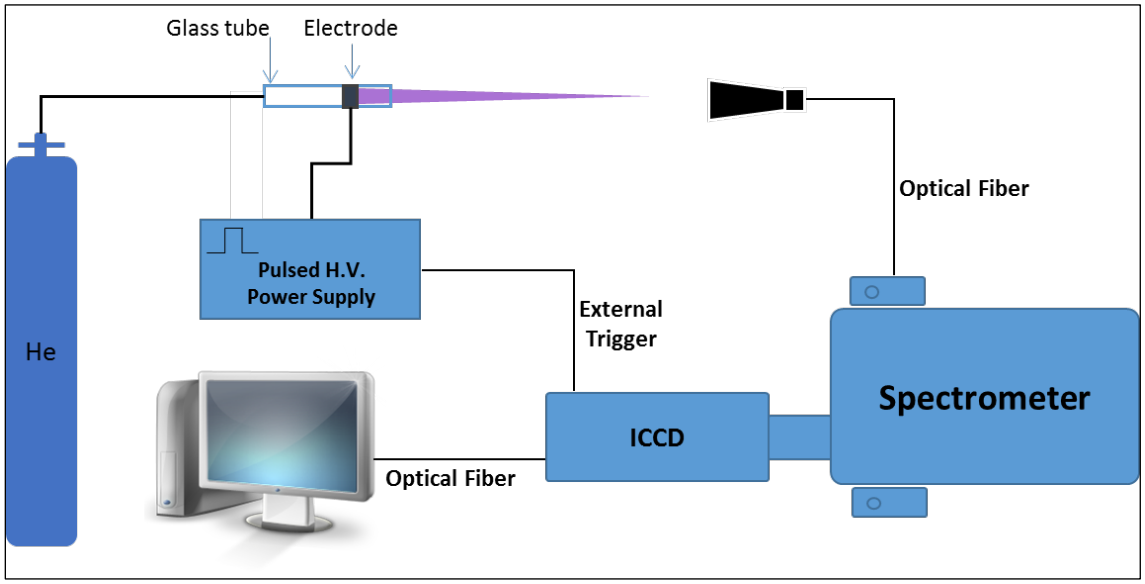

Figure 58. Schematics of the time resolved OES setup. The distance between the lens and the tip of the APPJ was 10 cm. The data acquisition of the ICCD camera was synced by the rise time of the applied voltage. The images were stored on the computer for post analysis.

The ICCD camera was connected to the wave function generator and was triggered by the rise time of the applied high-voltage pulse. The exposure time of the ICCD camera was adjusted to 20 ns. We integrated the collected light from 256 cycles to acquire an adequate intensity at each time interval. Then, we advance to another time step and repeat the operations for 101 times. The delay time was set to 0-2000 ns. We set the phosphor decay time to 10 ms and the gain value to 80%. The short exposure time needs higher gain value and phosphor decay time in order to record a picture with an adequate brightness. For all conditions, the operating temperature of the ICCD camera was set at -15°C according to the operating instructions. The experimental setup is also shown in Figure 59. The distance between the convex lens and the plasma jet was 10 cm in this experimental setup.

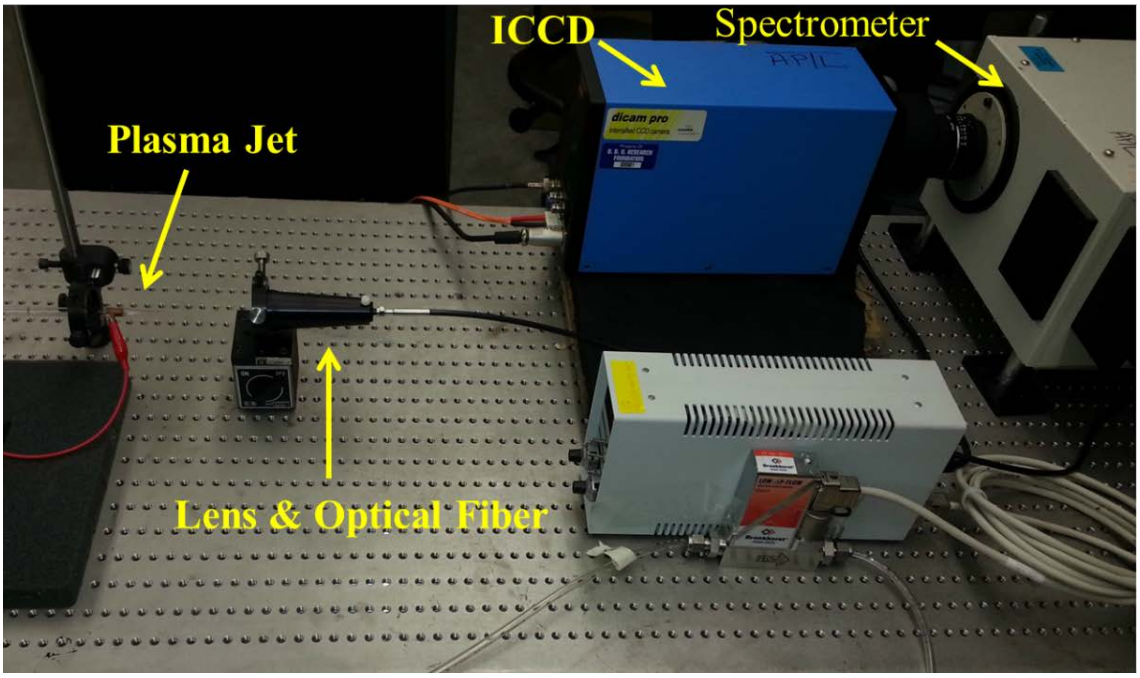

Figure 59. Experimental setup for time-resolved OES. The distance between the lens and the tip of the APPJ was 10 cm. The data acquisition of the ICCD camera was synched by the rise time of the applied voltage.

In this experiment, the spectrometer is locked on a specific wavelength and the exit port is open over the measuring time. Therefore, the ICCD camera can acquire the relative intensity of that specific wavelength with the exposure time of 20 ns in a time-resolved way. The measurement wavelength resolution and the integration time were adjusted to 0.01 nm and 50 ms, respectively. The width of the entrance slit was adjusted to 150 µm.

V.1.2 Electric Field Measurements (Stark Splitting Technique)

In 1919, Brose measured the electric field intensity in the cathode-fall region by observing the altered emission of the Stark effect from hydrogen discharge [62]. Several groups reported the use of polarization-dependent Stark splitting of emission of hydrogen Balmer lines to measure

the electric field strength in the plasma region in pure hydrogen and in helium with an admixture of hydrogen [63-66]. Recently, some groups have used the Stark splitting and shifting of the helium visible lines and their forbidden lines to measure the electric field strength [67-69]. In these methods, perturbation theory is used to evaluate the displacement of helium energy sublevels in an external electric field. In our method, as shown in Figure 60, the displacements of the Stark sublevels of He I 447.1 nm ($2p^3P^0$ - $4d^3D$) and its forbidden component ($2p^3P^0$ – $4f^3F^0$) is calculated in the external electric field ranging from 0 to 10 kV.

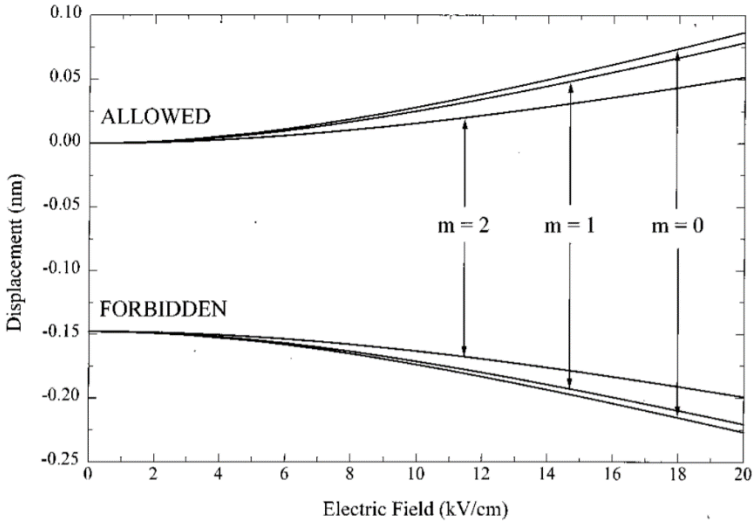

Figure 60. The sublevel displacements of $4d^3D$ and $4f^3F$ helium energy levels related to the upper levels of He I 447.1 nm its allowed and forbidden lines [67].

Since the $\pi(\Delta m = 0)$ components are stronger than $(\Delta m = \pm 1)$ and easier to detect, we will measure the wavelength separation $(\Delta\lambda_{Allowed-Forbidden})$ of π components of allowed and forbidden line $(m_{upper} = 0 \rightarrow m_{lower} = 0)$. Its relationship with the external electric field strength is shown in Figure 61.

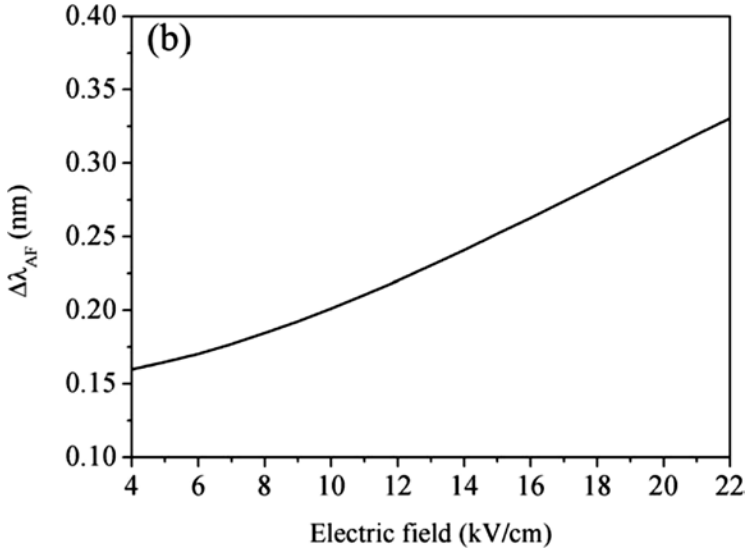

Figure 61. The relationship between the electric field strength and the wavelength separation of π component of helium visible line He I 447.1 nm from $m_{upper} = 0 \rightarrow m_{lower} = 0$ as $\Delta\lambda_{Allowed-Forbidden}$ [68].

The equivalent third-degree polynomial of Figure 61 is as

$$\Delta\lambda_{Allowed-Forbidden} = -1.6 \times 10^{-5}E^3 + 5.95 \times 10^{-4}E^2 + 2.5 \times 10^{-4}E + 0.15 \qquad (27)$$

Where $\Delta\lambda_{Allowed-Forbidden}$ is in nm and E is the external electric field strength in kV/cm.

To measure the wavelength separation of π component, we used the ICCD camera mounted on the spectrometer and put a high-contrast plastic linear polarizer with its axis parallel to the electric field. More than 10^6 photos were integrated per wavelength over time to acquire an adequate brightness for analysis. We recorded He 447.1 nm line profile emitted from the diffuse plasma. The grating of the spectrometer was fixed at 3600 grooves/mm with the entrance slit width of 300 μm. The exposure time of the ICCD camera was set to 20 ns with 100% gain value and 100 ms decay time. We set the wavelength on the spectrometer from 446.8 nm to 447.36 nm with a resolution of 0.02 nm.

Figure 62 shows the schematics of the electric field measurement setup by Stark splitting method. Since the APPJ plasma plume also emits He 447.1 nm, we put an opaque dielectric sheet between the APPJ and the chamber wall to block the plasma jet emission.

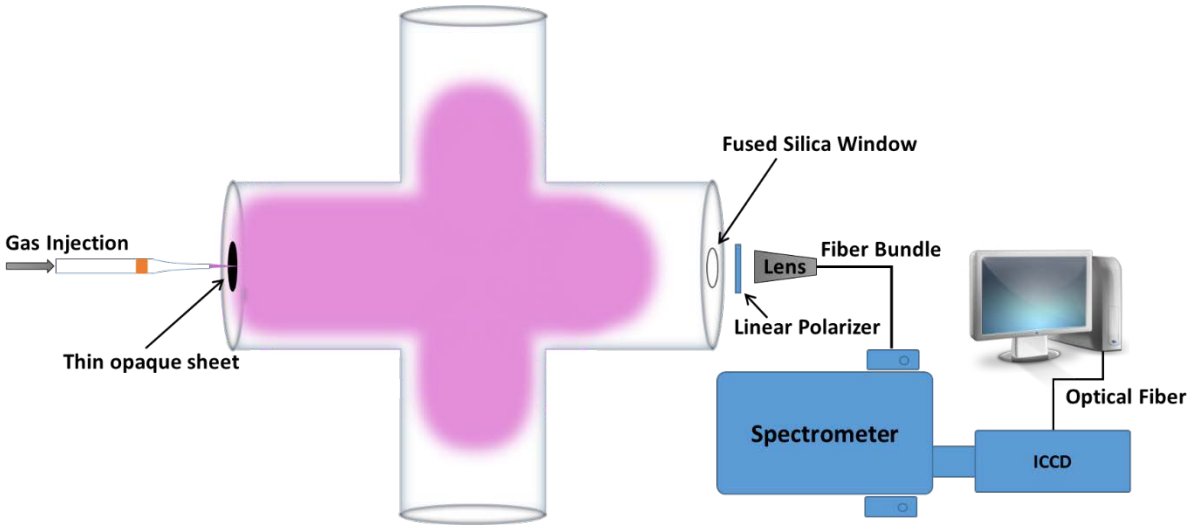

Figure 62. The schematic of the experimental setup for the electric field measurement by Stark splitting technique.

V.1.3 Fast Imaging

We also used the ICCD camera to measure the velocity and the brightness of the plasma propagation in order to study the propagation phases in both APPJ plasma plume and the transient diffuse plasma inside the low-pressure chamber. Figure 63 shows the schematics of the two experimental setups. The distance between the ICCD lens and the plasma plume was fixed at 30 cm. The distance for the chamber was fixed at 20 cm. Front view and side view imaging were taken and used depending on the aim of the image processing that will be discussed in the results section.

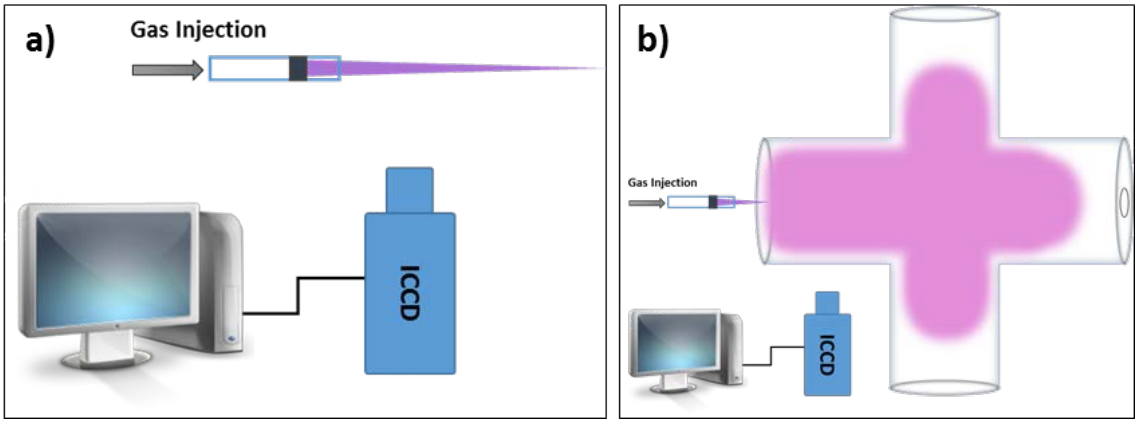

Figure 63. Schematics of the use of the ICCD camera to measure the brightness, velocity, and the propagation phases of a) the APPJ and b) the transient diffuse plasma. For the fast imaging of the diffuse plasma, side view and front view orientations were used to measure the velocity and the brightness of the plasma propagation vs. time, respectively.

The exposure time of the ICCD camera was adjusted to 20 ns with the repetition of 256 sample per recording. The delay time was set to 0-2000 ns and synched with the high-voltage pulse applied to the APPJ device. The phosphor decay time was fixed to 100 ms and the gain value to 80% and 100% for the APPJ and the diffuse plasma, respectively. The lens of the ICCD camera was adjusted to its best image quality and kept unchanged during the experiments.

V.2 RESULTS AND DISCUSSION

In this section, we discuss the results of the experiments that were done following the methods described in the previous section such as relative measurement of chemical species of APPJ and its interaction with a dielectric surface, as well as the reduced pressure diffuse plasma by optical emission spectroscopy. In addition, we present measurements of the electric field strength of the diffuse plasma by Stark splitting technique, velocity and brightness measurement of APPJ and the diffuse plasma by fast imaging technique. All of the emission-related experiments were done in a darkroom and at ambient temperature. To reduce the impact of ambient air perturbations that could disturb the measurements, we began the measurements after a few minutes of stillness inside the darkroom.

V.2.1 Single-Electrode Plasma Jet

Fast Imaging

The early formation stage of two plasma bullets in the APPJ by means of head-on ICCD pictures (see Figure 64) shows that at the initiation times of 220 ns and 920 ns, the plasma bullets are indeed a ring shape. The ring shape structure of the plasma bullets affirms that the formation process begins with a surface discharge in the vicinity of the jet tube where the electric field strength is at its highest.

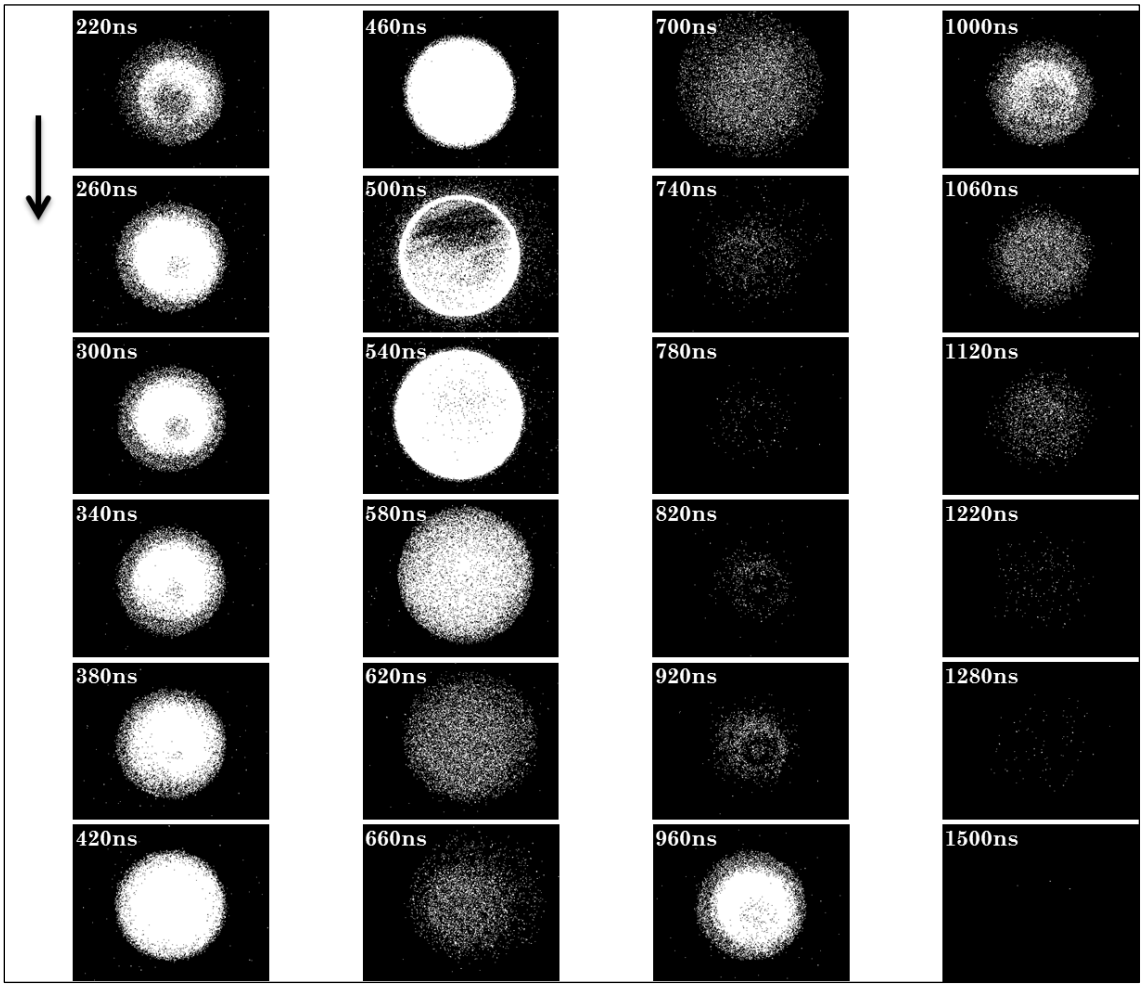

Figure 64. Head-on photography of the plasma plume along the jet tube showing the ring-shape plasma bullet with a lower brightness in the middle of the volumetric discharge at 220 ns and 920 ns (Applied voltage: 7 kV, pulse width: 700 ns, repetition rate: 7 kHz, He flow rate: 7 slm).

The side view pictures of the plasma bullets traveling along the jet tube is shown in Figure 65. The distance of the ICCD lens from the APPJ was fixed at 20 cm.

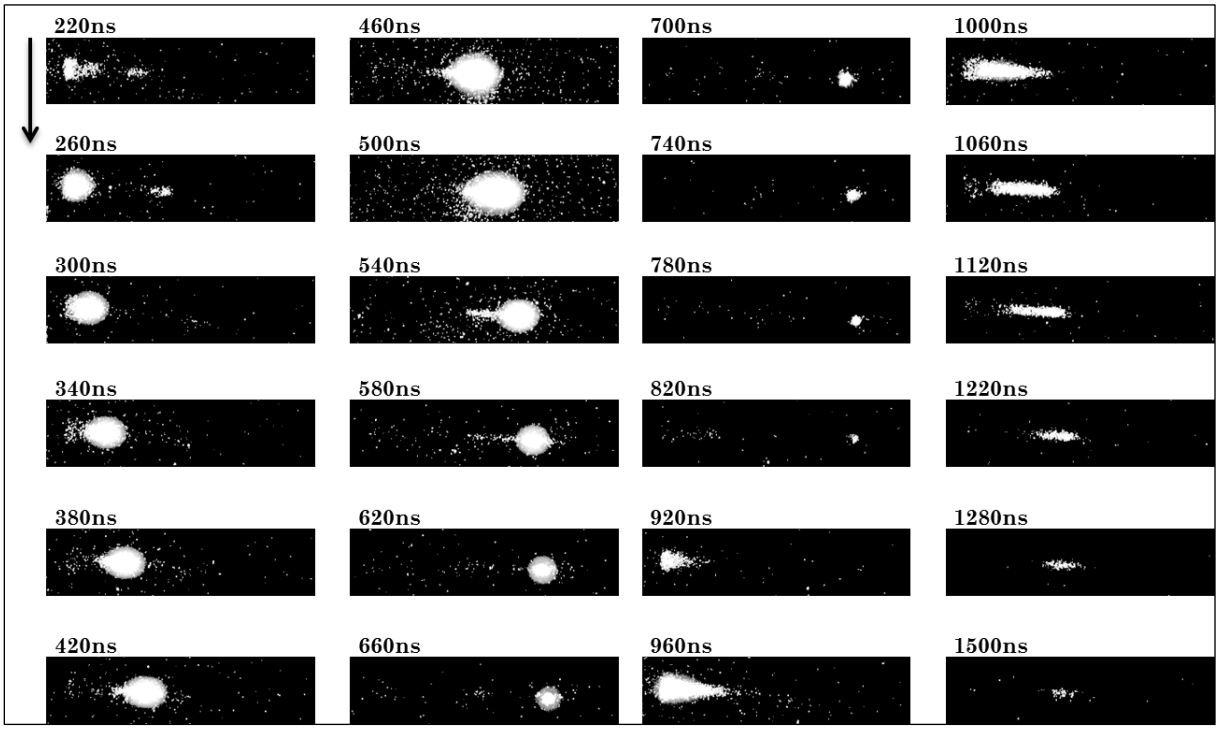

Figure 65. The side view pictures of the plasma bullets travelling along the jet. The APPJ tube exit is located on the left side of the pictures. (Applied voltage: 7 kV, pulse width: 700 ns, repetition rate: 7 kHz, He flow rate: 7 slm).

The velocity of the plasma bullet can be calculated by the displacement of the plasma bullet brightness peak over time by image processing. In Figure 66, an example of the plasma bullet velocity vs. time is shown with a peak value while traveling through the ambient air and in the helium gas channel. The velocity dramatically increases at the time of exiting the APPJ tube and emerging into the air. The reason is increasing the ionization ratio of the plasma bullet due to the increment of the air molecules such as nitrogen, oxygen, and water vapor molecules.

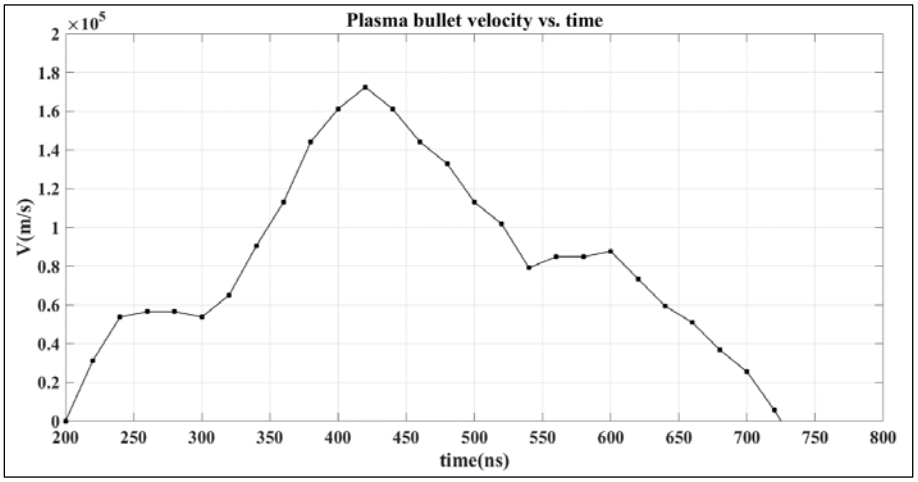

Figure 66. Velocity of the plasma bullet as function of time (Applied voltage: 7 kV, pulse width: 700 ns, repetition rate: 7 kHz, He flow rate: 7 slm).

The evolution process of first plasma discharge in the APPJ is shown in Figure 67. It was constructed using Matlab image processing of the ICCD pictures. Each graph in the figure represents a picture taken every 20 ns from 0 ns to 1000 ns. The starting point was at 220 ns and it lasted until 820 ns. The peak with the highest brightness intensity happened at 420 ns that is 20 ns after the time of exiting of the plasma bullet from the jet tube into the air through the helium gas channel.

Figure 68 shows the view from the back side of Figure 67. It was observed using images processing of the plasma bullet that the plasma bullet in the single-electrode APPJ is split into two separate parts at the time of exiting the tube. The two parts are very close to each other during the propagation process and their decay rate is similar.

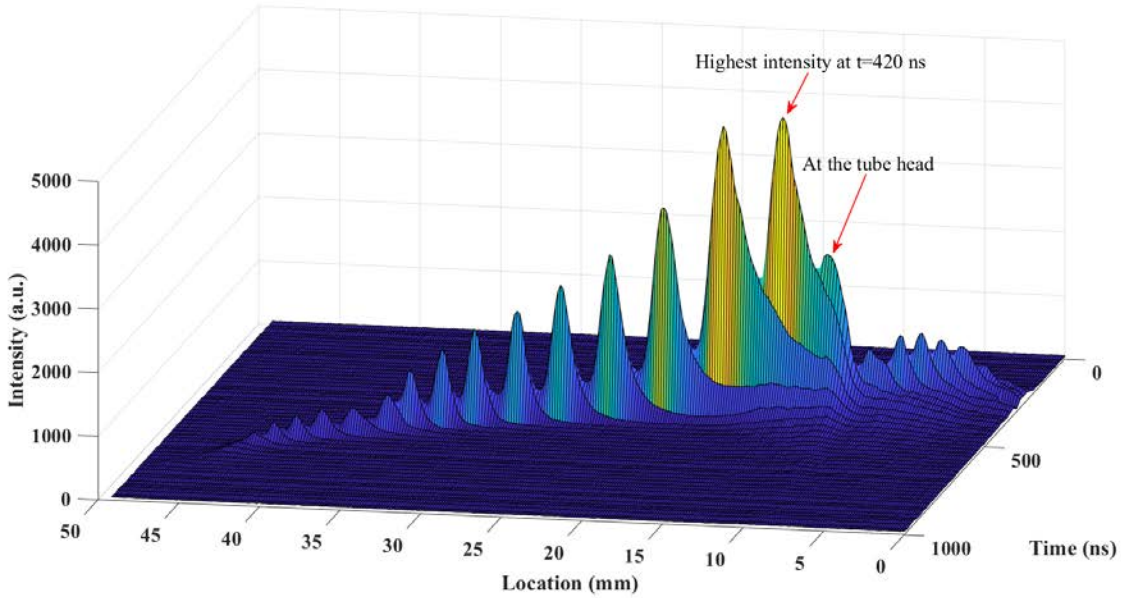

Figure 67. The evolution process of first plasma discharge in the APPJ plasma plume vs. time and location by image processing of the ICCD pictures (Applied voltage: 7 kV, pulse width: 1000 ns, repetition rate: 7 kHz, He flow rate: 7 slm).

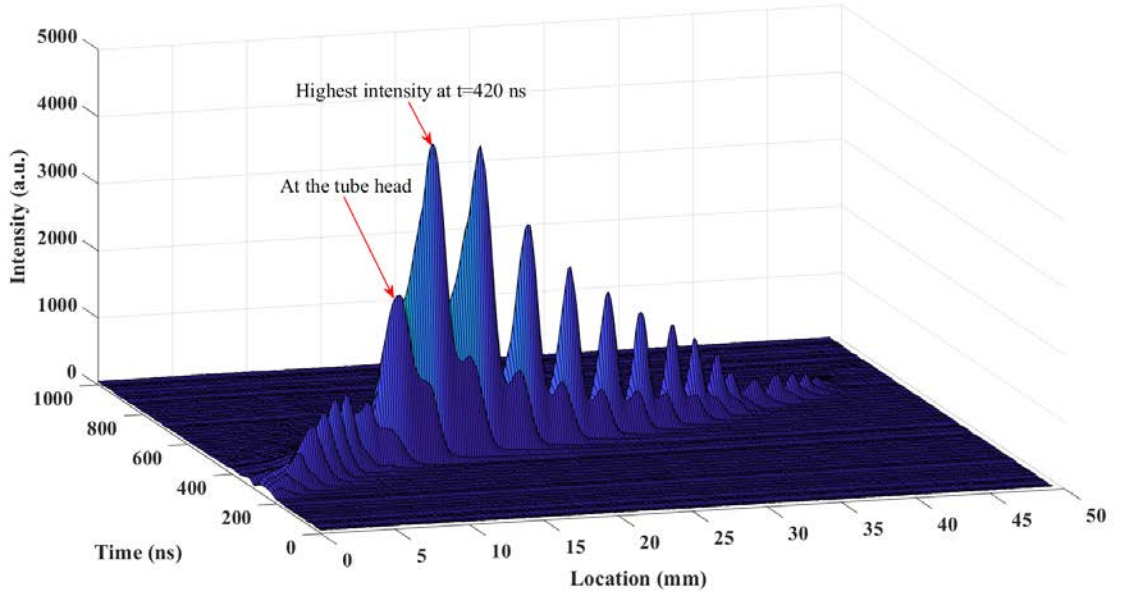

Figure 68. The evolution process of first plasma discharge in the APPJ plasma plume vs. time and location by image processing of the ICCD pictures (Applied voltage: 7 kV, pulse width: 1000 ns, repetition rate: 7 kHz, He flow rate: 7 slm).

Figure 69 shows the evolution of the second discharge vs. time. As it is clear there are two peak values at 1240 ns and 1300 ns. The location of the peak values is at 6 mm and 18 mm from the tip of the electrode, one inside the jet tube and another one outside of it. The locations are the same as the locations that were discussed in the previous chapter regarding the maximum positive net charge along the plasma channel measured by the D-dot probe. Figure 69 indicates that the recombination of released electrons along the gas channel during the second discharge is more likely to happen at the locations with higher values of positive net charge. The relative intensity ratio at those locations also has a close similarity to the measured relative positive net charge by the D-dot probe.

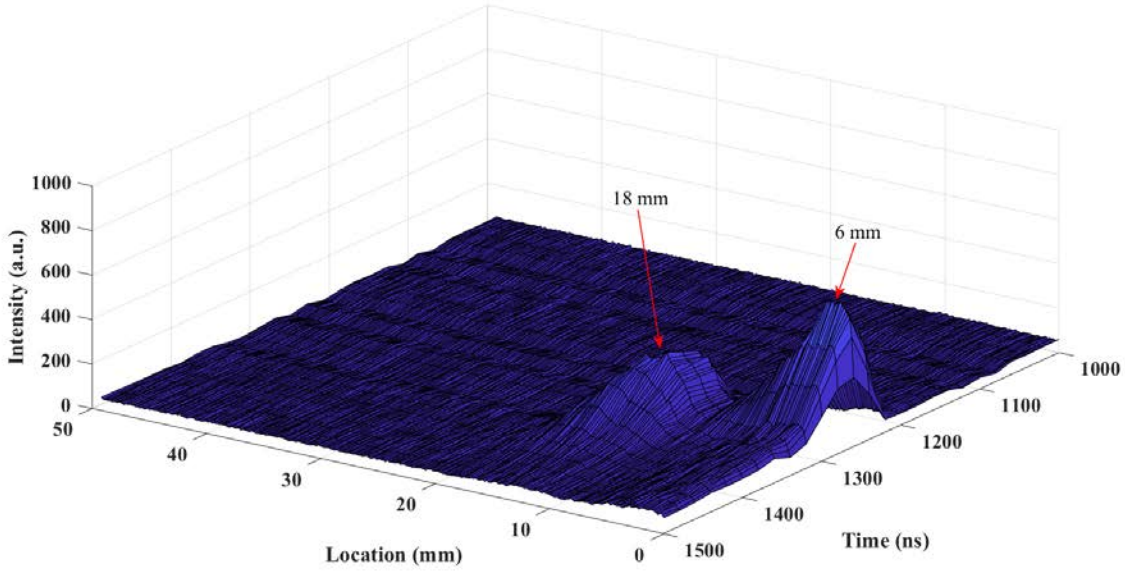

Figure 69. The evolution process of second plasma discharge in the APPJ plasma plume vs. time and location by image processing of the ICCD pictures (Applied voltage: 7 kV, pulse width: 1000 ns, repetition rate: 7 kHz, He flow rate: 7 slm).

Optical Emission Spectroscopy

An example of low-resolution visible emission spectra of APPJ observed in the 500-800 nm is represented in Figure 70. Since the high-intensity second order of UV in the visible region prevents recording a good quality intensity peaks in the visible region, we blocked it by putting a UV filter in the beam path towards the spectrometer fiber optic bundle. Most of the peaks in the visible spectra profile come from the helium metastable transitions such as 501.5 nm ($3^1P \rightarrow 2^1S$), 587.5 nm ($3^3D \rightarrow 2^3P$), 667.8 nm ($3^1D \rightarrow 2^1P$), and 706.5 nm ($3^3S \rightarrow 2^3P$). The helium excited states can be populated either by electron impact excitation of helium ground state and helium metastable state or by several dissociative recombination mechanisms. A weak signal of atomic oxygen O ($3^5S \rightarrow 3^5P$) at 777 nm can also be found.

The UV emission spectra of APPJ plasma plume in the wavelength range of 230-500 nm is shown in Figure 71. The same experimental setup was used to record the UV spectra of the plasma jet except for the UV filter that was not used in this case. Most of the signals in the UV spectra profile represent the second positive series of molecular nitrogen 0-0 bands including 337 nm and 380.4 nm. Very weak OH (A-X) transition can also be found in the UV spectra from 306 nm to 309.2 nm.

There are many other short-lived and long-lived generated species in the plume of the APPJ plasma which do not radiate during their decay time or their radiation is too weak to be detectable by means of OES method such as O_3, NO, NO_2, etc.

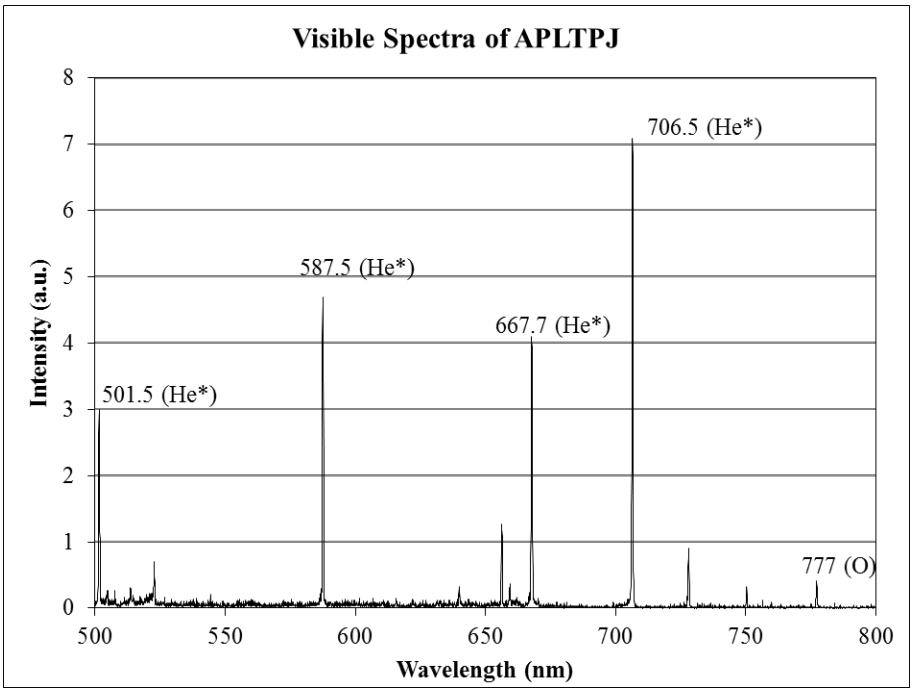

Figure 70. An example of low-resolution visible emission spectra of APPJ observed in the 500-800 nm after filtering the second order of UV in the visible region (Applied voltage: 7 kV, pulse width: 700 ns, repetition rate: 7 kHz, He flow rate: 7 slm).

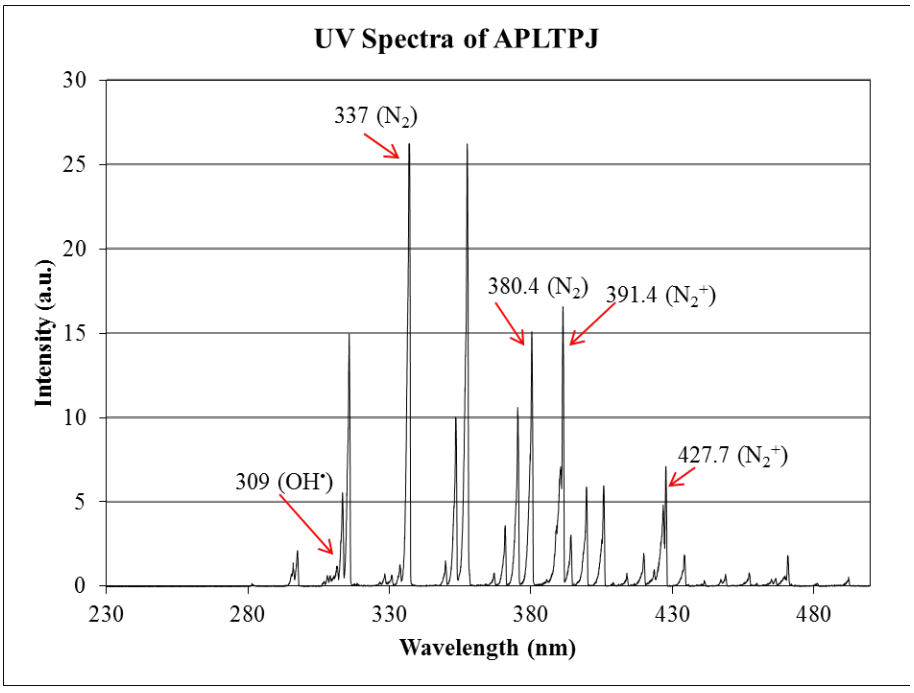

Figure 71. An example of low-resolution UV emission spectra of APPJ observed in the 230-500 nm (Applied voltage: 7 kV, pulse width: 700 ns, repetition rate: 7 kHz, He flow rate: 7 slm).

Integrating the spectra profile intensity gives us an exponential attenuation as a function of distance from the APPJ. We observed the same results by measuring the brightness of the plasma plume by means of ICCD camera. Figure 72 shows the results as a relative intensity vs distance from the tip of the plasma jet. The plasma bullet becomes smaller in volume while traveling through the gas channel and going farther away from the jet. The extracted exponential equation, $\frac{I}{I_0} = e^{\frac{x(mm)}{10}}$, shows a uniform attenuation with the total attenuation coefficient, α_{tot}, of 10 mm along the ionization channel.

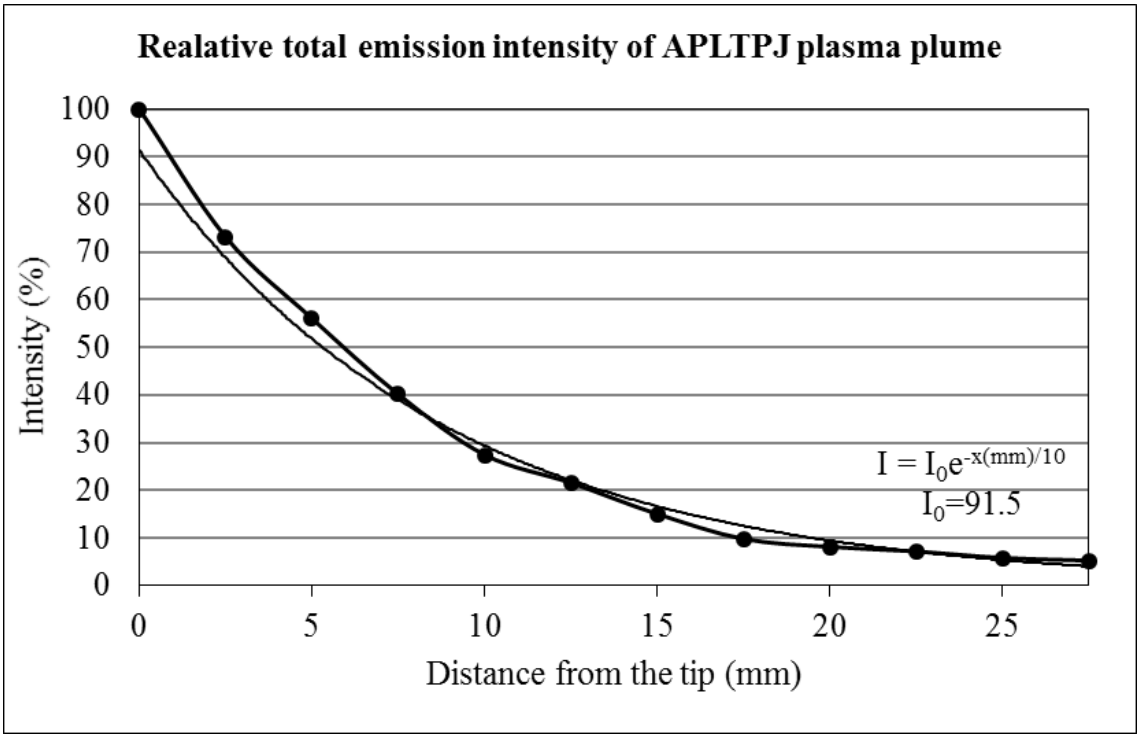

Figure 72. Relative space-resolved total emission of the APPJ plasma plume intensity integrated over the 230-800 nm wavelength range (Applied voltage: 7 kV, pulse width: 700 ns, repetition rate: 7 kHz, He flow rate: 7 slm).

Space-resolved OES results

In order to study the radiative species along the plasma plume, we measured the relative intensity of He^*, atomic oxygen, N_2^+, N_2, and $OH^\bullet$ by space-resolved OES. We used the mounted PMT on the spectrometer to record the data. As it was illustrated in Figure 57, the light was collected by two lenses through an aperture at 12 different distances from the APPJ electrode from 3 mm to 36 mm. Since the electrode blocked a portion of emitted light at the tip of the electrode at 0 mm, we excluded it from the results.

The relative intensity of metastable states of helium at 501.6 nm, 667.8 nm, and 706.55 nm vs. the distance from the tip of the APPJ electrode along the plasma plume is shown in Figure 73. The emission of He^* ($3^3S \rightarrow 2^3P$) at 706.5 nm drops faster than 667.8 nm ($3^1D \rightarrow 2^1P$) and 501.6 nm ($3^1P \rightarrow 2^1S$) that is corresponding to their probability of emission, Einstein coefficient. The results show that the helium metastable were formed inside the tube and they radiate with an exponential drop along the plasma plume.

Figure 74 shows the relative intensity of atomic oxygen at 777.25 nm ($3^5P \rightarrow 3^5S$) vs. the distance from the tip of the APPJ electrode. At 9 mm, the relative density of atomic oxygen is at its highest level. At the tip of the APPJ, air molecules (O_2, N_2, and a small amount of H_2O_2 molecules) start to diffuse into the helium gas channel and provide a different condition than inside the plasma jet region.

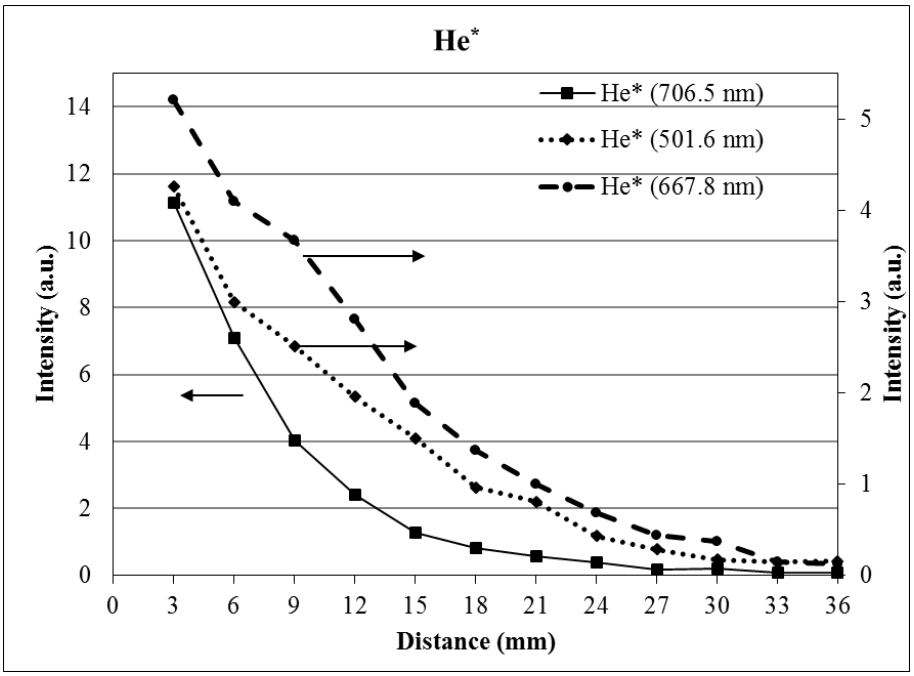

Figure 73. Relative intensity of metastable states of helium at 501.6 nm, 667.8 nm, and 706.55 nm vs. distance from the tip of the APPJ electrode along the plasma plume (Applied voltage: 7 kV, pulse width: 700 ns, repetition rate: 7 kHz, He flow rate: 7 slm).

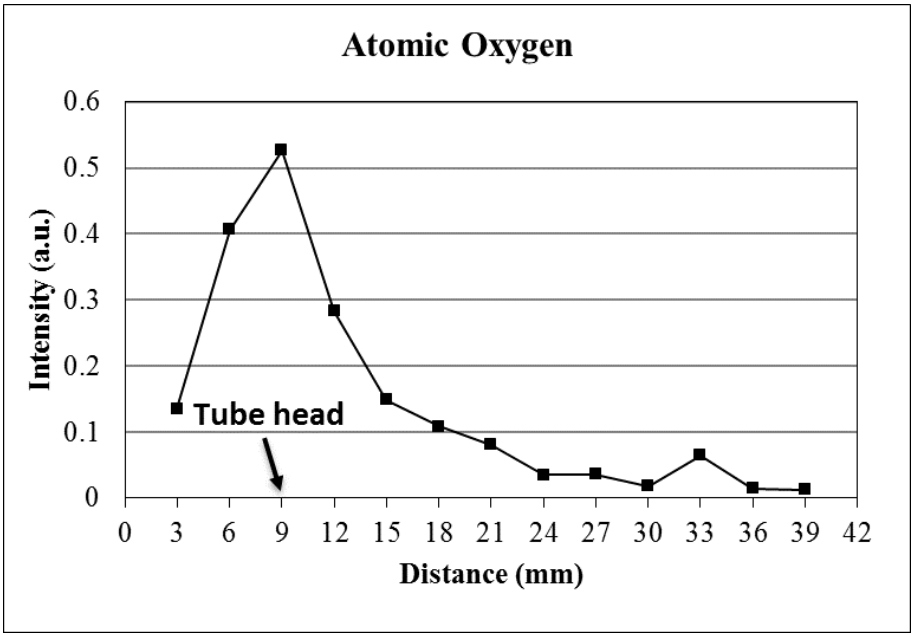

Figure 74. Relative density of atomic oxygen at 777.25 nm vs. distance from the tip of the APPJ electrode along the plasma plume (Applied voltage: 7 kV, pulse width: 700 ns, repetition rate: 7 kHz, He flow rate: 7 slm).

Figure 75 shows the evolution of N_2^+ along the plasma plume by observing the relative intensity of N_2^+ at 427.8 nm and 391.2 nm ($B^2\Sigma_u^+(v=0) - X^2\Sigma_g^+ (v=0)$). The evolution of N_2 along the plasma plume is presented in Figure 76 by observing the relative intensity of N_2 at 337.1 nm, 375.4 nm, and 380.3 nm. The evolution pattern of both N_2^+ and N_2 are similar. Both N_2^+ and N_2 densities reach their maximum level at the tip of the APPJ as atomic oxygen does. N_2^+ decay ratio is higher over distance with respect to N_2 decay ratio.

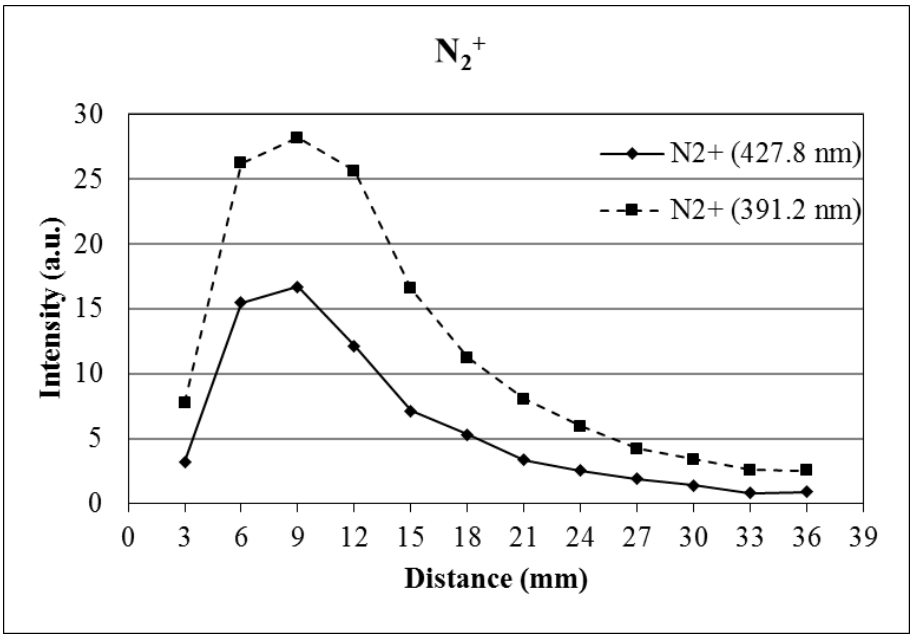

Figure 75. Relative density of N_2^+ at 427.8 and 391.2 nm ($B^2\Sigma_u^+(v=0) - X^2\Sigma_g^+ (v=0)$) vs. distance from the tip of the APPJ electrode along the plasma plume (Applied voltage: 7 kV, pulse width: 700 ns, repetition rate: 7 kHz, He flow rate: 7 slm).

We also observed the space-resolved density of hydroxyl radical, $OH^{\bullet}$ (A-X), at 309 nm vs. distance that is shown in Figure 77.. The maximum density starts from the inside of the APPJ due to the water vapor impurities from the plasma jet feeding gas.

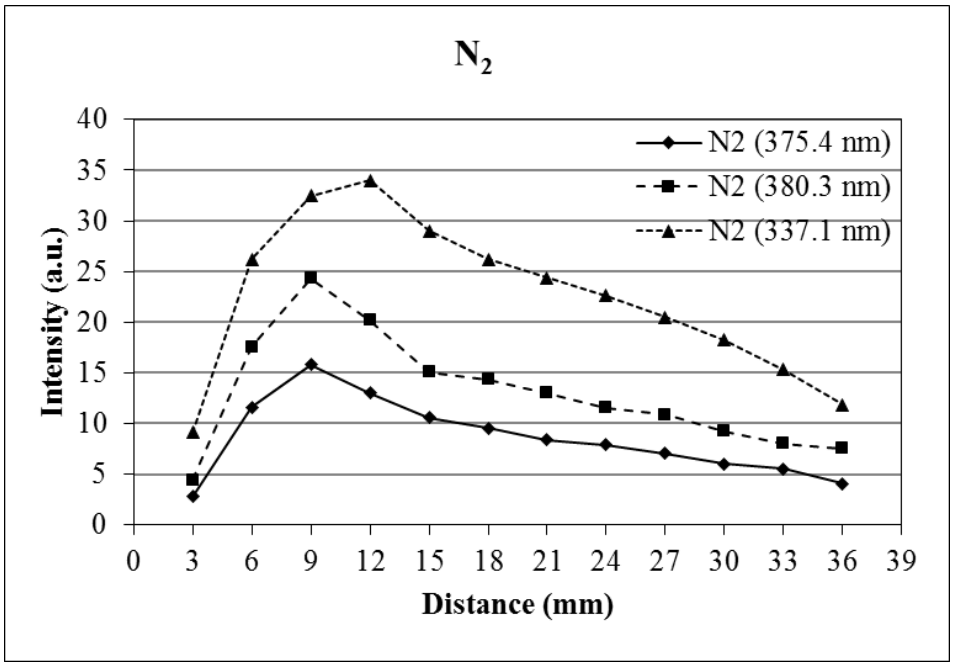

Figure 76. Relative density of N_2 at 337.1 nm, 375.4 nm, and 380.3 nm vs. distance from the tip of the APPJ electrode along the plasma plume (Applied voltage: 7 kV, pulse width: 700 ns, repetition rate: 7 kHz, He flow rate: 7 slm).

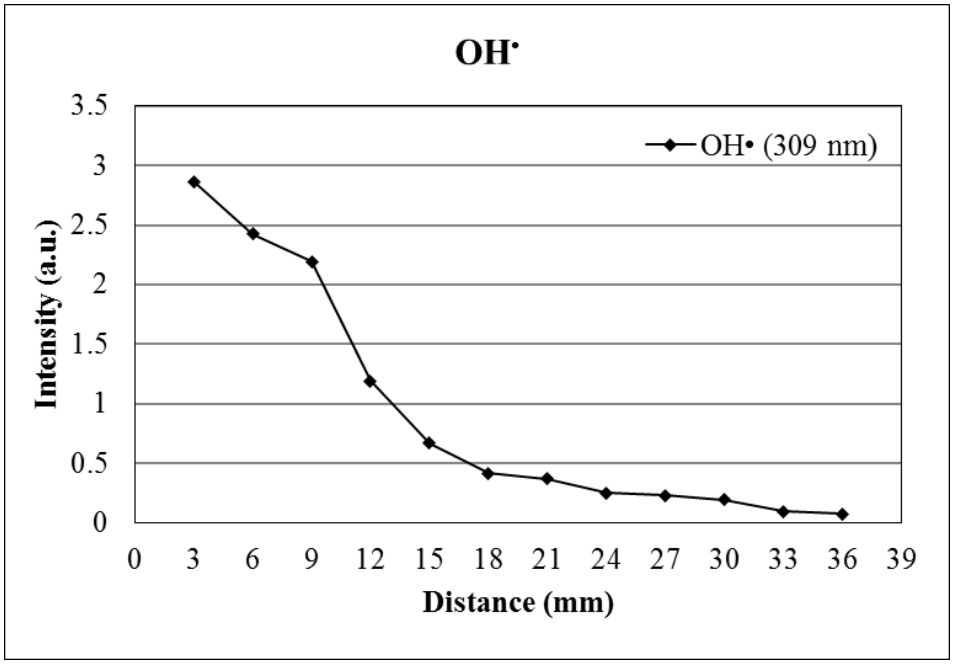

Figure 77. Relative density of $OH^{\bullet}$ (A-X) radical at 309 nm vs. distance from the tip of the APPJ electrode along the plasma plume (Applied voltage: 7 kV, pulse width: 700 ns, repetition rate: 7 kHz, He flow rate: 7 slm).

Time-resolved OES results

Time-resolved OES results provide a complimentary information about the evolution of the chemical species along the plasma plume over time. The lenses were placed head-on to the plasma plume and the light was collected by the ICCD mounted on the spectrometer as it was illustrated in Figure 58. The applied parameters were fixed as applied voltage: 7 kV, pulse width: 700 ns, repetition rate: 7 kHz, He flow rate: 7 slm for all experiments. The first discharge started at 220 ns and exited the APPJ tube at 460 ns in all measurements. The second discharge occurred at 960 ns.

The result of the time-resolved relative intensity of helium metastable state at 706.5 nm vs. time is shown in Figure 78. We see a sudden increment of He^* at the beginning when the plasma bullet forms. Since the intensity of He^* emission is roughly constant until the plasma bullet exits the tube, it shows that the H^* decay rate is equal to its production rate during that time. A sudden drop of about 85% at the tube exit shows that the interaction of He^* with air molecules (N_2, O_2, and H_2O_2 molecules) plays the most important role in the production of chemical species at the tube exit via the Penning ionization process. The two following equations show the Penning ionization process of atomic species and the Penning dissociative process of diatomic molecules, respectively [70].

$$He^* + X \rightarrow He + X^+ + e \tag{28}$$

$$He^* + YZ \rightarrow He + Y + Z \tag{29}$$

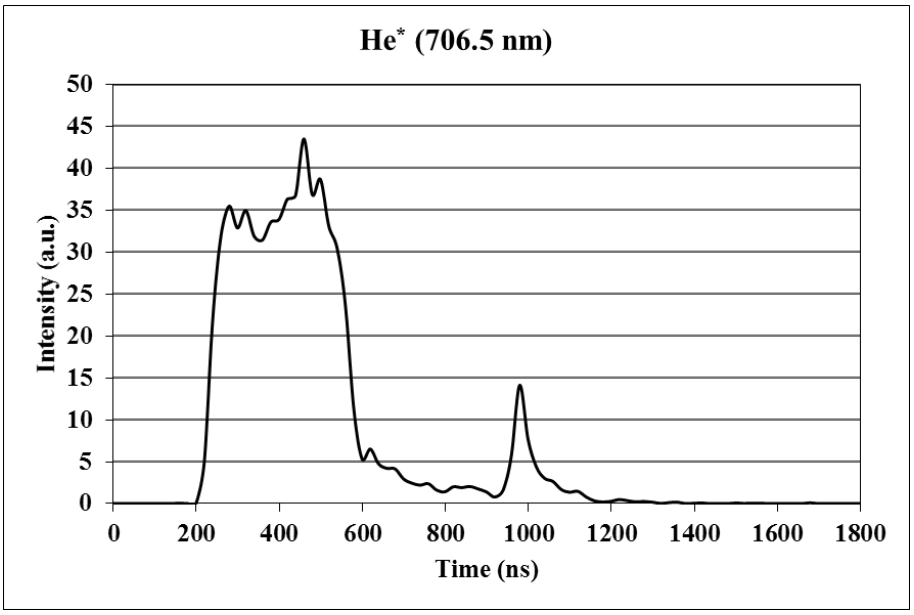

Figure 78. Time-resolved relative intensity of helium metastable state at 706.5 nm. The plasma bullet was generated at 220 ns and exits the APPJ tube at 460 ns. The second discharge occurred at 920 ns. (Applied voltage: 7 kV, pulse width: 700 ns, repetition rate: 7 kHz, He flow rate: 7 slm).

Figure 79 shows the result of the time-resolved relative intensity of atomic oxygen at 777.25 nm. The constant intensity of O $(3^5P \rightarrow 3^5S)$ inside the tube shows that the source of the oxygen molecule inside the tube is from the impurities of the feeding gas. At the exit tube, there is a dramatic increase in the production of atomic oxygen and it drops as the plasma bullet moves forward through the air. The second discharge has no particular impact on the production of atomic oxygen in the APPJ plasma.

Figure 80 shows the time-resolved relative intensity of hydroxyl radical emission at 309 nm. The production of hydroxyl radicals over time has a similar pattern to the generation of atomic oxygen. The production and decay rate of both species (hydroxyl radical and atomic oxygen) are in accordance with the production and decay rate of helium excited metastable 2^3S state over time in the APPJ plasma plume.

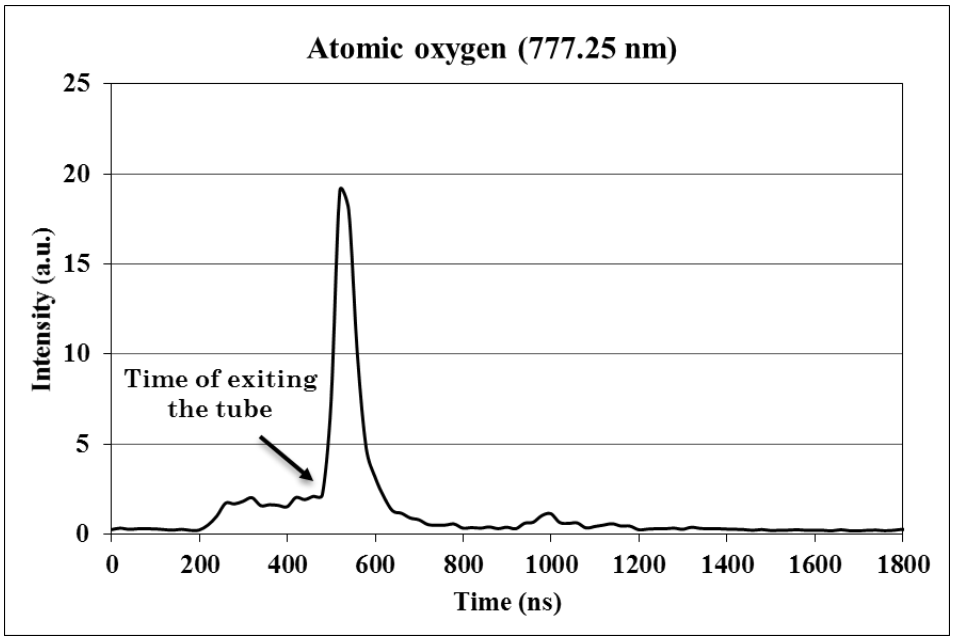

Figure 79. Time-resolved relative intensity of atomic oxygen at 777.25 nm. The first plasma bullet was generated at 220 ns and exits the APPJ tube at 460 ns. The second discharge occurred at 920 ns. (Applied voltage: 7 kV, pulse width: 700 ns, repetition rate: 7 kHz, He flow rate: 7 slm).

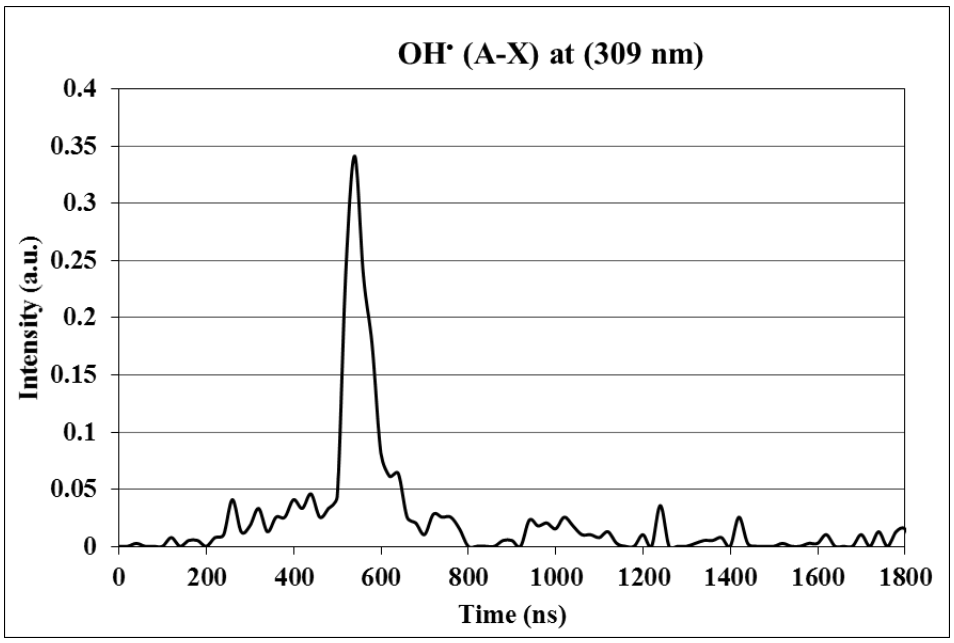

Figure 80. Time-resolved relative intensity of hydroxyl radical emission at 309 nm. The first plasma bullet was generated at 220 ns and exits the APPJ tube at 460 ns. The second discharge occurred at 920 ns. (Applied voltage: 7 kV, pulse width: 700 ns, repetition rate: 7 kHz, He flow rate: 7 slm).

V.2.2 Single-Electrode Plasma Jet and Dielectric Obstacle

The image of a plasma plume perpendicular to a dielectric surface in Figure 81 shows that the plume spreads homogeneously and symmetrically over the surface with a pink color as a result of generated helium metastable atoms until air molecules diffuse into the plasma zone and severely quench the metastable states of helium. Increasing the nitrogen and oxygen number density in the bulk of the plasma, the color of plasma becomes more bluish and it forms several discrete surface discharges. The mechanism of surface charge spread on the dielectric surface is thought to be similar to a plasma jet.

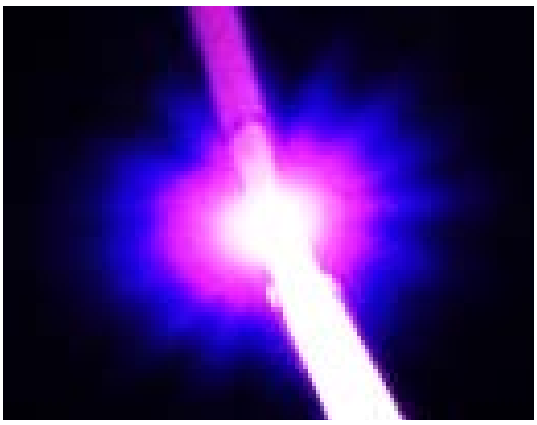

Figure 81. Image of plasma plume spreading over a Plexiglass surface with a thickness of 17 mm (Applied voltage: 7 kV, pulse width: 1000 ns, repetition rate: 7 kHz, He flow rate: 7 slm, Distance between the APPJ tube exit and the dielectric surface: 6 mm).

As the successive images of bullet-dielectric surface incidence are shown in Figure 82.a, it was observed that the plasma bullet propagation on the surface of a dielectric as a surface discharge is homogeneously distributed while a sufficient amount of helium is accessible on the dielectric surface. The images of plasma bullet-dielectric surface incidence in Figure 82.b shows the second plasma bullet associated with the electron relaxation process in which the accumulated electrons inside the APPJ tube spread over the formerly developed ionization channel.

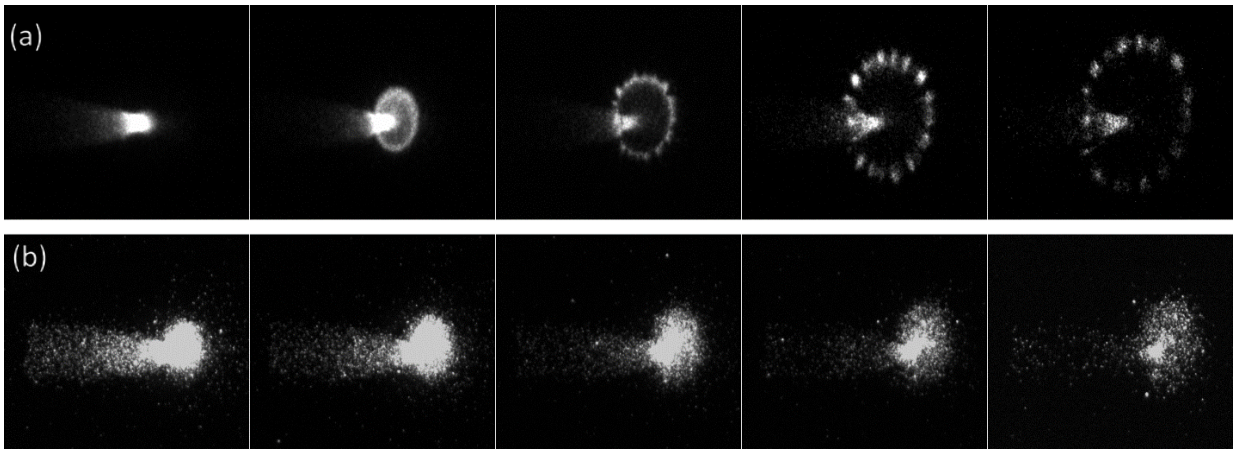

Figure 82. Images of bullet-dielectric surface incidence. Images were captured successively every 20 ns. A) Propagation of the first plasma bullet and b) the second plasma bullet on the surface of a Plexiglass located at the distance of 6 mm from the tip of the APPJ (Applied voltage: 7 kV, pulse width: 1000 ns, repetition rate: 7 kHz, He flow rate: 7 slm).

Surface discharge propagation speed in Figure 83 indicates that the velocity of surface discharge spreading on the surface of the dielectric decreases over time. It was also observed that the plasma bullet velocity in the vicinity of the dielectric surface is several times higher than the maximum velocity of the plasma bullet during its propagation phase which was 60 km/s as reported by Laroussi and co-workers [27].

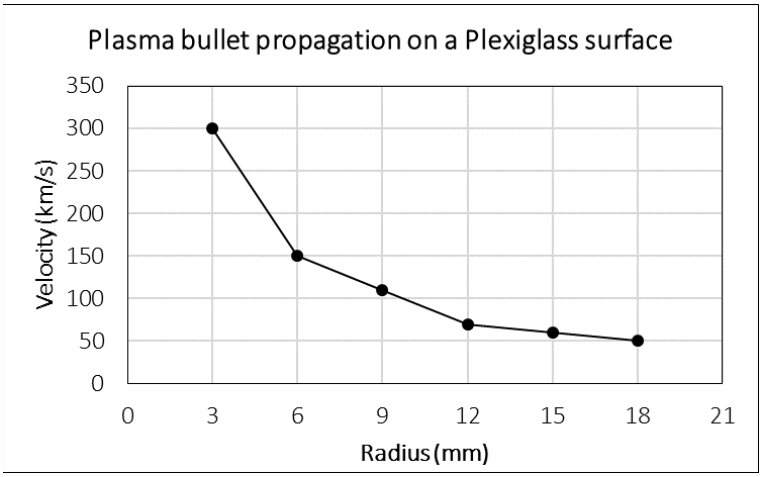

Figure 83. Bullet propagation velocity on the surface of a dielectric. Measurement was done by dividing the bullet propagating radius by the time of the expansion (Applied voltage: 7 kV, pulse width: 1000 ns, repetition rate: 7 kHz, He flow rate: 7 slm).

V.2.3 Transient Diffuse Plasma at Reduced Pressure

Fast Imaging

Figure 84 shows a typical example of fast imaging of the FIW inside the low-pressure chamber generated by the APPJ plasma plume that is placed perpendicular to the cylindrical Pyrex shell of the chamber with a distance of 15 mm from the tube exit. The plasma bullet exits the APPJ tube and impinges on the chamber wall at 600 ns and initiates the diffuse plasma inside the chamber. The ICCD camera recorded the side-view pictures of the FIW propagation phases. Since there is no electrode inside the chamber, the electrons get accelerated directly proportional to the electric field intensity. A preliminary ionization process is expected before the plasma bullet onset due to the external electric field strength when the APPJ device is running with no plasma at the very beginning of the rise time of the high-voltage pulse. The evolution of diffuse plasma inside the chamber shows that the approaching plasma bullet makes a transition inside the chamber from a low-density ionization process to a FIW that lasts for several hundreds of nanoseconds. The speed of the FIW was about 10^6 m/s.

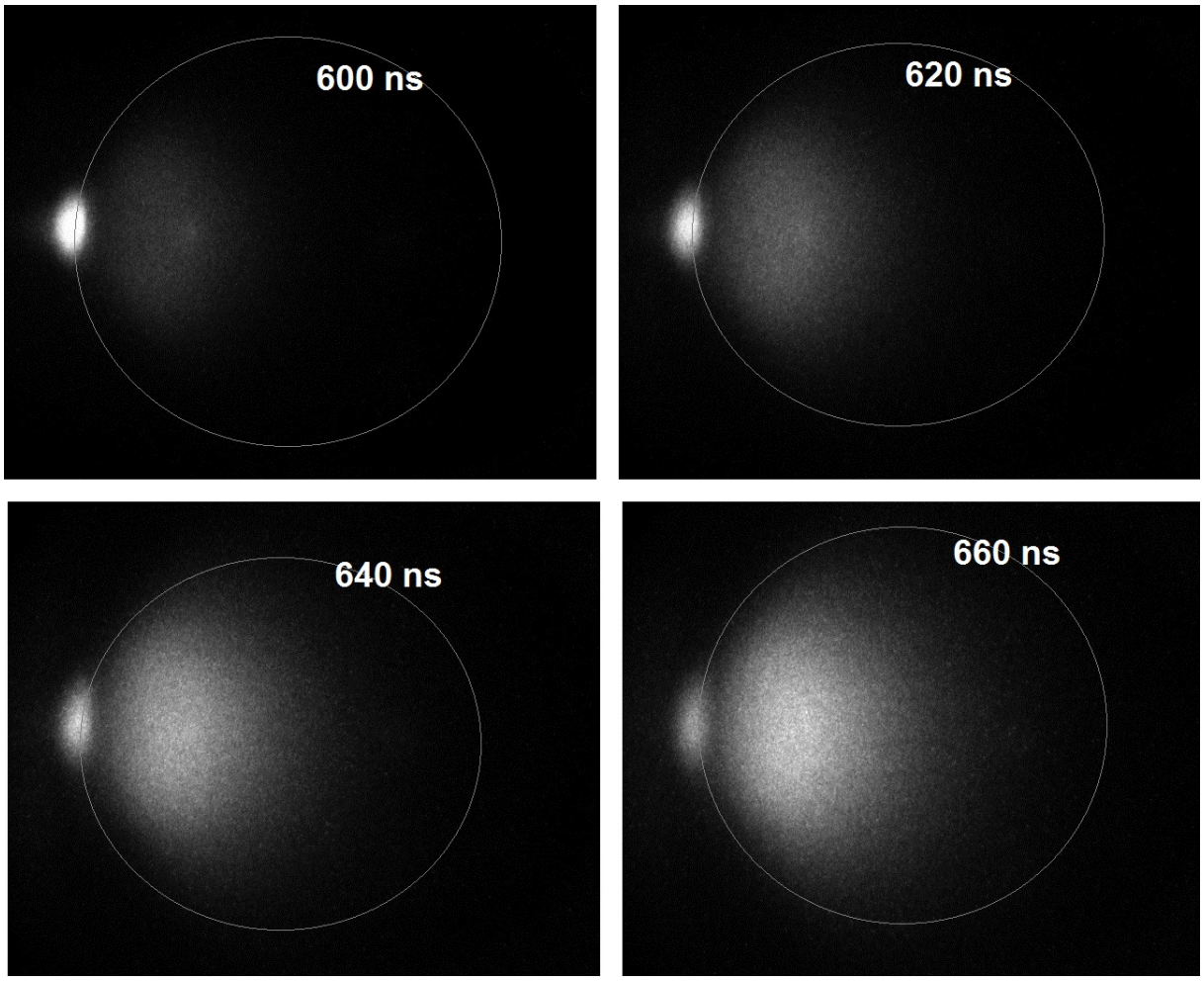

Figure 84. The evolution of diffuse plasma inside the chamber. The bright spot on the left is the plasma bullet that was impinged on the glass surface of the low-pressure chamber wall (Applied voltage: 7 kV, Pulse width: 1000 ns, Repetition rate: 7 kHz, APPJ He flow rate: 7 slm, Pressure: 0.5 Torr, Distance between plasma jet exit tube and the chamber: 6 mm).

As shown in Figure 85, increasing the pressure from 200 mTorr up to 3 Torr leads to the formation of a corona discharge or sub-glow discharge in the air diffuse plasma. This transition happens when a collisionless or weakly collisional plasma becomes more collisional.

Figure 85. The transition of plasma from a diffuse glow discharge to corona discharge in a chamber filled with air at a) 200 mTorr with negative glow and positive column, b) at 1 Torr without the positive column, and c) at 3 Torr transitions to corona discharge (Applied voltage: 7 kV, pulse width: 1000 ns, repetition rate: 7 kHz, APPJ He flow rate: 7 slm, Distance between plasma jet exit tube and the chamber: 6 mm).

We measured the distance traveled by the FIW inside the chamber as a function of pressure in both helium diffuse plasma and air diffuse plasma. These are presented in Figure 86 and Figure 87, respectively. The results show a shrinkage in the FIW volume as pressures increases. The distance that FIW can travel is inversely proportional to the pressure. Comparing Figure 86 with Figure 87, the length of FIW in the air diffuse plasma drops dramatically as compared to the helium diffuse plasma. The reason can be due to quenching effect of highly electronegative oxygen and nitrogen molecules in the air plasma.

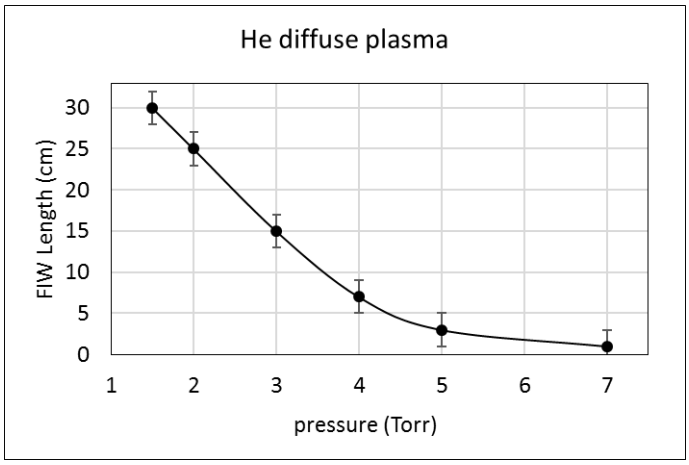

Figure 86. FIW propagation length vs. pressure in a diffuse plasma inside the chamber filled with helium (Applied voltage: 7 kV, pulse width: 1000 ns, repetition rate: 7 kHz, APPJ He flow rate: 7 slm, Distance between plasma jet exit tube and the chamber: 6 mm).

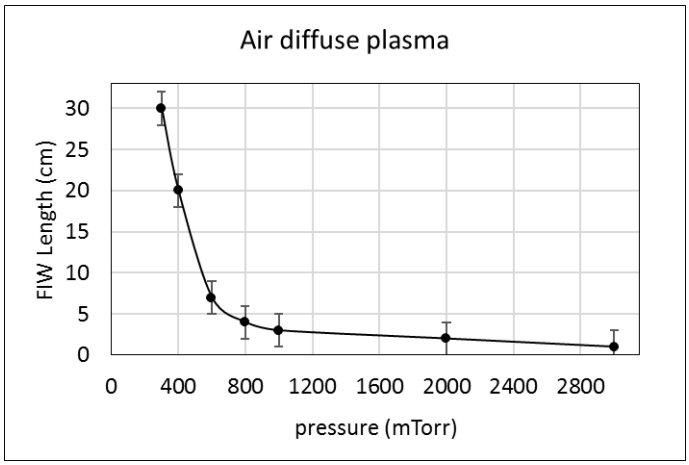

Figure 87. FIW propagation length vs. pressure in a diffuse plasma inside the chamber filled with air (Applied voltage: 7 kV, pulse width: 1000 ns, repetition rate: 7 kHz, APPJ He flow rate: 7 slm, Distance between plasma jet exit tube and the chamber: 6 mm).

Optical Emission Spectroscopy (OES)

Figure 88 shows an example of a combined UV and visible spectra of the helium diffuse plasma from 300 nm to 800 nm observed by the spectrometer and PMT as the recorder. Nitrogen and oxygen impurities in the helium diffuse plasma play an important role in the radiative decays of the plasma besides the helium metastable transitions itself as it was mentioned earlier.

Most of the radiative transitions mentioned in the APPJ spectroscopy can be found in the helium diffuse plasma due to the similar admixtures. Moreover, we observed the first and the second ionization of nitrogen, N(I) and N(II) [71]. In the helium diffuse plasma, N(I) and N(II) were observed by their relatively high intensity peaks of 415.1 nm ($2s^2 2p^2(^3\mathrm{P})4\mathrm{p} \rightarrow 2s^2 2p^2(^3\mathrm{P})3s$) and 595.0 nm ($2s^2 2p 3d \rightarrow 2s^2 2p 3p$), respectively.

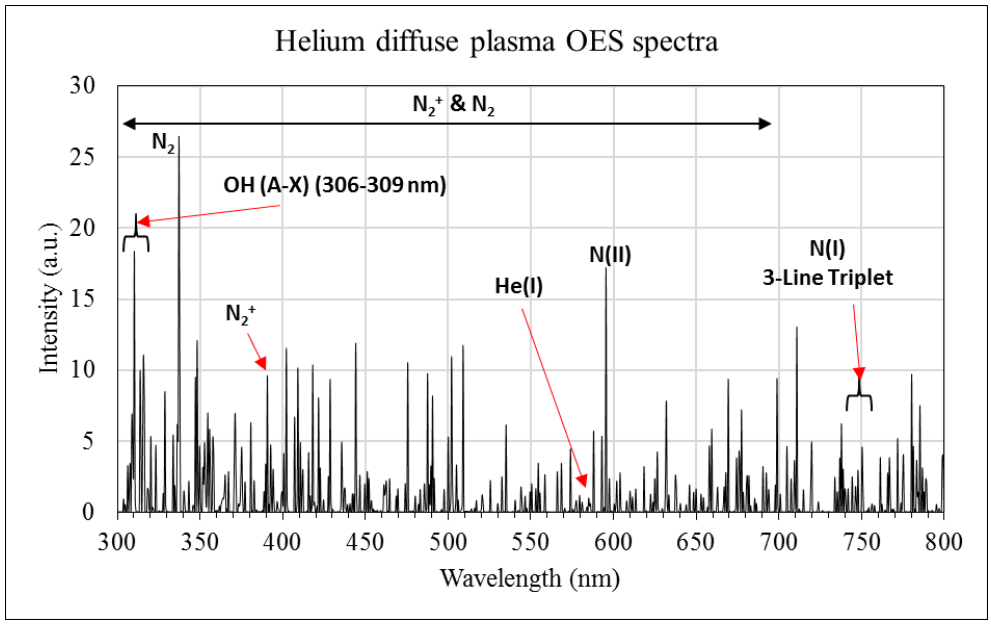

Figure 88. An example of a combined UV and visible spectra of the helium diffuse plasma at 1.5 Torr in the 300-800 nm range (Applied voltage: 7 kV, pulse width: 1000 ns, repetition rate: 7 kHz, APPJ He flow rate: 7 slm, Distance between plasma jet exit tube and the chamber: 6 mm).

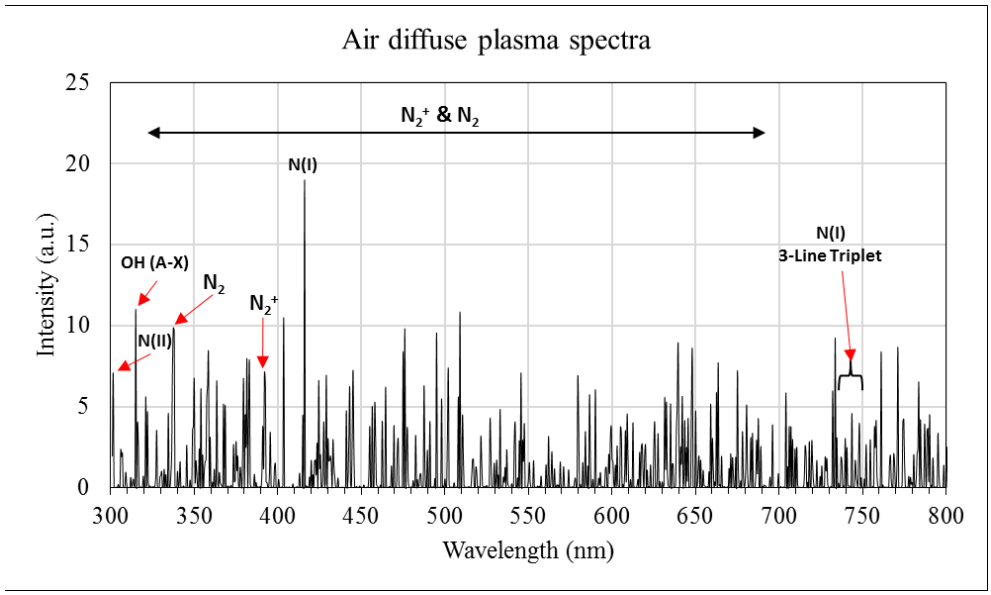

Figure 89. An example of a combined UV and visible spectra of the air diffuse plasma at 200 mTorr in the 300-800 nm range (Applied voltage: 7 kV, pulse width: 1000 ns, repetition rate: 7 kHz, APPJ He flow rate: 7 slm, Distance between plasma jet exit tube and the chamber: 6 mm).

The excited state of N_2^+ is often generated by the reaction of N_2 with helium metastable as shown below

$$He^* + N_2 \rightarrow N_2^+ + He + e^-$$

Most of the electronic transitions in the diffuse plasma are related to the nitrogen molecular bands since it is the main constituent of air either in the air diffuse plasma or in the helium diffuse plasma as an impurity. The most probable transitions are N_2 FPS, N2 SPS, and N_2^+ FNS. Table 5 is a list of some observed intense nitrogen molecular bands in a laser-induced nitrogen breakdown, their electronic transition, and wavelength in angstrom (A^o) for the major band heads with assigned vibrational quantum numbers transitioning from v' to v'' as a radiative decay [72, 73].

Excited Hydroxyl radical, OH(A), transition to its ground state, OH(X) is another emission that is observed in various He plasmas with even a very small amount of H_2O impurity. It is generated by the following reactions.

$$H_2O + He^* \rightarrow H_2O^+ + e^-$$

$$H_2O^+ + H_2O \rightarrow H_3O^+ + OH(X)$$

And OH(X) becomes excited by electron impact excitation emitting from 306 nm to 309.2 nm, consequently. OH(A) is also reported to be generated by electron impact excitation dissociation of H_2O and also dissociative recombination of H_2O^+ or H_3O^+ resulting in high rotational energy [74].

Table 5. List of some intense observed nitrogen molecular bands in a capacitive breakdown, their electronic transition, and wavelength in angstrom (A^o) for the major band heads with assigned vibrational quantum numbers ν' and ν'' [73].

Molecule	Name of the system	Observed band system	Major band heads (Å) (v', v'')
N_2^+	First negative	$B^2\Sigma_u^+ - X^2\Sigma_g^+$	2861.7 (11, 6); 3033.0 (11, 7); 3065.1 (15, 10); 3076.4 (4, 1); 3078.2 (3, 0); 3291.6 (5, 3); 3293.4 (4, 2); 3298.7 (3, 1); 3308.0 (2, 0); 3319.9 (8, 6); 3349.6 (18, 13); 3381.5 (10, 8); 3419.6 (14, 11); 3447.3 (23, 16); 3460.8 (17, 13); 3493.4 (12, 10); 3532.3 (5, 3); 3538.3 (4, 3); 3548.9 (3, 2); 3563.9 (2, 1); 3582.1 (1, 0); 3588.6 (16, 13); 3612.4 (10, 9); 3806.8 (5, 5); 3818.1 (4, 4); 3835.4 (3, 3); 3857.9 (2, 2); 3884.3 (1, 1); 3914.4 (0, 0); 4110.9 (6, 7); 4121.3 (5, 6); 4140.5 (4, 5); 4199.1 (2, 3); 4236.5 (1, 2); 4278.1 (0, 1); 4459.3 (7, 9); 4466.6 (6, 8); 4490.3 (5, 7); 4515.9 (4, 6); 4554.1 (3, 5); 4599.7 (2, 4); 4651.8 (1, 3); 4709.2 (0, 2); 4864.4 (7, 10); 4881.7 (6, 9); 4913.2 (5, 8); 4957.9 (4, 7); 5012.7 (3, 6); 5076.6 (2, 5); 5148.8 (1, 4); 5228.3 (0, 3); 5485.5 (4, 8); 5564.1 (3, 7); 5653.1 (2, 6); 5754.4 (1, 5); 5864.7 (0, 4)
N_2	Second positive	$C^3\Pi_u - B^3\Pi_g$	2953.2 (4, 2); 2962.0 (3, 1); 2976.8 (2, 0); 3116.7 (3, 2); 3136.0 (2, 1); 3159.3 (1, 0); 3268.1 (4, 4); 3285.3 (3, 3); 3311.9 (2, 2); 3338.9 (1, 1); 3371.3 (0, 0); 3500.5 (2, 3); 3536.7 (1, 2); 3576.9 (0, 1); 3641.7 (4, 6); 3671.9 (3, 5); 3710.5 (2, 4); 3755.4 (1, 3); 3804.9 (0, 2); 3857.9 (4, 7); 3894.6 (3, 6); 3943.0 (2, 5); 3998.4 (1, 4); 4059.4 (0, 3); 4094.8 (4, 8); 4141.8 (3, 7); 4200.5 (2, 6); 4269.7 (1, 5); 4343.6 (0, 4); 4355.0 (4, 9); 4416.7 (3, 8); 4490.2 (2, 7); 4574.3 (1, 6); 4667.3 (0, 5); 4723.5 (3, 9); 4814.7 (2, 8); 4916.8 (1, 7); 5031.5 (0, 6); 5066.0 (3, 10); 5179.3 (2, 9); 5309.3 (1, 8)
N_2	First positive	$B^3\Pi_g - A^3\Sigma_u^+$	6322.9 (10, 7); 6394.7 (9, 6); 6468.6 (8, 5); 6544.9 (7, 4); 6623.6 (6, 3); 6704.8 (5, 2); 6788.6 (4, 1); 6875.2 (3, 0); 7164.8 (7, 5)

Figure 90-39 are representing the results of the effect of pressure on the relative density of the most dominant species in the helium diffuse plasma such as N_2, N_2^+, O, OH, N(I), and N(II). For N_2, N_2^+, and O, the pattern shows that increasing and decreasing the pressure from an optimum pressure has a negative impact on the concentration of those species.

The impact of pressure on the N_2 concentration is lower with respect to its impact on the concentration of N_2^+. As it can be seen in the results, the impact of pressure on the ionized species such as N_2^+, N(I), and N(II) is considerable.

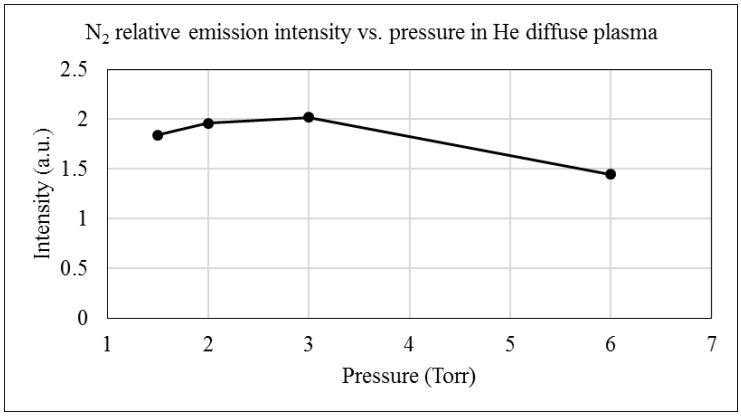

Figure 90. The effect of pressure on the N_2 SPS $0-0$ relative emission intensity at 337 nm in helium diffuse plasma.

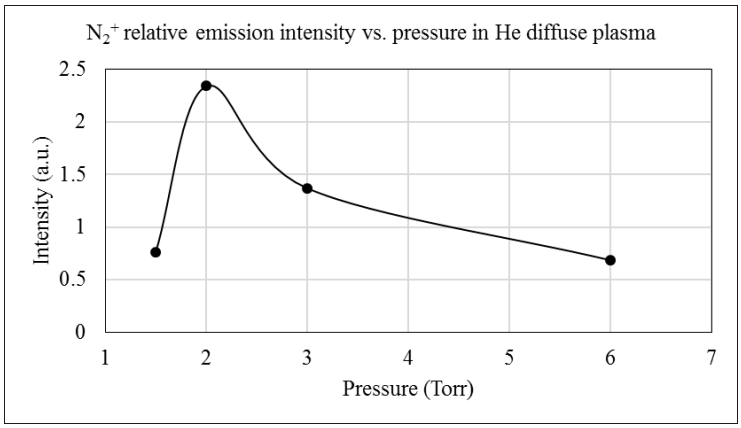

Figure 91. The effect of pressure on the N_2^+ FNS $0-0$ relative emission intensity at 391.2 nm in helium diffuse plasma.

The results in Figure 92 and Figure 93 show that lowering the pressure has a direct effect on the concentration of atomic oxygen and contrariwise, an inverse effect on that of hydroxyl radical. Increasing the pressure has a small impact on both $OH^{\bullet}$ and O in the helium diffuse plasma.

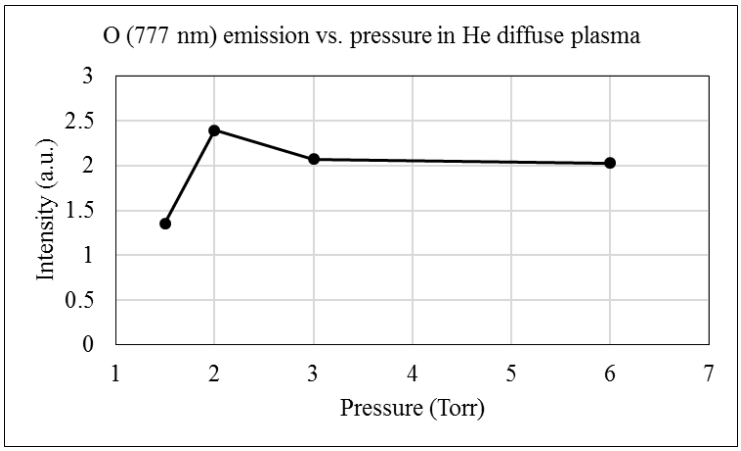

Figure 92. The effect of pressure on the atomic oxygen, O $(3^5S - 3^5P)$, relative emission intensity at 777.25 nm in helium diffuse plasma.

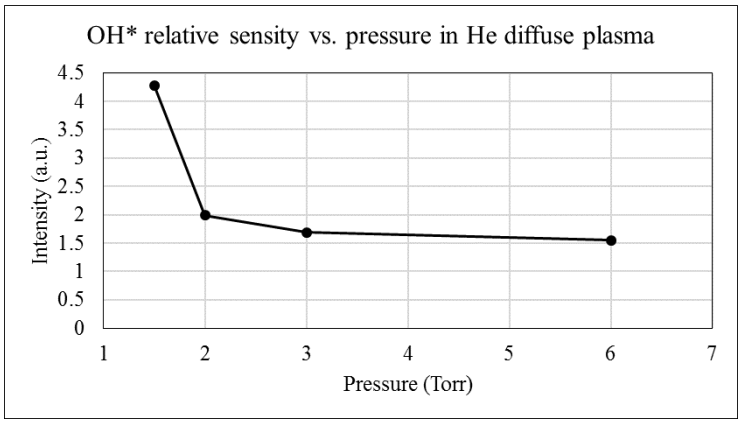

Figure 93. The effect of pressure on the $OH(A - X)$ relative emission intensity at 309 nm in helium diffuse plasma.

Figure 94 and Figure 95 show the effect of pressure on the relative emission intensity of N(I) at 415 nm and N(II) at 595.0 nm, respectively. The reason of exponential drop of N(I) and N(II) concentrations by increasing pressure is that the higher pressure means the higher gas density, which leads to more collisions and less electron mean free path to gain enough energy to ionize

nitrogen. Therefore, the density of the N(II) drops faster than that of N(I) by increasing the pressure, consequently.

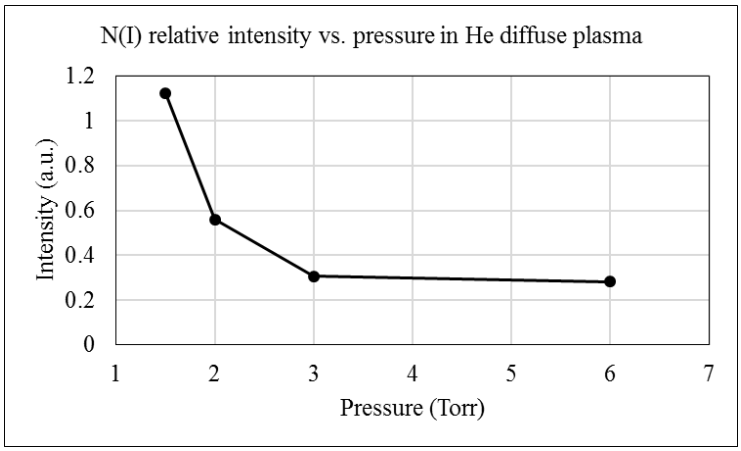

Figure 94. The effect of pressure on the N(I) relative emission intensity at 415 nm in helium diffuse plasma.

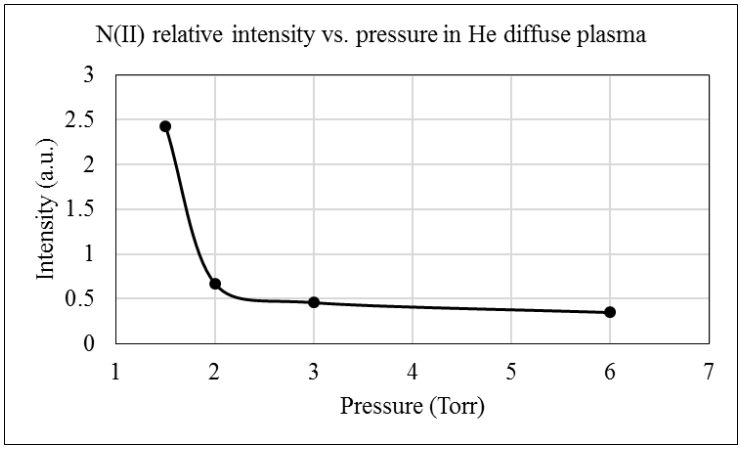

Figure 95. The effect of pressure on the N(II) relative emission intensity at 595.0 nm in helium diffuse plasma.

We also observed the impact of pressure on the generated species in the air diffuse plasma and the results are shown in Figure 96-45. The observed pressure was from 200 mTorr to 2 Torr. The impact of pressure on the N_2 concentration has a similar pattern with the helium diffuse plasma. The concentration of N_2^+ reduces by increasing the pressure.

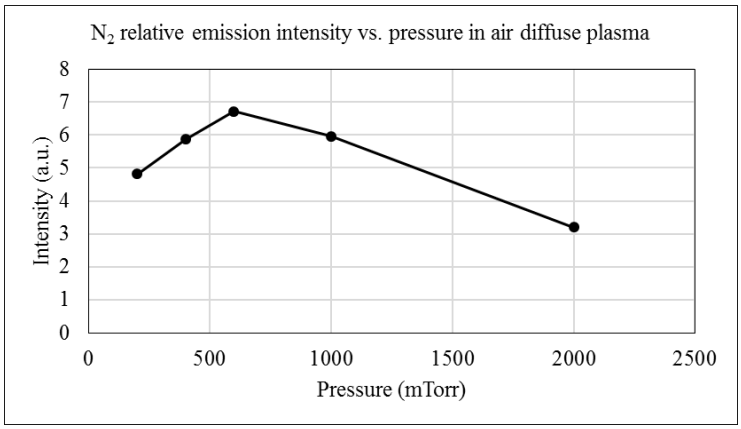

Figure 96. The effect of pressure on the N_2 SPS $0-0$ relative emission intensity at 337 nm in air diffuse plasma.

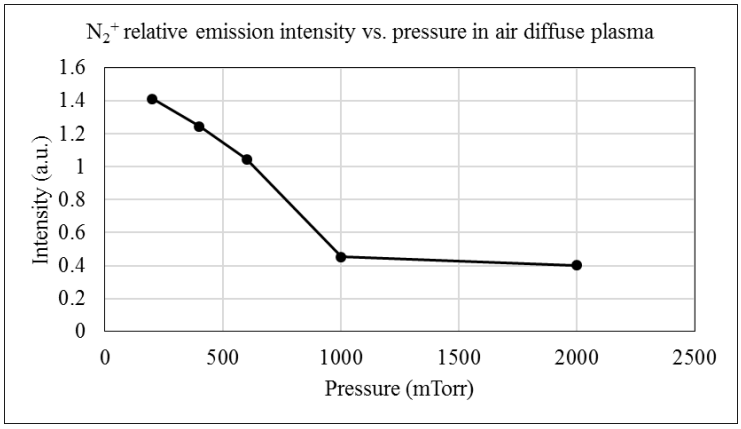

Figure 97. The effect of pressure on the N_2^+ FNS $0-0$ relative emission intensity at 395 nm in air diffuse plasma.

The concentration of atomic oxygen increased by increasing pressure as it is shown in Figure 98. It is interesting that the concentration of atomic oxygen (Figure 98) and hydroxyl radical (Figure 99) in the diffuse plasma filled with air have a totally different response to the applied pressure. It also should be considered that the pressure range in the helium diffuse plasma is in the 1.5-6 Torr while for the air diffuse plasma is in the 200-2000 mTorr.

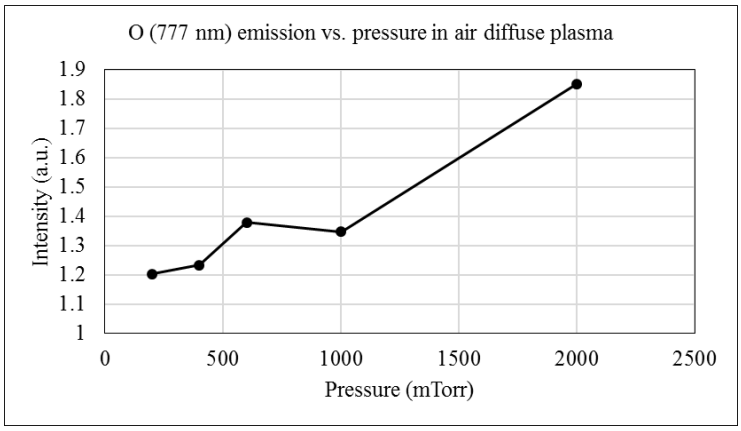

Figure 98. The effect of pressure on the atomic oxygen, O $(3^5S - 3^5P)$, relative emission intensity at 777.25 nm in air diffuse plasma.

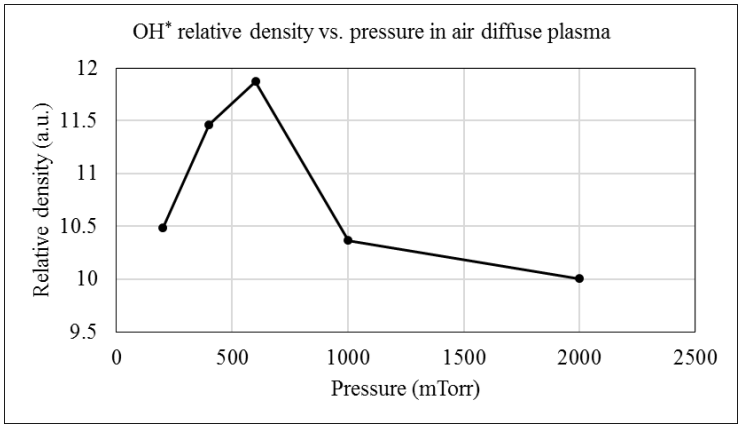

Figure 99. The effect of pressure on the hydroxyl radical, $OH(A - X)$, relative emission intensity at 309 nm in air diffuse plasma.

The relative density of N(I) and N(II) vs. pressure is shown in Figure 100 and Figure 101, respectively. The results show that the concentration of N(I) and N(II) reduces exponentially by increasing pressure from 200 mTorr to 2000 mTorr in the air diffuse plasma. Comparing the results of Figure 100 and Figure 101, it was observed that the concentration of N(I) drops faster than that of N(II) by increasing the air pressure. Our hypothesis is that the quenching effect of air molecules such as O_2, O, and N_2 in the air diffuse plasma is responsible for the higher reaction rates of N(I) as opposed to the N(II) species.

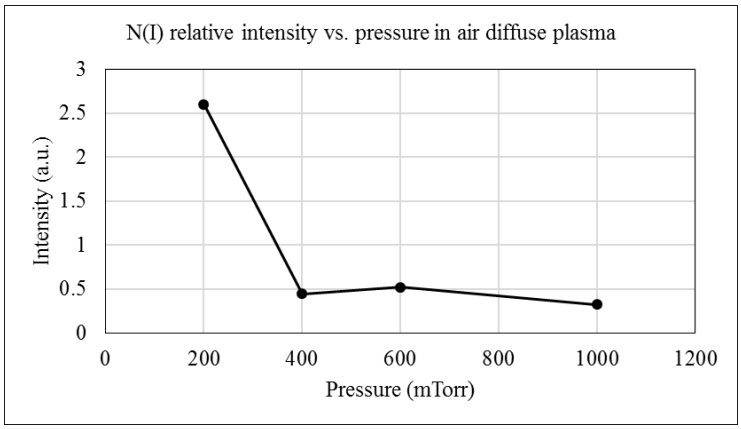

Figure 100. The effect of pressure on the N(I) relative emission intensity at 415 nm in air diffuse plasma.

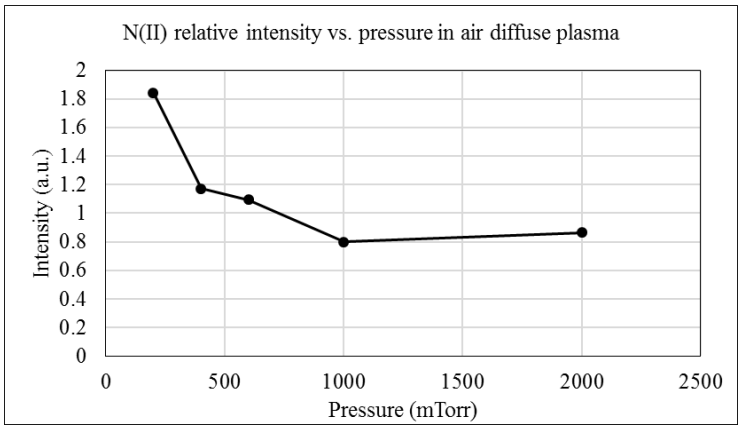

Figure 101. The effect of pressure on the N(II) relative emission intensity at 300.5 nm in air diffuse plasma.

Stark Broadening Technique (Electric field Measurement)

Figure 102 illustrates an example of the π-polarized spectra of He(I) 447.1 nm in the presence of the external electric field from the APPJ plasma. The spectra were measured from the diffuse plasma inside the chamber while the APTLPJ tube exit was 6 mm away from the chamber wall. Allowed peak was measured at 447.22 nm, forbidden peak at 446.96 nm, and E-free peak at

447.18±0.1 nm. $\Delta\lambda_{Allowed-Forbidden}$=0.29 nm indicates the wavelength separation due to the electric field strength inside the chamber and equal to E=18.4 kV/cm.

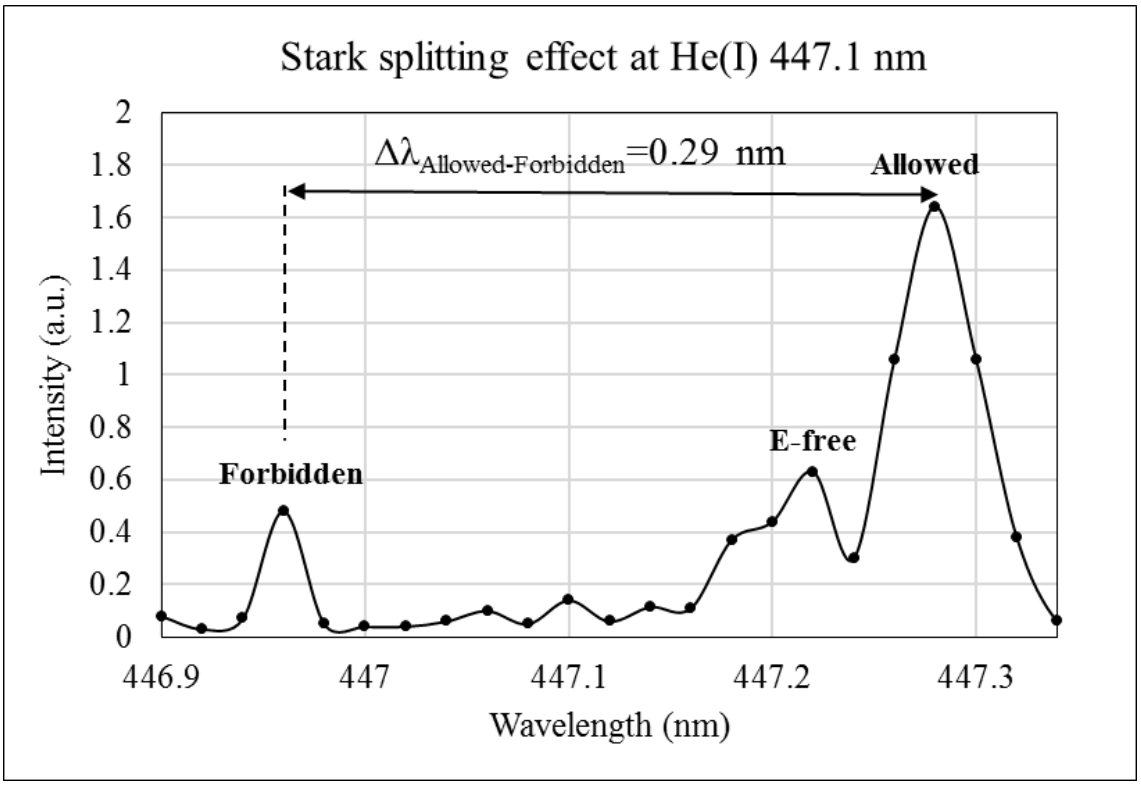

Figure 102. An example of π-polarized spectra of He 447.1 nm. These spectra were measured from the diffuse plasma inside the chamber while the APTLPJ tube exit was 6 mm away from the chamber wall. Allowed peak was measured at 447.22 nm, forbidden peak at 446.96 nm, and E-free peak at 447.18±0.1 nm. $\Delta\lambda_{Allowed-Forbidden}$=0.29 nm indicates the maximum electric field inside the chamber was E=19 kV/cm (Applied voltage: 8.5 kV, repetition rate: 7 kHz, Pulse width: 1 µs, APPJ He flow rate: 7 slm).

The effect of the applied voltage on the electric field strength in the diffuse plasma was investigated. Figure 103 shows the results of the APPJ applied voltage vs. the electric field strength inside the chamber. Increasing the applied voltage generates more intense plasma bullets with a higher electric field and therefore, it enhances the electric field strength inside the low-pressure system. We could not retrieve the information about applied voltages lower than 5 kV due to the inadequate intensity of the forbidden peak.

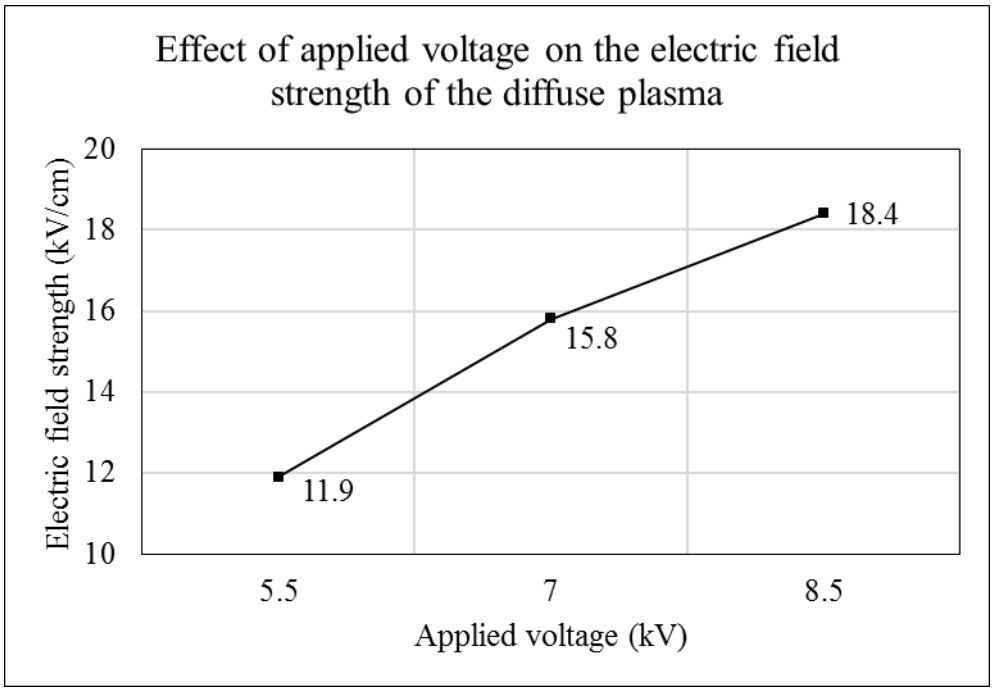

Figure 103. The effect of APPJ applied voltage on the strength of the electric field in kV/cm in the helium diffuse plasma measured by the Stark splitting technique (Applied voltage: 7 kV, pulse width: 1000 ns, repetition rate: 7 kHz, APPJ He flow rate: 7 slm, Pressure: 1.5 Torr, Distance between plasma jet exit tube and the chamber: 6 mm).

We measured the electric field strength by changing the pressure from 1.5 Torr to 3 Torr and it was revealed that the maximum electric field intensity inside the chamber is independent of the pressure in the helium diffuse plasma. The reason is that the highest electric field strength happens in the vicinity of the chamber wall at the point of the plasma bullet incidence and due to the maximum surface charge at that point. The surface charge density on the dielectric surface only depends on the characteristics and configuration of the APPJ plasma as discussed in the previous chapter. However, $\frac{E}{N}$ ratio drops by increasing the pressure (pressure is directly proportional to the gas number density) and that is responsible for the characteristics of the FIW such as the ionization ratio, the propagation speed, and the FIW propagation length.

V.3 SUMMARY

In this chapter, we introduced a space-resolved OES to measure the relative density of the chemical species of the APPJ plasma plume including $N_2\ SPS\ 0-0$ band at 337 nm, $N_2^+\ FNS\ 0-0$ band at 391.2 nm, $OH^*(A-X)$ at 309 nm, $O\ (3^5S-3^5P)$ at 777 nm, and $He\ (2^3P-3^3S)$ at 706 nm as well as their time-resolved measurements by temporal OES method. The relative density of the chemical species vs. applied pressure in a helium and air diffuse plasma was studied too. In the diffuse plasma, in addition to the mentioned emission spectra of the spectral transition bands, the first and double ionization of atomic nitrogen, N(I) and N(II), were detected that reduced by increasing the applied pressure.

The effect of a dielectric obstacle on the APPJ plasma bullet was investigated by fast imaging and image processing techniques. The results showed that the surface discharge on the dielectric material enhances the speed of the surface plasma spread and it has no specific impact on the traveling distance of the discharge outside of the APPJ device. The FIW speed in the low-pressure chamber was measured and the effect of the pressure and the gas type was investigated.

We also applied a method of non-intrusive electric field measurement in a low-pressure transient helium glow discharge by Stark splitting technique using π-polarized spectra of He 447.1 nm line profile. The results showed that the APPJ applied voltage has a direct effect on the electric field strength in the diffuse plasma and on the FIW ionization ratio, and consequently on the FIW propagation speed.

CHAPTER VI

CONCLUSION

The remote generation of a non-thermal diffuse plasma in a nonconductive reduced-pressure chamber was generated by an external guided fast ionization wave (FIW) from an atmospheric-pressure helium low-temperature plasma jet (APPJ). In order to explore the characteristics of the remotely generated diffuse plasma, three conjunct investigations have been reported in the present dissertation as follows:

1. The external plasma source of energy (atmospheric-pressure low-temperature plasma jet) and the propagation mechanisms of the supersonic-velocity plasma bullets.

2. The interaction of the APPJ plasma plume with a dielectric surface which forms the wall of the reduced-pressure system.

3. Electrical and spectroscopic measurements of the diffuse plasma ignition and the propagation phases of the fast ionization waves in the diffuse plasma.

The formation and propagation mechanisms of different types of ionization waves, FIWs, and guided FIWs were introduced (as streamers) and discussed in detail. The capability of atmospheric-pressure guided FIWs generated by an APPJ as a suitable type of carrier of packets of localized energy that is able to be aimed at a specific target remotely and to be transferred through a solid dielectric barrier was adopted for the present research work. This considerable idea is the basis of the present study on the generation of a transient glow discharge plasma remotely, without introducing any electrodes into a reduced-pressure system.

A single-electrode atmospheric-pressure low-temperature plasma jet (APPJ) was chosen to be used as a remote source of energy for the transient glow-discharge plasma to generate guided FIW. In an APPJ, every high-voltage pulse generates two discharges with opposite polarity. The positive and negative polarity discharges happen at the rise time and the fall time of the high-voltage pulse, respectively. The consumed energy of the APPJ during the first and the second discharge was 0.6 mJ and 1.0 mJ when the applied voltage was 7 kV (and He flow rate was 7 slm), respectively. The characteristics of the APPJ when it was placed in front of a planar dielectric obstacle was also investigated. The consumed energy of the APPJ in front of a planar dielectric obstacle during the first and the second discharge was 1.0 mJ and 2.5 mJ when the applied voltage was 7 kV (the distance between the tube exit and the surface was 6 mm and He flow rate was 7 slm), respectively.

The formation and propagation of the plasma bullets were investigated. Fast imaging of the APPJ plasma plume with a time resolution of 20 ns revealed that the speed of the plasma plume is 1.7×10^5 m/s and it is in fact a fast ionization wave traveling along the gas channel in the ambient air. It was also shown that the emitted spectra of the plasma bullet had an exponential drop as it traveled along the plasma jet axis.

The investigations revealed that the fundamental reason for transition of the external guided FIW into another FIW inside the reduced-pressure chamber through a dielectric surface was due to the induced surface charge on the dielectric surface by the enhanced electric field at the frontier of the APPJ fast ionization wave. The induced current and the resultant induced charge was measured by a capacitive passive probe. The induced charge due to the applied voltage to the

APPJ was about 27 nC while the charge due to the approaching plasma plume was 68 nC (for the values of the applied parameters mentioned earlier). We also found that the gas flow rate increases the strength and the traveling distance of the plasma plume on the dielectric surface. Therefore, it has a positive effect on the induced surface charge.

We developed a new D-dot probe to measure the spatiotemporal-resolved net charge in the plasma plume. This probe works based on the induced charge due to the time variation of the electric field in the vicinity of the probe surface. The results of the measurements showed that the plasma plume is positively charged due to the attraction of electrons towards the positive electrode. The plasma plume had two positive net charge peaks at 6 mm (located inside the jet tube) and 18 mm (located outside the jet tube) away from the electrode. The net charge peak inside the plasma jet tube was 22 nC at 320 ns and the net charge peak at 18 mm was 14.5 nC at 425 ns at their maximum peak values when the applied voltage was 7 kV and He flow rate was 7 slm.

Langmuir single probe as an intrusive probing technique was used to determine the plasma features such as electron density, electron temperature, Debye length, and the electric potential of reduced-pressure diffuse plasma. The Langmuir probe was placed in the bulk of the reduced-pressure plasma. The electron temperature in a helium/air plasma at 0.3 Torr was $T_e = 2.73$ eV with the electron density of $n_e = 6.38 \times 10^{16}$ m^{-3}. For the helium diffuse plasma with 30% air admixture, $T_e = 2.2$ eV and $n_e = 1.624 \times 10^{16}$ m^{-3}. Increasing the pressure inside the chamber reduced the electron number density and the ionization ratio, consequently.

In chapter 5, a space-resolved OES was used to measure the relative density of the chemical species of the APPJ plasma plume including $N_2\ SPS\ 0-0$ band at 337 nm, $N_2^+\ FNS\ 0-0$ band at 391.2 nm, $OH^*(A-X)$ at 309 nm, $O\ (3^5S-3^5P)$ at 777 nm, and $He\ (2^3P-3^3S)$ at 706 nm. The time-resolved measurements were also done by temporal OES method. The relative density of the chemical species vs. pressure in a helium and air diffuse plasma was studied too. In the diffuse plasma, in addition to the mentioned emission spectra of the molecular bands, the first and double ionization of atomic nitrogen, N(I) and N(II), were detected and were found to decrease for increasing pressures.

We also used a non-intrusive electric field measurement in a reduced-pressure transient helium glow discharge by Stark splitting technique using π-polarized spectra of He 447.1 nm line profile. The electric field strength of the start point of the helium diffuse plasma at 1.5 Torr was $E = 15.8\frac{kV}{cm}$ when the applied voltage to the APPJ electrode was 7 kV. The results showed that the APPJ applied voltage has a direct effect on the electric field strength in the diffuse plasma and on the FIW ionization ratio.

In conclusion, the generation of large-volume fast ionization wave in an electrically-isolated reduced-pressure system by another FIW from an APPJ was found to be a transient discharge that is generated by electric field enhancement (up to 18.5 kV/cm) in the vicinity of a dielectric surface. The plasma is found to be capable of producing ionic molecules and atoms such as N_2^+, N(I) and N(II). The lack of contamination due to the electrodeless arrangement makes this FIW-generated plasma source an attractive candidate for plasma fabrication and plasma treatment technologies.

Suggested Future Studies

For future studies, the observation and detailed measurements of the electric field inside the chamber as the essential parameter for the generation of reduced-pressure FIW is suggested. The space-resolved and time-resolved measurement of the electric field along the FIW propagation trajectory inside the chamber generated with either negative streamer or positive streamer from APPJ is recommended to gain more information about the mechanisms of the FIW generation and its propagation.

Modelling of this plasma source needs to be done to study the fundamental role of the electric field enhancement, the physiochemical processes, and the configuration of the reduced-pressure system on the FIW plasma generation and its propagation phases. The resultant information from the modeling would make it cost-effective for the optimization of the plasma system.

REFERENCES

[1] P. M. Bellan, *Fundamentals of plasma physics*. Cambridge University Press, 2008.

[2] J. Tyczkowski, *Cold Plasma-A Promising Tool for the Development of Electrochemical Cells*. INTECH Open Access Publisher, 2012.

[3] Y. P. Raizer and J. E. Allen, *Gas discharge physics*. Springer Berlin, 1997.

[4] M. Laroussi, "Low temperature plasma-based sterilization: overview and state-of-the-art," *Plasma processes and polymers,* vol. 2, no. 5, pp. 391-400, 2005.

[5] R. Morent, N. De Geyter, J. Verschuren, K. De Clerck, P. Kiekens, and C. Leys, "Non-thermal plasma treatment of textiles," (in English), *Surface & Coatings Technology,* Review vol. 202, no. 14, pp. 3427-3449, Apr 2008.

[6] A. Fridman, A. Chirokov, and A. Gutsol, "Non-thermal atmospheric pressure discharges," (in English), *Journal of Physics D-Applied Physics,* Review vol. 38, no. 2, pp. R1-R24, Jan 2005.

[7] D. Mariotti and R. M. Sankaran, "Microplasmas for nanomaterials synthesis," (in English), *Journal of Physics D-Applied Physics,* Review vol. 43, no. 32, p. 21, Aug 2010, Art. no. 323001.

[8] C. Jama and R. Delobel, "Cold Plasma Technologies for Surface Modification and Thin Film Deposition," in *Multifunctional Barriers for Flexible Structure: Textile, Leather and Paper*, vol. 97, S. Duquesne, C. Magniez, and G. Camino, Eds. (Springer Series in Materials Science, Berlin: Springer-Verlag Berlin, 2007, pp. 109-124.

[9] D. Xiao, *Gas discharge and gas insulation*. Springer, 2015.

[10] U. Kogelschatz, "Dielectric-barrier discharges: Their history, discharge physics, and industrial applications," (in English), *Plasma Chemistry and Plasma Processing,* vol. 23, no. 1, pp. 1-46, Mar 2003.

[11] H. Aghajani and S. Behrangi, "Pulsed DC Glow Discharge Plasma Nitriding," in *Plasma Nitriding of Steels*: Springer, 2017, pp. 71-125.

[12] M. A. Lieberman and A. J. Lichtenberg, *Principles of plasma discharges and materials processing*. John Wiley & Sons, 2005.

[13] C. Tendero, C. Tixier, P. Tristant, J. Desmaison, and P. Leprince, "Atmospheric pressure plasmas: A review," *Spectrochimica Acta Part B: Atomic Spectroscopy,* vol. 61, no. 1, pp. 2-30, 2006.

[14] J. R. Roth, *Industrial Plasma Engineering: Volume 1-Principles*. CRC press, 1995.

[15] H. Conrads and M. Schmidt, "Plasma generation and plasma sources," *Plasma Sources Science and Technology,* vol. 9, no. 4, p. 441, 2000.

[16] M. Laroussi, X. Lu, V. Kolobov, and R. Arslanbekov, "Power consideration in the pulsed dielectric barrier discharge at atmospheric pressure," *Journal of Applied Physics,* vol. 96, no. 5, pp. 3028-3030, 2004.

[17] M. Laroussi, I. Alexeff, J. P. Richardson, and F. F. Dyer, "The resistive barrier discharge," *IEEE Transactions on Plasma Science,* vol. 30, no. 1, pp. 158-159, 2002.

[18] E. Karakas, M. A. Akman, and M. Laroussi, "The evolution of atmospheric-pressure low-temperature plasma jets: jet current measurements," *Plasma Sources Science and Technology,* vol. 21, no. 3, p. 034016, 2012.

[19] M. Laroussi, X. Lu, and C. M. Malott, "A non-equilibrium diffuse discharge in atmospheric pressure air," *Plasma Sources Science and Technology,* vol. 12, no. 1, p. 53, 2003.

[20] V. Nehra, A. Kumar, and H. Dwivedi, "Atmospheric non-thermal plasma sources," *International Journal of Engineering,* vol. 2, no. 1, pp. 53-68, 2008.

[21] M. Laroussi and H. Razavi, "Indirect Generation of a Large-Volume Diffuse Plasma by an Ionization Wave From a Plasma Jet," *IEEE Transactions on Plasma Science,* vol. 43, no. 7, pp. 2226-2229, 2015.

[22] M. Laroussi and X. Lu, "Room-temperature atmospheric pressure plasma plume for biomedical applications," *Applied Physics Letters,* vol. 87, no. 11, p. 113902, 2005.

[23] N. Mericam-Bourdet, M. Laroussi, A. Begum, and E. Karakas, "Experimental investigations of plasma bullets," *Journal of Physics D: Applied Physics,* vol. 42, no. 5, p. 055207, 2009.

[24] X. Lu and M. Laroussi, "Dynamics of an atmospheric pressure plasma plume generated by submicrosecond voltage pulses," *Journal of Applied Physics,* vol. 100, no. 6, p. 063302, 2006.

[25] A. Begum, M. Laroussi, and M. R. Pervez, "Atmospheric pressure He-air plasma jet: Breakdown process and propagation phenomenon," *AIP Advances,* vol. 3, no. 6, p. 062117, 2013.

[26] J. Jarrige, M. Laroussi, and E. Karakas, "Formation and dynamics of plasma bullets in a non-thermal plasma jet: influence of the high-voltage parameters on the plume characteristics," *Plasma Sources Science and Technology,* vol. 19, no. 6, p. 065005, 2010.

[27] E. Karakas, M. A. Akman, and M. Laroussi, "Propagation phases of plasma bullets," *IEEE Transactions on Plasma Science,* vol. 39, no. 11, pp. 2308-2309, 2011.

[28] M. Laroussi and M. Akman, "Ignition of a large volume plasma with a plasma jet," *AIP Advances,* vol. 1, no. 3, p. 032138, 2011.

[29] X. Lu, G. Naidis, M. Laroussi, and K. Ostrikov, "Guided ionization waves: Theory and experiments," *Physics Reports,* vol. 540, no. 3, pp. 123-166, 2014.

[30] L. M. Vasilyak, S. Kostyuchenko, N. N. Kudryavtsev, and I. Filyugin, "Fast ionisation waves under electrical breakdown conditions," *Physics-Uspekhi,* vol. 37, no. 3, p. 247, 1994.

[31] S. Starikovskaia, A. Y. Starikovskii, and D. Zatsepin, "The development of a spatially uniform fast ionization wave in a large discharge volume," *Journal of Physics D: Applied Physics,* vol. 31, no. 9, p. 1118, 1998.

[32] O. Omarov and A. Rukhadze, "On the theory of plasma streamer development," *Bulletin of the Lebedev Physics Institute,* vol. 36, no. 10, p. 310, 2009.

[33] J. J. Thomson, "Notes on recent researches in electricity and magnetism," *Mercury,* vol. 8, no. 10, p. 115, 1893.

[34] L. B. Loeb, "Ionizing waves of potential gradient," *Science,* vol. 148, no. 3676, pp. 1417-1426, 1965.

[35] A. N. Lagarkov and I. M. Rutkevich, *Ionization waves in electrical breakdown of gases*. Springer Science & Business Media, 2012.

[36] N. Anikin, S. Pancheshnyi, S. Starikovskaia, and A. Y. Starikovskii, "Breakdown development at high overvoltage: electric field, electronic level excitation and electron density," *Journal of Physics D: Applied Physics*, vol. 31, no. 7, p. 826, 1998.

[37] O. V. Boutine and L. M. Vasilyak, "Use of a fast ionization wave for laser pumping," in *Gas and Chemical Lasers and Intense Beam Applications*, 1998, vol. 3268, pp. 334-342: International Society for Optics and Photonics.

[38] H. Raether, "Die Entwicklung der Elektronenlawine in den Funkenkanal," *Zeitschrift für Physik,* journal article vol. 112, no. 7, pp. 464-489, July 01 1939.

[39] L. B. Loeb and J. M. Meek, "The Mechanism of Spark Discharge in Air at Atmospheric Pressure. I," *Journal of Applied Physics*, vol. 11, no. 6, pp. 438-447, 1940.

[40] J. Qin and V. P. Pasko, "On the propagation of streamers in electrical discharges," *Journal of Physics D: Applied Physics*, vol. 47, no. 43, p. 435202, 2014.

[41] M. Zhelezniak, A. K. Mnatsakanian, and S. V. e. Sizykh, "Photoionization of nitrogen and oxygen mixtures by radiation from a gas discharge," *High Temperature Science*, vol. 20, pp. 423-428, 1982.

[42] G. V. Naidis, "Simulation of streamers propagating along helium jets in ambient air: Polarity-induced effects," *Applied Physics Letters,* vol. 98, no. 14, p. 141501, 2011.

[43] N. Liu *et al.*, "Assessment of sprite initiating electric fields and quenching altitude of a1Πg state of N2 using sprite streamer modeling and ISUAL spectrophotometric measurements," *Journal of Geophysical Research: Space Physics*, vol. 114, no. A3, 2009.

[44] J. Vaill, D. Tidman, T. Wilkerson, and D. Koopman, "Propagation of high-voltage streamers along laser-induced ionization trails," *Applied Physics Letters*, vol. 17, no. 1, pp. 20-22, 1970.

[45] M. Teschke, J. Kedzierski, E. Finantu-Dinu, D. Korzec, and J. Engemann, "High-speed photographs of a dielectric barrier atmospheric pressure plasma jet," *IEEE Transactions on Plasma Science*, vol. 33, no. 2, pp. 310-311, 2005.

[46] M. Akman, "Dynamics of non-thermal plasma jets under variable pressure," MS thesis, ECE, Old Dominio University, 2012.

[47] R. J. Magyar, "Electron Collisions with Helium and Argon," Amherst College, 1998.

[48] "DiCam Pro Operating Instructions," ed: pco. imaging, 2004.

[49] J. Wang, C. Gao, and J. Yang, "Design, experiments and simulation of voltage transformers on the basis of a differential input D-dot sensor," *Sensors*, vol. 14, no. 7, pp. 12771-12783, 2014.

[50] Q. Yang, S. Sun, R. Han, W. Sima, and T. Liu, "Intense transient electric field sensor based on the electro-optic effect of LiNbO3," *Aip Advances*, vol. 5, no. 10, p. 107130, 2015.

[51] E. Slikboer, O. Guaitella, and A. Sobota, "Time-resolved electric field measurements during and after the initialization of a kHz plasma jet—from streamers to guided streamers," *Plasma Sources Science and Technology,* vol. 25, no. 3, p. 03LT04, 2016.

[52] H.-E. Wagner, R. Brandenburg, K. Kozlov, A. Sonnenfeld, P. Michel, and J. Behnke, "The barrier discharge: basic properties and applications to surface treatment," *Vacuum*, vol. 71, no. 3, pp. 417-436, 2003.

[53] O. Auciello and D. L. Flamm, *Plasma Diagnostics: Discharge parameters and chemistry*. Academic Press, 2013.

[54] F. F. Chen, "Langmuir probe diagnostics," in *IEEE-ICOPS Meeting, Jeju, Korea*, 2003, pp. 2-6.

[55] M. Campanell, "Negative plasma potential relative to electron-emitting surfaces," *Physical Review E,* vol. 88, no. 3, p. 033103, 2013.

[56] R. Heinisch, F. Bronold, and H. Fehske, "Physisorption of an electron in deep surface potentials off a dielectric surface," *Physical Review B,* vol. 83, no. 19, p. 195407, 2011.

[57] R. Heinisch, F. Bronold, and H. Fehske, "Phonon-mediated sticking of electrons at dielectric surfaces," *Physical Review B,* vol. 82, no. 12, p. 125408, 2010.

[58] R. Heinisch, F. Bronold, and H. Fehske, "Phonon-mediated desorption of image-bound electrons from dielectric surfaces," *Physical Review B,* vol. 81, no. 15, p. 155420, 2010.

[59] N. Gascon, M. Dudeck, and S. Barral, "Wall material effects in stationary plasma thrusters. I. Parametric studies of an SPT-100," *Physics of Plasmas (1994-present),* vol. 10, no. 10, pp. 4123-4136, 2003.

[60] N. Hershkowitz, F. Ze, and H. Kozima, "Negative plasma potentials produced by supplemental electron emission," *Physics of Fluids (1958-1988),* vol. 22, no. 2, pp. 338-346, 1979.

[61] J. Sheehan and N. Hershkowitz, "Negative plasma potential in a multidipole chamber with a dielectric coated plasma boundary," *Journal of Vacuum Science & Technology A,* vol. 30, no. 3, p. 031302, 2012.

[62] E. Brose, "Stärke des elektrischen Feldes und Zerlegung der Wasserstofflinien vor der Kathode des Glimmstroms," *Annalen der Physik,* vol. 363, no. 8, pp. 731-752, 1919.

[63] C. Barbeau and J. Jolly, "Electric field measurement in the cathode sheath of a hydrogen glow discharge," *Applied physics letters,* vol. 58, no. 3, pp. 237-239, 1991.

[64] Z. Donkó, K. Rózsa, R. Tobin, and K. Peard, "Modeling and measurements on an obstructed glow discharge in helium," *Physical Review E,* vol. 49, no. 4, p. 3283, 1994.

[65] B. Ganguly and A. Garscadden, "Electric field and Doppler emission profile measurements in an obstructed hydrogen discharge," *Journal of applied physics,* vol. 70, no. 2, pp. 621-627, 1991.

[66] U. Czarnetzki, D. Luggenhölscher, and H. Döbele, "Space and time resolved electric field measurements in helium and hydrogen RF-discharges," *Plasma Sources Science and Technology,* vol. 8, no. 2, p. 230, 1999.

[67] M. Kuraica and N. Konjević, "Electric field measurement in the cathode fall region of a glow discharge in helium," *Applied physics letters,* vol. 70, no. 12, pp. 1521-1523, 1997.

[68] Y. Lu, S. Wu, W. Cheng, and X. Lu, "Electric field measurements in an atmospheric-pressure microplasma jet using Stark polarization emission spectroscopy of helium atom," *The European Physical Journal Special Topics,* journal article vol. 226, no. 13, pp. 2979-2989, August 01 2017.

[69] G. B. Sretenović, I. B. Krstić, V. V. Kovačević, B. M. Obradović, and M. M. Kuraica, "Spatio-temporally resolved electric field measurements in helium plasma jet," *Journal of Physics D: Applied Physics,* vol. 47, no. 10, p. 102001, 2014.

[70] K. Bell, A. Dalgarno, and A. Kingston, "Penning ionization by metastable helium atoms," *Journal of Physics B: Atomic and Molecular Physics,* vol. 1, no. 1, p. 18, 1968.

[71] M. Hanafi, M. Omar, and Y.-D. Gamal, "Study of laser-induced breakdown spectroscopy of gases," *Radiation Physics and Chemistry,* vol. 57, no. 1, pp. 11-20, 2000.

[72] S. Bayram and M. Freamat, "Vibrational spectra of N2: An advanced undergraduate laboratory in atomic and molecular spectroscopy," *American Journal of Physics,* vol. 80, no. 8, pp. 664-669, 2012.

[73] J. Camacho, J. Poyato, L. Diaz, and M. Santos, "Optical emission studies of nitrogen plasma generated by IR CO2 laser pulses," *Journal of Physics B: Atomic, Molecular and Optical Physics,* vol. 40, no. 24, p. 4573, 2007.

[74] M. Tsumaki and T. Ito, "Optical emission spectroscopy of atmospheric-pressure non-equilibrium plasma with mist injection," *AIP Advances,* vol. 7, no. 12, p. 125211, 2017.

VITAE

Hamid Razavi received his PhD in the Plasma Engineering and Medicine Institute (PEMI) under the advisory of Prof. Mounir Laroussi at Old Dominion University in August 2018. He received his M.S. degree in Plasma Engineering from Laser and Plasma Engineering Institute of Shahid Beheshti University in 2011 and his B.S. degree in Physics from University of Kashan, Iran in 2007. His PhD research was focused on development and diagnostics of a new source of low-temperature plasma ignited by fast ionization wave. His master thesis was on the cracking of organic macromolecules and desulfurization of oil byproducts using dielectric barrier discharge (DBD) plasmas. His current research interests include plasma diagnostics, plasma processing, chemical and industrial applications of plasmas, and modeling of low-temperature plasmas. He has authored and co-authored over 6 research papers published in international peer-reviewed journals and conference proceedings. He was awarded the “Excellent Researcher of the Year” from the University of Kashan in 2006.